Delft University of Technology

Scaling and Modelling Photoluminescence of Si Nanoparticles Embedded in Silicon Oxide

Jim Quik

TU Delft

Background image of cover page obtained from:
http://1fotonin.com/image.php?pic=data/wallpapers/38/WDF_856168.png

Delft University of Technology

Faculty of Electrical Engineering,
Mathematics and Computer Sciences

Master Thesis

Scaling and Modelling Photoluminescence of Si Nanoparticles Embedded in Silicon Oxide

For the degree of Master of Science in Sustainable Energy Technology
at Delft University of Technology.
A project performed at the Photovoltaic Materials and Devices department
of the TU Delft.

To be defended in public at 10:00 on June 15, 2016

Author:
J. Quik

Student Number:
4148711

Master Programme:
Sustainable Energy Technology,
Solar Energy

Supervisors:
dr. R.A.C.M.M. van Swaaij
MSc. M. van Sebille

Graduation Committee:
prof. dr. A.H.M. Smets
dr. T.J. Savenije
dr. R.A.C.M.M. van Swaaij
MSc. M. van Sebille

TU Delft

PVMD
Delft University of Technology

Acknowledgements

Here I will express my gratitude to all people who have contributed both directly and indirectly to this work. First of all I would like to say that I am grateful for all the people I met and worked with during my thesis, and the many people that made this project possible. Some of which I would like to address personally.

First of all I would like to thank my daily supervisor, Martijn van Sebille, who always had time for me. The many interesting discussions and the constructive feedback have greatly contributed to the quality of my work. I really appreciate the freedom he gave me to investigate what interested me, and the challenges it brought me. I am also thankful for the weekly meetings with dr. René van Swaaij, who often pointed out interesting ideas. I would like to thank Jort Allebrandi for his contribution to the nanocrystal inter-particle spacing model, which made it possible for me to determine several properties of the investigated material. I am grateful for the help of Stefaan Heirman, who helped to keep the measurement equipment up and running, which led to little delay during my thesis. Finally I would like to thank ing. Tiny Verhoeven of the Department of Chemical Engineering and Chemistry at the Eindhoven University of Technology, for providing me with XPS data of my samples.

I would also like to take this opportunity to thank the members of the graduation comittee for their time and effort put into judging my work, with special thanks to prof. Arno Smets and dr. Tom Savenije.

Finally I would like to thank some of my friends. First Ronald van Schie, our friendship and mutual interest in solar energy has led to the best collaborations I have experienced during my studies. This has improved my LaTeX skills, which have eased the text processing of this thesis tremendously. And the friends I made in my office, Erika Durán and Timo van Pelt, who made me enjoy the many office hours so much more.

And last but not least, my family, for their loving care and support during all of my studies.

Jim Quik
June 7, 2016

Abstract

Silicon nanoparticles (NPs) embedded in a dielectric matrix, such as SiO_2, pose a promising candidate for all-silicon multi-junction solar cells. This material is often analysed with photoluminescence (PL) measurements. In literature, the intensities of different PL measurements are either directly compared or normalized. Normalization leads to loss of information, and direct comparison is questionable because of the many factors influencing intensity.

In this thesis, a study is performed on PL spectra of Si NPs embedded in intrinsic SiO_x, fabricated with plasma enhanced chemical vapour deposition. A novel way of scaling PL to the amount Si-Si bonds is proposed, using the phonon modes of a-Si and c-Si. Both the PL spectum and the phonon modes are measured simultaneously with a Raman spectroscope. This method makes comparison of intensities between different measurements possible.

First a literature study is performed, which identifies three possible PL mechanisms: quantum confinement in a-Si or c-Si NPs, interface state recombination in the Si/SiO_2 interface, and matrix defects emitting around 2 eV. A theoretical model is derived to relate the emission spectrum to the NP size distribution. A fitting error analysis indicates that a combination of interface state recombination and matrix defects yields the best results with the least amount of fitting parameters.

Finally several experiments are performed, which validate the method and investigate the effect of annealing and passivation temperature, excess silicon content, and Si-rich layer thickness on the PL spectra. The validating experiments indicate that this method is independent of misalignment angles up to at least $7° \pm 2°$, and a lower excitation wavelength results in less signal from the substrate and a larger wavelength measurement range. Passivation with a tube furnace, a rapid thermal process and hydrogen plasma is investigated. Tube furnace passivation results in the lowest defect density, which decreases with increasing passivation temperature up to at least 600 °C. Temperatures in excess of 200 °C are deemed necessary for efficient passivation. By either reducing the excess silicon content, or increasing the Si-rich layer thickness, the clustered NP fraction decreases. At an annealing temperature of 700 °C, a-Si NPs are present, which grow further and form large a-Si patches when the annealing temperature is increased to 900 °C. At a 1000 °C, the a-Si clusters start to crystallize, and a-Si and c-Si NPs coexist. Although PL peak shifts are visible, which are in accordance with quantum confinement, the PL spectra are dominated by interface state recombination.

Table of Contents

Acknowledgements i

Abstract ii

Table of Contents iv

List of Acronyms vii

List of Symbols viii

1 Introduction 1
- 1.1 Motivation . . . 1
- 1.2 Theory . . . 2
  - 1.2.1 Quantum Mechanics . . . 2
  - 1.2.2 Embedded Nanoparticle Formation . . . 5
  - 1.2.3 Phonons . . . 7
  - 1.2.4 Charge Carrier Recombination . . . 8
  - 1.2.5 Photoluminescence of Embedded Nanoparticle Structures . . . 9
- 1.3 Research Goals & Objectives . . . 13

2 Experimental Methods 15
- 2.1 Deposition . . . 15
  - 2.1.1 Substrate Preparation . . . 15
  - 2.1.2 Plasma Enhanced Chemical Vapour Deposition . . . 15
  - 2.1.3 Electron-Beam Physical Vapour Deposition . . . 16
- 2.2 Annealing and Passivation . . . 17
  - 2.2.1 Tube Furnace . . . 17
  - 2.2.2 Rapid Thermal Process . . . 17
  - 2.2.3 Hydrogen Plasma Passivation . . . 17
- 2.3 Characterization . . . 18
  - 2.3.1 Spectroscopic Ellipsometry . . . 18
  - 2.3.2 Fourier Transform Infrared Spectroscopy . . . 19
  - 2.3.3 Raman Spectroscopy . . . 19
  - 2.3.4 Photothermal Deflection Spectroscopy . . . 21
  - 2.3.5 X-ray Photoelectron Spectroscopy . . . 21
  - 2.3.6 Dark Conductivity . . . 21

3 Photoluminescence Scaling & Modelling **23**
3.1 Photoluminescence Scaling . . . 23
3.2 Photoluminescence Modelling . . . 24
3.2.1 Quantum Confinement . . . 24
3.2.2 Interface State Recombination . . . 29
3.2.3 Defects . . . 29
3.3 Fitting Procedure . . . 30

4 Results & Discussion **33**
4.1 Validation . . . 33
4.1.1 Excitation Wavelength . . . 33
4.1.2 Misalignment Angle . . . 36
4.2 Passivation of Dangling Bonds . . . 38
4.2.1 Tube Furnace & Rapid Thermal Process Passivation . . . 38
4.2.2 Hydrogen Plasma Passivation . . . 46
4.3 Excess Silicon Content . . . 50
4.4 Si-rich Layer Thickness . . . 57

5 Conclusions & Recommendations **65**
5.1 Validation . . . 65
5.1.1 Excitation Wavelength . . . 65
5.1.2 Misalignment Angle . . . 65
5.2 Passivation of Dangling Bonds . . . 65
5.2.1 Tube Furnace & Rapid Thermal Process Passivation . . . 65
5.2.2 Hydrogen Plasma Passivation . . . 65
5.3 Excess Silicon Content . . . 66
5.4 Si-rich layer thickness . . . 66
5.5 Photoluminescence Mechanisms . . . 66
5.6 Recommendations . . . 67
5.6.1 Si Nanoparticles Embedded in SiO_2 . . . 67
5.6.2 Scaled Photoluminescence Measurements . . . 67

Bibliography **69**

A Photoluminescence Model **81**
A.1 Layer Thickness Variation . . . 81
A.2 Photoluminescence Maxima . . . 81

B Measurement Error Analysis **83**
B.1 Raman Spectroscope . . . 83
B.1.1 Discussion . . . 85
B.1.2 Incorporation of measurement error . . . 85
B.2 Photothermal Deflection Spectroscope . . . 85

List of Acronyms

a-Si	Amorphous Silicon
c-Si	Crystalline Silicon
FG	Forming Gas
FTIR	Fourier Transform Infrared Spectroscopy
IPA	Isopropylalcohol
ISR	Interface State Recombination
MSE	Mean Square Error
NBOHC	Non-Bridging Oxygen Hole Center
NP	Nanoparticle
P_b center	Dangling bond defect on surface of Si NP
PDS	Photothermal Deflection Spectroscopy
PECVD	Plasma Enhanced Chemical Vapour Deposition
PL	Photoluminescence
QC	Quantum Confinement
RTP	Rapid Thermal Processing
SE	Spectroscopic Ellipsometry
SRH	Shockley-Read-Hall
TF	Tube Furnace
TFA	Tube Furnace Annealed
XPS	X-ray Photoelectron Spectroscopy

List of Symbols

Physical constants

c	Speed of light
h	Planck constant
$\hbar$	Reduced Planck constant
m_0	Electron rest mass
k_b	Boltzmann constant
q	Elementary charge

Theory

a	Width of quantum well or NP diameter
Ψ	Wave function
m^*	Effective mass
m_e^*	Effective mass of electrons
m_h^*	Effective mass of holes
$\vec{r}$	Position of a particle
t	Time
x	Position or $\frac{[\mathrm{O}]}{[\mathrm{Si}]}$ fraction
ϕ	Time component of wave function Ψ
ψ	Position component of wave function Ψ
E	Total energy of particle
E_g	Bandgap of NP
E_bulk	Bandgap of bulk
V	Potential energy
V_0	Potential barrier height
T	Tunneling probability
n	Quantum number
δ	Change in $\frac{[\mathrm{O}]}{[\mathrm{Si}]}$ fraction
ω	Angular frequency
$\vec{k}$	Wave vector
$I_{\mathrm{TO,a\text{-}Si}}$	Integrated intensity of a-Si TO mode
$I_{\mathrm{TO,c\text{-}Si}}$	Integrated intensity of c-Si TO mode
τ	Lifetime
τ_eff	Effective lifetime
R	Recombination rate
Δn	Excess minority carrier concentration
X_c	Crystalline volume fraction
γ	Ratio of Raman efficiencies of a-Si and c-Si

Experimental methods

Δw	Raman shift
λ	Wavelength of backscattered light
λ_{laser}	Wavelength of laser
d	Distance between contacts
E_{act}	Activation energy
I	Current
l	Length of contacts
σ	Conductivity
t	Thickness of layer
T	Temperature
V	Voltage

Photoluminescence Scaling & Model

y	Measured Raman spectrum
$y_{\text{Si-Si}}$	Raman spectrum scaled to Si-Si bonds

Quantum confinement effect

$n_{\text{c-Si}}$	Total c-Si NP density
$n_{\text{a-Si}}$	Total a-Si NP density
$N_{\text{c-Si,NP}}$	Number of atoms in c-Si NP
$N_{\text{a-Si,NP}}$	Number of atoms in a-Si NP
$\rho_{\text{c-Si,layer}}$	Atomic density of c-Si in layer
$\rho_{\text{a-Si,layer}}$	Atomic density of a-Si in layer
$\rho_{\text{c-Si}}$	Atomic density of c-Si
$\rho_{\text{a-Si}}$	Atomic density of a-Si
ρ_{layer}	Total atomic density of layer
ρ_{SiO_2}	Molecular density of SiO_2 in layer
$\Gamma_{\text{c-Si}}$	Atomic percentage of c-Si in layer
$\Gamma_{\text{a-Si}}$	Atomic percentage of a-Si in layer
Γ_{SiO_2}	Molecular percentage of SiO_2 in layer

Functions

f_{mono}	NP size distribution in monolayer
f_{single}	NP size distribution in one layer inside multilayer
f_{multi}	NP size distribution in multilayer
F_{norm}	Normal distribution of energy
G_{layer}	Normal distribution of layer thickness
$P_{\text{i,mono}}$	Isolated NP probability in monolayer
$P_{\text{i,multi}}$	Isolated NP probability in multilayer
F_{norm}	Normal distribution fit function
F_{mono}	Monolayer fit function
F_{multi}	Multilayer fit function
F_{tot}	Total fit fuction
F_{i}	Individial fit function

Parameters

α_{i}	Amplitude fitting parameter
a_{min}	Critical NP diameter
L	Layer thickness
μ_l	Peak position of log-normal and logit-normal
σ_l	Peak width of log-normal and logit-normal
μ_n	Mean of normal distribution
σ_n	Standard deviation of normal distribution

Introduction

1

This chapter starts with the motivation for this research, based on global warming and the need for efficient sustainable energy resources. Next the relevant theory is presented; starting with quantum mechanics, followed by nanoparticle formation, phonons and recombination mechanisms. Finally a short literature review of photoluminescence and its mechanisms in silicon oxide embedded Si nanoparticles is presented, which leads to the research goals and objectives of this master thesis.

1.1 Motivation

The climate problem and all its consequences is one of the global challenges humanity is facing today. In the latest report of the IPCC it is stated that *"continued emission of greenhouse gases will cause further warming and long-lasting changes in all components of the climate system"* and *"limiting climate change would require substantial and sustained reductions in greenhouse gas emissions"* [1, P. 8]. This shows the severity of the problem, and the need for a solution. An approach to reduce greenhouse gas emissions is making a transition to more sustainable and clean energy technologies.

One of these sustainable energy technologies is photovoltaic conversion of sunlight into electricity. This technology has already proven itself with a fast growing market [2]. However silicon-wafer based modules, which have a market share of 92% [2], are approaching their theoretical efficiency limit of 29.4% [3]. The search for higher efficiency has led to the investigation of multi-junction solar cells.

Multi-junction solar cells consist of a stack of two or more cells with different bandgaps, and require advanced bandgap engineering in order to work optimally [4, 5]. Silicon nanoparticles (NPs) embedded in a dielectric matrix such as SiO_2 pose a promising candidate for all-silicon multi-junction solar cells, since it combines a tunable bandgap with abundant materials. The bandgap can be tuned by changing the NP size [6–14], and the use of abundant materials makes it viable for large scale applications [6, 15, 16].

The optical properties of these NPs have been extensively studied with photoluminescence (PL) spectroscopy, providing insight into the electrical properties of the material [17]. However the origin of PL in Si NPs embedded in a SiO_2 matrix is still under debate [7, 17]. The theories include quantum confinement [6–14, 18–27], interface state recombination [11, 20–22, 28–32] and defects [9, 10, 24, 27, 29, 32–39].

The PL intensity indicates the recombination rate and mechanisms at play, and comparing the intensities of different contributions among different samples provides interesting information, such as changes in the electronic structure or defect densities.

In literature there is however no consensus on how to compare different PL spectra; the intensities are either directly compared [8, 11, 40–44], or normalized [29, 31, 45–52]. Normalization leads to loss of information, since only relative intensities of different contributions can be compared, but absolute intensity is lost. Direct comparison is questionable because of the many factors influencing intensity; sample angle [47, 53], contamination, excitation power [54, 55], temperature [52, 56], sample thickness and NP density.

In this thesis a material study is performed on Si NPs embedded in intrinsic SiO_x. The characterization is mainly focused on PL, and a novel way of scaling PL is proposed. Due to this scaling, PL intensities of different measurements can be compared, removing the influence of sample angle, sample thickness and NP density. A model is derived to fit the acquired spectra, and help with identifying the different contributions. Finally four experiments are performed to asses the new scaling method and model, and to elaborate on the source of PL in the material.

1.2 Theory

This section explains the relevant physics and chemistry theory. First quantum confinement (QC) is explained, which is the typical property of NPs. Then NP formation and embedded NP structures are discussed, which supports the structure chosen for this research. Next phonons and recombination mechanisms are addressed. Finally this section is concluded with a literature review on PL mechanims of silicon oxide embedded Si NPs.

1.2.1 Quantum Mechanics

In quantum mechanics the position $\vec{r}$ of a particle at time t is described by its wave function $\Psi(\vec{r},t)$, which is found after solving the Schrödinger equation [57]:

$$i\hbar\frac{\partial}{\partial t}\Psi(\vec{r},t) = \left[V(\vec{r},t) - \frac{\hbar^2}{2m^*}\nabla^2\right]\Psi(\vec{r},t), \tag{1.2.1}$$

where V is the potential, $\hbar$ is the reduced Planck constant, m^* is the effective mass of the particle and ∇ is the Laplacian operator. In contrast to classical mechanics, the wave function does not give the unambiguous position and momentum of a particle. Instead it represents the state of a particle given by Born's statistical interpretation of the wave function [57]:

$$\int_a^b |\Psi(\vec{r},t)|^2\,\mathrm{d}\mathbf{r} = \left\{ \begin{array}{l} \text{Probability of finding the particle} \\ \text{between } a \text{ and } b, \text{ at time } t \end{array} \right\}. \tag{1.2.2}$$

This means that quantum mechanics is governed by statistical interpretations, which is the cause of some interesting quantum effects which are not found in classical mechanics, such as QC.

Quantum Confinement

The QC effect is a typical property of NPs, and can be explained with the quantum well, also known as the infinite square well. This model describes a free particle, which is confined by an infinite potential barrier at the edges of the well. This free particle represents a charge carrier inside a NP, which is confined inside the NP by the high bandgap of surrounding material. The problem is for the sake of simplicity one dimensional, resulting in the following potential:

$$V(x) = \begin{cases} 0 & \text{if } 0 \leq x \leq a \\ \infty & \text{if } x < 0 \text{ or } x > a \end{cases}, \tag{1.2.3}$$

in which a is the width of the well. Since the problem is one dimensional the Schrödinger equation can be reduced. And because V is independent of time, separation of variables can be used; $\Psi(x,t) = \psi(x)\phi(t)$. The time dependent part is neglected for the rest of this example. For the position component $\phi(x)$, the Schrödinger equation becomes

$$V(x)\psi - \frac{\hbar^2}{2m^*}\frac{\partial^2\psi}{\partial x^2} = E\psi. \tag{1.2.4}$$

Here E is a separation constant, introduced by separation of variables. Outside the well the only possible solution is $\psi(x) = 0$. The solution to the Schrödinger equation inside the well is given by:

$$\psi(x) = \sum_{n=1}^{\infty} c_n \psi_n(x), \tag{1.2.5}$$

and where $\psi_n(x)$ is given by:

$$\psi_n(x) = \sqrt{\frac{2}{a}}\sin(\frac{n\pi}{a}x). \tag{1.2.6}$$

$n = 0, 1, 2, 3...$ is the quantum number, representing the state of the particle in the well, and the coefficient c_n is determined by the initial wave function $f(x)$, $c_n = \int \psi_n^*(x) f(x) \mathrm{d}x$ [57]. Since the initial wave function is not considered important for this example, c_n is neglected. The interesting part of this model is that it shows energy discretization and size dependence, because of n and a respectively:

$$E_n = \frac{\hbar^2\pi^2 n^2}{2m^* a^2}. \tag{1.2.7}$$

Now that the solution for 1D is known, it is relatively easy to expand this to 3D. The total energy of the particle is the sum of the energy of each direction:

$$E_{n_x,n_y,n_z} = \frac{\hbar^2\pi^2}{2m^*}\left(\frac{n_x^2}{a_x^2} + \frac{n_y^2}{a_y^2} + \frac{n_z^2}{a_z^2}\right), \tag{1.2.8}$$

where the subscripts x, y and z represent each of the three spatial dimensions. For the simplest case of a cubical box with sides of length a and $n_x = n_y = n_z = n$ equation 1.2.8 reduces to:

$$E_n = \frac{3\hbar^2\pi^2 n^2}{2m^* a^2}. \tag{1.2.9}$$

This equation holds for a cubic NP, however for a spherical NP with a diameter a the confinement is larger because the volume is smaller. Therefore a correction factor of 4/3 is introduced [17]. To obtain the bandgap of a NP, the QC energy of the ground state of the NP is added to the bandgap of the bulk, E_{bulk}:

$$E_{\text{g}} = E_{\text{bulk}} + E_1 = E_{\text{bulk}} + \frac{3\hbar^2\pi^2}{2m^* a^2}. \tag{1.2.10}$$

The effective masses of electrons and holes in silicon are $m_{\text{e}}^* = 1.18m_0$ and $m_{\text{h}}^* = 0.81m_0$ respectively [58], with m_0 the electron rest mass. The total effective mass is then calculated using the following relation [57]:

$$m^* = \left(\frac{1}{m_{\text{e}}^*} + \frac{1}{m_{\text{h}}^*}\right)^{-1}, \tag{1.2.11}$$

which leads to an effective mass of $m^* = 0.48m_0$.

Tunnelling

In classical mechanics it is impossible to overcome a potential barrier with height V_0 when $E < V_0$, with E the energy of the particle. In quantum mechanics however there is a possibility to pass this barrier because of the probabilistic nature of the wave function. For example we consider a potential barrier of height V_0, ranging from $x = 0$ to $x = a$. When a particle approaches the barrier, there is a finite probability for the particle to exist beyond the barrier. The reason for this is the probabilistic nature of the wavefunction and the requirement of continuity. There will be an exponential decay inside the barrier, and since the wave function must be continuous, at the other side of the barrier the wave function cannot be zero, see figure 1.1a. For the potential barrier problem, an approximation of the tunneling probability is given by [59, 60]:

$$T \approx \exp -\sqrt{\frac{8a^2m^*(V_0 - E)}{\hbar^2}}. \tag{1.2.12}$$

This shows that the barrier should be thin and low, or the particle should have a high energy, to reach a high tunneling probability. Further expanding the problem, a finite potential well is defined:

$$V = \begin{cases} V_0 & \text{if } x \leq -a \\ 0 & \text{if } -a < x < a \\ V_0 & \text{if } x \geq a \end{cases}. \tag{1.2.13}$$

A finite potential well represents a nanoparticle embedded in a host material, where the bandgap of the host material defines the potential of the well. The solution to this problem is a cosine in the well, with an exponential decay in the edges of the well[61]. The shape of this wave function is shown in figure 1.1b.

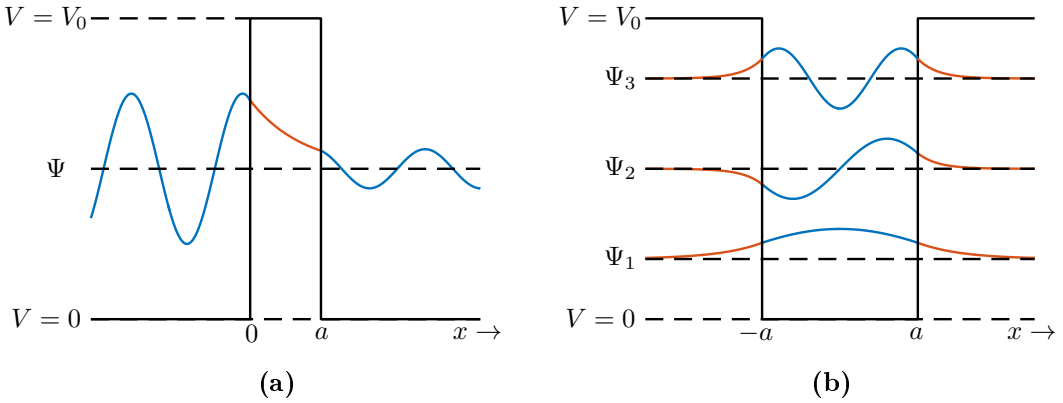

Figure 1.1: The effect of quantum tunneling in **(a)** a potential barrier and **(b)** a finite well. The red line is an exponential decay of the wavefunction inside the potential barrier. The vertical offset in **(b)** is for clarity. The initial wavefunction is arbitrary and not considered important for this example.

One can imagine that if the edges of the well are of a finite thickness, there is again a chance that the particle tunnels through the barrier as in figure 1.1a. When the problem is expanded to a repetition of finite wells with a finite barrier thickness, we approach a NP superlattice. In this hypothetical model, charge transport can only occur by tunneling of charge carriers. In a real material there could also be energy levels inside the potential barrier, or clustering of NPs which both allow for other charge transport mechanisms.

1.2.2 Embedded Nanoparticle Formation

The conventional method of fabricating Si NPs embedded in a SiO_2 layer is by depositing a layer of silicon suboxide, a-SiO_x with $x < 2$ [4]. High temperature annealing of a-SiO_x causes phase separation described by:

$$\text{a-SiO}_x \rightarrow \frac{x}{x+\delta}\ \text{a-SiO}_{(x+\delta)} + \left(1 - \frac{x}{x+\delta}\right)\ \text{a-Si}, \tag{1.2.14}$$

with $x + \delta \leq 2$ [44]. δ is the change in $\frac{[O]}{[Si]}$. It is reported that this process starts around 600 °C [62] to 650 °C [8]. Full stoichiometrization occurs according to the following equation:

$$\text{a-SiO}_x \rightarrow \frac{x}{2}\ \text{a-SiO}_2 + \left(1 - \frac{x}{2}\right)\ \text{a-Si}, \tag{1.2.15}$$

which is the limiting case of equation 1.2.14 where $x + \delta = 2$ [44, 46, 63]. It is believed that this phase separation ensures separation of Si NPs by a SiO_2 shell [46].

The a-Si NPs start to crystallize if the cluster radius is larger than the critical crystallization radius, and when the temperature is above the crystallization temperature [46]. The critical crystallization radius for a-Si is calculated to be around 0.57 nm [64, 65]. The a-Si clusters start to crystallize between 900 °C [62] to 1000 °C [8]. The crystallization temperature depends on composition [8], because an a-SiO_x/a-Si interface decreases the crystallization temperature of a-Si compared to an a-SiO_2/a-Si interface [64].

Embedded Nanoparticle Structures

By changing the initial composition of the silicon suboxide or the annealing conditions, the size of the NPs can be controlled [4, 7, 12]. The resulting monolayer is shown in figure 1.2a. Another method to create Si NPs embedded in SiO_2 is a multilayer structure; a repetition of SiO_x and SiO_2 layers [4], so called Si-rich and buffer layers. In this structure the NP size can be controlled to a certain degree by the Si-rich layer thickness and composition [46, 47], and the vertical NP separation is controlled by the thickness of the buffer layer [4, 46], see figure 1.2b. In a solar cell the contacts will be positioned on the bottom and top of the cell, hence this is the direction where charge transport is most important. It is believed that this method gives better control over the NP size and separation than the monolayer structure [47, 66, 67], and this method has often been applied for embedded NP formation [66, 68–76]. Therefore a multilayer structure is used in this thesis.

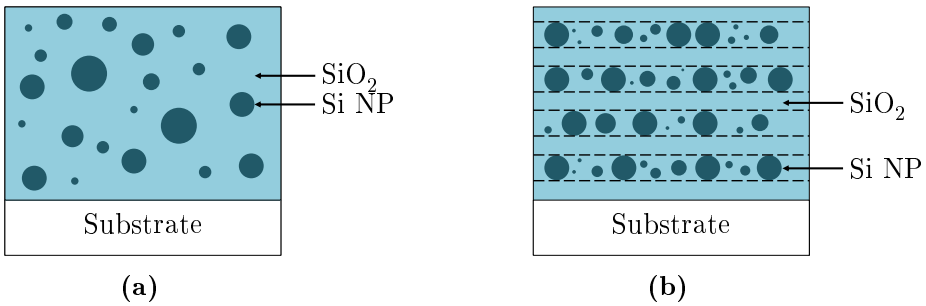

Figure 1.2: **(a)** The monolayer and **(b)** multilayer structure of Si NPs embedded in SiO_2, both after annealing. Made after Janz *et al.* [67].

1.2.3 Phonons

Although in a solid atoms are bonded together, they are always in a state of continuous motion at temperatures above absolute zero. This is vibrational motion around an equilibrium position in the lattice of the material. The modes of vibration are called phonons, of which there are four types; longitudinal acoustic (LA), transverse acoustic (TA), longitudinal optic (LO) and transverse optic (TO) [61]. Longitudinal and transverse refer to the direction of energy transfer with respect to the atomic displacement; longitudinal means they are aligned, while transverse means they are perpendicular. Acoustic and optic refer to the phase of the atomic displacement; acoustic means that all atoms are in phase, while optic means that neighbouring atoms are in opposite phase. These atomic vibrations can be compared to an interconnected series of masses and springs. The four phonon modes are illustrated in figure 1.3.

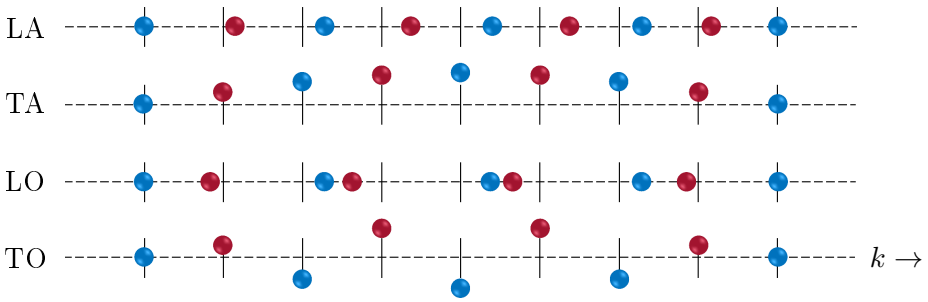

Figure 1.3: Schematic illustration of the four different phonon modes, made after Harrison [61].

Crystallinity

Many solids can exist in both amorphous and crystalline form. Differences in optical and electrical properties between amorphous and crystalline Si NPs have been observed [77, 78], and therefore it is important to quantify the crystalline volume fraction, which is often obtained by measuring a Raman spectrum. Using the integrated intensities of the amorphous and crystalline TO modes, $I_{\text{TO,a-Si}}$ and $I_{\text{TO,c-Si}}$ respectively, the crystalline volume fraction X_{c} can be calculated according to [79, 80]:

$$X_{\text{c}} = \frac{I_{\text{TO,c-Si}}}{\gamma I_{\text{TO,a-Si}} + I_{\text{TO,c-Si}}}. \tag{1.2.16}$$

Here γ is the ratio of Raman efficiencies of the a-Si TO mode compared to the c-Si TO mode. This ratio is due to the difference in cross-section of the two phonon excitations, and is set at 0.8 [80–82].

1.2.4 Charge Carrier Recombination

Generation of excess charge carriers in a semiconductor can be achieved by illuminating the material, with a photon energy larger than the bandgap. A valence electron can then be excited into the conduction band, leaving behind a hole in the valence band. This process is called photogeneration, and is one of the key principles of a solar cell. If excited charge carriers are not collected, they will recombine again through one of the three types of recombination; radiative, Shockley-Read-Hall (SRH) or Auger. These three mechanisms are illustrated in figure 1.4.

With radiative recombination the electron relaxes to the valence band, emitting a photon with an energy equal to the bandgap. For efficient radiative recombination the material should be a direct bandgap material, since then no additional phonons are required[16].

SRH recombination is indirect recombination, facilitated by an impurity atom or lattice defect. These defects introduce energy levels within the quasi-fermi levels, E_{T}, which assists charge carrier recombination. For SRH recombination a conduction electron can then recombine with a hole by stepping through the defect energy level. This type of recombination is typically non-radiative, and excess energy is usually dissipated in the form of heat [16].

Auger recombination is a three-particle process. The excess energy of recombination of an electron and hole, is transferred to a third particle. This third particle is either an electron in the conduction band, or a hole in the valence band. The third particle is then further excited into the respective band, after which it thermalizes to the band edge.

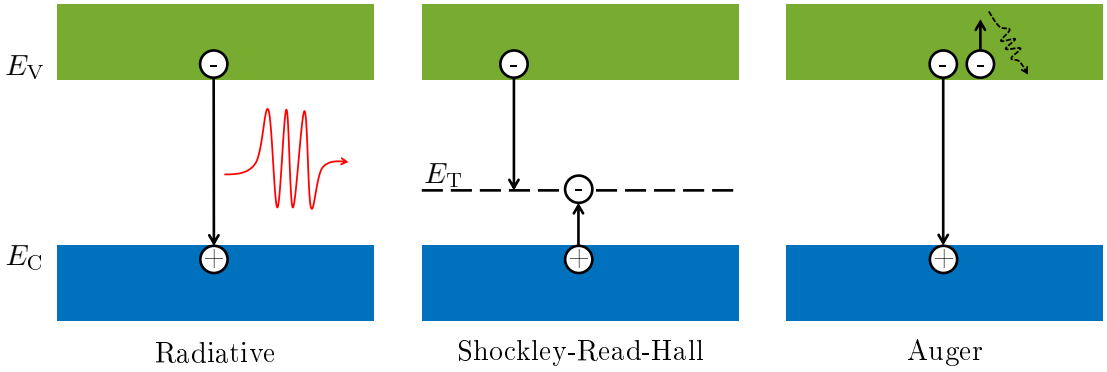

Figure 1.4: The three types of recombination in a semiconductor. Only one of the two configurations is shown for SRH and Auger recombination. The red wave represents a photon. The white circles represent holes and electrons, indicated by the + and − respectively. E_{V} and E_{C} represent the valence and conduction band edges, and E_{T} is the trap state energy.

The average time a charge carrier is excited before recombination is called the lifetime, τ. The effective lifetime, τ_{eff}, is related to the lifetime of each recombination

mechanism by:

$$\frac{1}{\tau_{\text{eff}}} = \sum_i \frac{1}{\tau_i}, \tag{1.2.17}$$

where the subscript i represents the recombination mechanism. The recombination rate R is related to the lifetime by:

$$R = \frac{\Delta n}{\tau}, \tag{1.2.18}$$

where Δn is the excess minority carrier concentration. Since the effective lifetime is strongly reduced by the recombination mechanism with the shortest lifetime, the recombination rate is therefore dominated by that process.

1.2.5 Photoluminescence of Embedded Nanoparticle Structures

PL is based on radiative recombination after photogeneration of charge carriers [17]. For semiconductors this process consists of the absorption of a high energy photon, which excites charge carriers from deep in the valcence band far into the conduction band. These charge carriers then thermalize to the band edges, and recombine through one of the recombination mechanisms discussed in the previous section. Although PL only considers radiative recombination, as shown in figure 1.5, the PL spectrum contains much information about the electronic structure of the material [17].

The origin of PL in Si NPs embedded in a SiO_2 matrix is still under debate [7, 17], therefore a short summary of the current theories is presented. First QC in NPs is discussed, then interface state recombination (ISR) is treated, and finally defects in the material are considered.

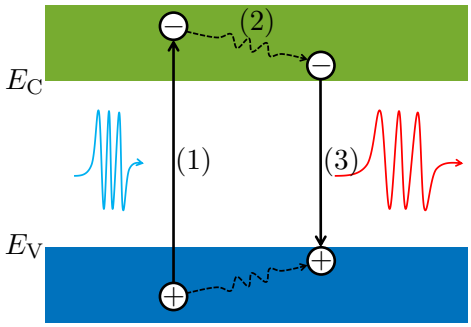

Figure 1.5: Schematic representation of PL in a semiconductor. The blue and red wave represent a photon with high and low energy respectively. The white circles represent holes and electrons, indicated by the + and − respectively. E_V and E_C represent the valence and conduction band edges. (1): absorption and excitation. (2): thermalization to the band edges. (3): radiative recombination.

Quantum Confinement in Si Nanoparticles

As discussed in section 1.2.1 the theoretical bandgap of a NP depends on the particle diameter. Because the PL spectrum depends on the bandgap of the material, the PL spectrum should also depend on the particle diameter. Since this size dependence is often seen in the experimental results, QC in NPs is often the explanation for the resulting PL [17]. In figure 1.6a typical spectra of Si NPs embedded in SiO_2 are shown, and figure 1.6b shows the general observed trend in PL maxima as a function of NP size. QC is both observed in amorphous [14, 18, 25–27] as well as crystalline NPs [6–13, 18–25, 28].

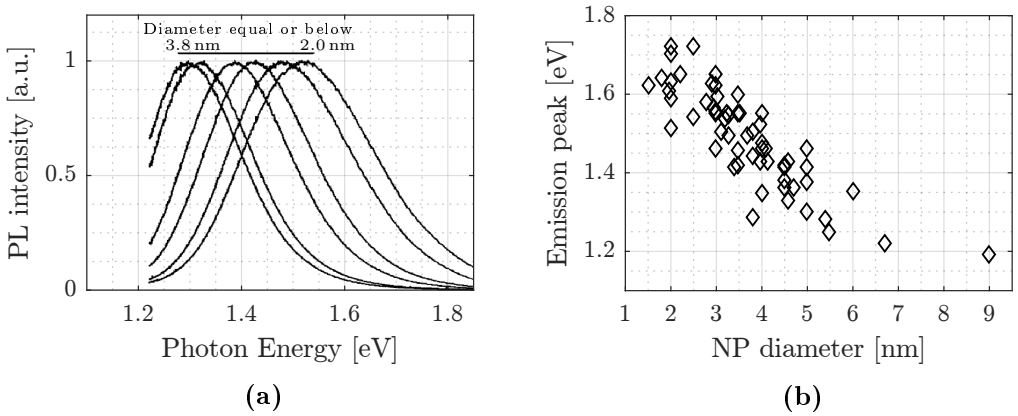

Figure 1.6: PL spectra and maxima of Si NPs embedded in SiO_2. **(a)**: Normalized PL spectra of multilayer samples with different NP diameter, taken from Zacharias *et al.* [46]. **(b)**: PL maxima as a function of NP size, taken from Küsová *et al.* [83].

Interface States

It has been shown that the Si/SiO_2 interface is not sharp; the NPs are surrounded by an intermediate region of *a*-Si and strained SiO_2 [84]. Next there is a region of compressed SiO_2 because of the higher density of Si atoms in Si than in SiO_2, which extends about 3 nm into the SiO_2 [85]. Therefore some theories state that PL originates from ISR at the Si/SiO_2 interface [11, 29, 32]. The position of these photoluminescent peaks show only little dependence on NP size, thus not following QC [11, 20–22, 28–32, 48].

Defect States

Defect states are the last mechanism considered. These defects include photoluminescent defects in the SiO_2 matrix, and photoluminescent quenching dangling bonds at the NP surface. Photoluminescent defects often have characteristic peak positions

independent of Si concentration [9]. A well characterized defect is the non-bridging oxygen hole center (NBOHC), with an emission at 1.91 eV [24, 34, 36, 86]. It is the oxygen part of a broken Si-O bond in the SiO_2 matrix, and can form by rupturing a strained Si-O bond [36, 87, 88], see figure 1.7. Other reported defects include a double bonded Si=O at the Si/SiO_2 interface (1.66 eV) [34] or oxygen deficiencies (2.0 eV) [30].

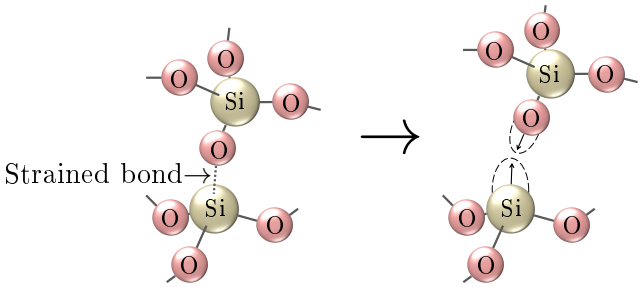

Figure 1.7: The formation of a NBOHC defect. The arrows denote the unpaired spin and the dashed balloons represent their orbitals. Made after Salh[87].

An important PL quenching defect is a dangling bond defect at the surface of a NP [89], also called a P_b center. P_b centers are considered important non-radiative recombination sites [43, 90, 91], therefore reducing PL intensity. They have been identified as a silicon atom bonded to only three silicon atoms, with the non-bonding orbital aligned along the (111) directions [92]. Other dangling bond configurations are intermediate oxidation states of Si; Si^{1+} (Si_2O), Si^{2+} (SiO), and Si^{3+} (Si_2O_3) [85]. Throughout this report dangling bonds on the surface of a Si NP will be referred to as P_b centers.

To reduce the effect of defects, samples are passivated with hydrogen. Beneficial effects of the interactions of hydrogen in silicon have been shown already in 1976 [93]. It is strongly believed that atomic hydrogen passivates dangling bonds [4, 5, 13, 53, 70, 90, 94–97]. Hydrogen can also passivate photoluminescent defects, such as defects in SiO_2 [10]. Passivation of defects increases the lifetime of the specific recombination mechanism, reducing the recombination rate. This will result in relatively more recombination in other mechanisms, ultimately increasing PL of other mechanisms, such as previously mentioned QC or ISR [13, 53, 70].

To give a clear overview of this summary the reported PL maxima and their ascribed contributions are illustrated in figure 1.8.

Comparing Photoluminescence Spectra

The presented summary focused mainly on peak position rather than intensity. Intensities of different contributions indicate the recombination rates of the different mechanisms, and is therefore valuable information. The intensity of different contri-

butions within one measurement can be compared straightforwardly, however comparing the intensity of different measurements and samples is questionable. In literature there is no consensus on how to compare different PL spectra; the intensities are either directly compared [8, 11, 40–44], or normalized [29, 31, 45–52].

There are some reasons which make direct comparison doubtful. For instance the sample could be at a different angle, which could result in a different intensity due to increased reflection of the excitation beam. In some research the normalized PL spectra are complemented with PL quantum yield measurements using an integrating sphere [47, 53]. This technique measures the spectral emission of a sample, integrating over all directions, thereby removing the angle-dependence. Another technique, although not used in characterization of Si NPs, called angle-resolved PL, shows angle-dependent PL intensity and even spectra for some materials [98–100]. Both techniques are far more complicated than a regular PL measurement and require specialized equipment. Other effects influencing PL intensity include contamination of the surface of the sample, excitation power [54, 55], temperature [52, 56], sample thickness and NP density.

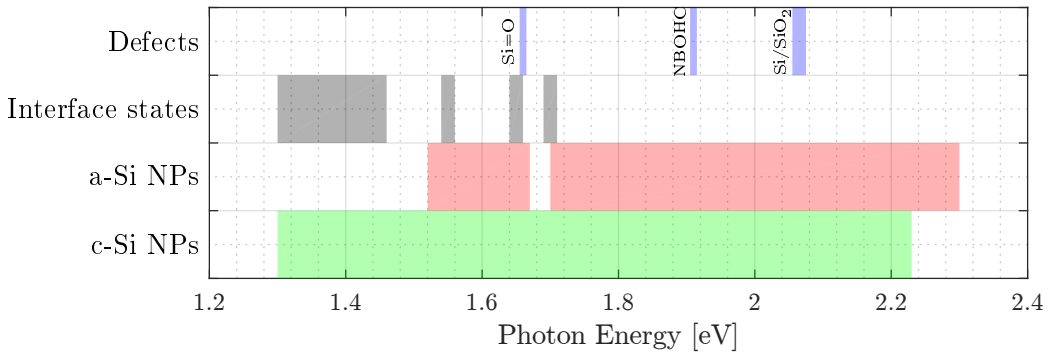

Figure 1.8: Reported PL maxima and their ascribed contributions in the PL spectrum of the considered structure. See table A.1 for data and references.

1.3 Research Goals & Objectives

As discussed in section 1.2.5, PL gives insight into the electronic structure, the recombination mechanisms, the defect density and the charge carrier lifetimes. Comparison of intensities of different PL measurements is however doubtful, and would require specialized equipment, such as integrating spheres. Therefore the research goal of this thesis is:

Develop a method for comparison of photoluminescence spectra and intensities of different measurements of embedded silicon nanoparticle structures using a Raman spectroscope, and identify the different recombination mechanisms in their spectra.

To achieve this goal the following objectives are set:

- **Develop a scaling method for comparing PL spectra and intensities**
  The PL spectrum is measured with a Raman spectroscope, and simultaneously the a-Si and c-Si phonon modes are measured. Using the phonon modes to scale the PL spectrum, several factors influencing PL could be bypassed.
- **Develop a model to fit the PL spectra**
  A fitting model is derived to give insight in the PL mechanisms present in the PL spectra. The model is divided into three parts; QC, ISR and defects. An overfitting analysis must be performed to identify the best combination of fitting functions.
- **Assess the scaling method**
  Using different excitation wavelengths during a Raman measurement to distinguish between Raman phonon modes and PL. And misaligning a sample in order to examine the effect of misalignment on the scaled PL. These two experiments will identify PL in the measured data, and validate the scaling method.
- **Assess the effect of passivation on the PL**
  Applying the presented method and model to assess the effect of different passivation conditions. Three passivation methods are considered: tube furnace passivation, rapid thermal process passivation and hydrogen plasma passivation. Each of these three techniques is performed at three different temperatures, providing insight into the passivation reaction, and the behaviour of different PL mechanisms.
- **Assess the effect of composition of the Si-rich layer on the PL**
  By changing the composition of the Si-rich layer, the NP size distribution and clustered NP fraction is changed. This will influence the PL spectrum, providing insight into the different contributions.

- **Assess the effect of Si-rich layer thickness on the PL**
  By varying the Si-rich layer thickness the maximum size of the NPs is changed. Each thickness is annealed at three different temperatures, and passivated with the tube furnace. This gives insight into the source of PL, and structural changes in the samples.

Experimental Methods

2

This chapter explains the experimental methods used throughout this thesis. First the deposition is treated, explaining both the substrate preparation as well as the deposition techniques. Then annealing and passivation is discussed, which deals with the tube furnace. Finally characterization of the samples is explained, comprising of optical techniques to obtain structural and electronic information, and an electrical technique to obtain the conductivity of the samples.

2.1 Deposition

First the substrate preparation is discussed, after which two deposition techniques are described. First plasma enhanced chemical vapour deposition, which is the deposition used for the creation of the multilayer structure. Then physical vapour deposition is addressed, as it is used for the deposition of aluminium contacts. All depositions are performed in a class 10 000 cleanroom, while wearing cleanroom clothes and gloves.

2.1.1 Substrate Preparation

In this thesis both quartz and c-Si wafer substrates are used. Spectrosil® 2000 is used as a quartz substrate, which is ultra-high purity silica with exceptional optical transmission from 0.62 eV to 6.9 eV [101]. The c-Si wafer substrates are 300 μm thick, [100] oriented p-type wafers with a resistivity of 1000-10 000 Ωcm. Each substrate is cleaned in an ultrasonic bath for 10 min in acetone, followed by 10 min in isopropylalcohol, more commonly known as IPA. After each bath the substrates are dried using a nitrogen flow. This entire procedure is executed under a fume hood, and during this process the substrates are handled with tweezers. The native oxide layer on the c-Si wafer is not removed because it does not hinder the deposition, or any of the used characterization techniques.

2.1.2 Plasma Enhanced Chemical Vapour Deposition

Plasma Enhanced Chemical Vapour Deposition (PECVD) is a technique for the deposition of thin films. PECVD is a well-developed technique, which is often used for creating multilayer structures for embedded NP formation [6, 21, 67, 70, 71, 73, 102]. Using a plasma to deposit thin films makes low substrate temperatures possible, below 200 °C, which is lower than for conventional chemical vapour deposition processes [16].

PECVD is based on the following principle: first precursor gases are injected into the deposition chamber. Then electrical energy is used to generate a plasma, which generates reactive radicals. These interact with the substrate, allowing thin film growth. Because the formation of reactive species occurs in the gas phase, the substrate can be maintained at low temperatures. The pressure, substrate temperature, precursor gas composition, duration and the power coupled into the plasma are some of the parameters determining the composition and thickness of the film [16].

In this thesis a radio frequency PECVD is used, with a radio frequency signal of 13.56 MHz. All samples are deposited using PECVD at a pressure of 1.4 mbar, substrate temperature of 90 °C, plasma power density of 21 mWcm^{-2} and electrode distance of 14 mm. The multilayer structure of the samples consists of alternating Si-rich and buffer layers. It contains a total of 37 Si-rich layers and 38 buffer layers, starting and ending with a buffer layer. The thicknesses of the Si-rich and buffer layers are 3 nm and 1 nm respectively, unless specified otherwise. Throughout this theses three compositions are used, two Si-rich compositions with different excess Si content, and one buffer composition. The composition is determined using X-ray photoelectron spectroscopy. The gas flows for the different compositions are shown in table 2.1.

Table 2.1: PECVD settings for the deposition of the different compositions. The settings of $SiO_{0.3}$ and $SiO_{1.3}$ were adopted from Fusi, 2015 [103], and used as a starting point to obtain the $SiO_{0.9}$ composition.

		Gas flows [sccm]		
Layer	Composition	SiH_4	CO_2	H_2
Si-rich	$SiO_{0.3}$	10	27	200
Si-rich	$SiO_{0.9}$	4	55	200
Buffer	$SiO_{1.3}$	2	72	200

2.1.3 Electron-Beam Physical Vapour Deposition

The aluminium contacts used for determining the conductivity of the sample are deposited using physical vapour deposition. This technique vaporizes the source material in a vacuum chamber by bombarding an Al target with an electron-beam. The vaporized particles travel through the vacuum and reach the sample, condensing and forming a layer on the sample [16]. The size and shape of the contacts is controlled by shadow masks, masking off the area that should remain free from the depositing film.

For this process the Provac PRO500S is used. All contacts made for the experiments discussed in this report are 300 nm thick aluminium. The contacts are 2×4 mm, and spaced 0.5 mm apart. After the deposition the contacts are annealed at 130 °C for 30 min in air at atmospheric pressure.

2.2 Annealing and Passivation

As explained in the theory section, annealing and passivation are important processes for high quality embedded NPs; annealing causes phase separation and NP formation, and passivation reduces defect densities. Tube furnace processing is used for annealing and passivation throughout this thesis. Rapid thermal processing and hydrogen plasma passivation are two techniques used for passivation in one of the experiments.

2.2.1 Tube Furnace

A tube furnace (TF) is a furnace which can reach temperatures around 1000 °C, and can be used for process times in the order of hours. Gasses can be injected into these furnaces to provoke certain reactions.

All TF processes are perfomed in a Tempress horizontal tube stack. In this thesis a nitrogen flow is used for annealing, and a forming gas (FG) (90% N_2 and 10% H_2) flow is used for passivation. The maximum temperature ramp of the used TF is 10 °C/ min, and is used for every TF process. The loading and unloading temperature is 100 °C, in order to minimize oxidation of the sample. The samples are placed with the substrate onto a c-Si wafer, which acts as a carrier. The annealing and passivation settings used throughout this thesis are presented in the table below.

Table 2.2: Annealing and passivation settings for the TF unless specified otherwise.

	Maximum temperature	Time	Gas	Gas flow [slm]
Annealing	1000 °C	1 h	N_2	10
Passivation	600 °C	1 h	FG	10

2.2.2 Rapid Thermal Process

Rapid thermal processing (RTP) is the counterpart of the tube furnace. This furnace can reach the same temperatures, however the process time is in the order of several seconds up to minutes, with a temperature ramp of 10 °C/s. This rapid heating is usually provided by lamps or lasers, depending on the furnace. In this project a Solaris 100 RTP is used, which utilizes 13 quartz halogen lamps on top and bottom of the sample. This double sided heating is applied to reduce non-uniform heating found on single sided systems [104]. The temperature is monitored by a sensor which is attached to a c-Si carrier wafer.

2.2.3 Hydrogen Plasma Passivation

Hydrogen plasma passivation uses plasma to create a reactive atomic hydrogen mixture, which is used for passivation. This is achieved by using H_2 as a precursor

gas in the PECVD setup. This has the previously mentioned benefits of PECVD with respect to temperature, which is expected to result in passivation at lower temperatures compared to RTP or TF passivation. The passivation is performed at a pressure of 12.5 mbar[1], and electrode distance of 10 nm, and afterwards the sample is cooled down in N_2 at 1.5 μbar.

2.3 Characterization

In this section all characterization procedures are described. First spectroscopic ellipsometry is explained, which is used for measuring the thickness of the sample. Next Fourier transform infrared spectroscopy is treated, for determining structural variations. Then Raman spectroscopy is discussed, which is the main focus of this thesis. It is used to determine the amount of crystallization of the Si NPs, and it is also used to both scale and measure PL. After that photothermal deflection spectroscopy is considered, which is a very sensitive method to determine the spectral absorption of the sample, giving insight into the defect density. Next X-ray photoelectron spectroscopy is explained, which is used for determining the composition of the different layers. Finally the dark conductivity setup is explained, used for determining the room-temperature conductivity of the sample. During all measurements the sample is handled with a tweezer while wearing cleanroom gloves.

2.3.1 Spectroscopic Ellipsometry

Spectroscopic ellipsometry (SE) characterizes the change in polarized light upon reflection of the sample. Light polarized parallel to the surface of the sample is called p-polarized, while light polarized perpendicular to the sample is called s-polarized. The amplitude ratio and phase difference between this p- and s-polarized light is measured. The measurement is most sensitive for a specific angle of incidence, which depends on the optical constants of the sample. Spectroscopic indicates that this measurement is performed at different wavelengths, resulting in more information about the sample. SE is especially useful for determining the thickness since the thickness sensitivity is in the order of 0.1 Å with conventional instruments [105]. Because of this SE is mainly used to determine the thickness of the multilayer stack.

A M-2000 J. A. Woollam Co. Inc. Spectroscopic Ellipsometer is used for SE measurements. For all measurements a photon energy range of 0.73 eV to 6.5 eV is used. The measurement angle range varies depending on substrate; 55°-70° for quartz substrates, and 65°-75° for c-Si wafer substrates. The angle range is scanned in 5° steps, and the sample is aligned at the center of the angle range. Because of the high transmittance of the quartz substrate, a piece of tape is applied to the backside in order to scatter backside surface reflections, which could interfere with the measurement.

[1] 12.5 mbar is the highest operating pressure of the used PECVD setup.

2.3.2 Fourier Transform Infrared Spectroscopy

Fourier Transform Infrared Spectroscopy, abbreviated as FTIR, is a technique that measures the infrared absorption spectrum of the sample. Instead of measuring the absorption at each wavelength separately, it illuminates the sample with a beam of many frequencies and measures the absorption. Repeating this with different frequency combinations, and using a Fourier transform, the signal is separated into absorption at each wavelength. Certain resonant frequencies of molecular structures ly in the infrared range, and infrared light with this frequency is absorbed by these molecular vibrations. Therefore by measuring the infrared absorption of the sample, information about the structure can be obtained. Theoretically the absorption spectrum should have discrete absorption lines, however the individual vibrational motions are usually accompanied by other rotational motions [87], resutling in absorption bands. Many absorption bands related to SiO_x have been identified, and it has been shown that FTIR can characterize the structural variations of SiO_x [106].

The Thermo Scientific Nicolet 5700 is used for obtaining the FTIR spectra. FTIR spectra are only measured of samples with a wafer substrate, since the infrared transmission of the quartz substrates is insufficient for effective measurements. The spectral range is set at 400-4000 cm^{-1}. Absorption peaks related to SiO_x are summarized in table 2.3.

Table 2.3: FTIR absorption peaks of various Si-O bonding modes and their wavenumber ranges. If only one value is presented in the wavenumber range, no range was specified.

Wavenumber range [cm^{-1}]		Mode	Reference	Remarks
457		Si-O-Si rocking	[107, 108]	
810		Si-O-Si bending	[109–113]	
965	1080	Si-O-Si asymmetric stretching TO	[62, 108–114]	With increasing $\frac{[O]}{[Si]}$: increasing wavenumber, increasing LO, decreasing FWHM
1200	1300	Si-O-Si asymmetric stretching LO	[108]	Typically shoulder of TO

2.3.3 Raman Spectroscopy

Raman spectroscopy relies on Raman scattering to obtain information about the composition of the sample. Raman scattering is inelastic scattering of a photon with the lattice of the material under investigation. This scattering results in a photon with a higher (Stokes shift) or lower (anti-Stokes shift) energy than the incident photon. The change in photon energy is either stored in, or released from phonons. Because monochromatic light is used as a light source, Raman scattering can be measured by a change in frequency. Raman scattering depends on the vibrational

modes of the lattice, which is unique to every lattice. Therefore Raman spectroscopy can provide insight into the structure and bonds in the sample, and is very sensitive to changes in the material structure.

Raman measurements are typically presented in Raman shift, which eases analysis of Raman phonon modes. The conventional way of presenting Raman shift is in cm^{-1}, and it can be calculated with the following relation:

$$\Delta w = \left(\frac{1}{\lambda} - \frac{1}{\lambda_{\mathrm{laser}}} \right) \cdot 10^7, \tag{2.3.1}$$

where λ and λ_{laser} are the wavelength of the backscattered and laser light in nanometres respectively. In this report, the Raman spectroscope is used for PL measurements, which are presented in eV. Conversion of Raman shift to eV is achieved with the following formula:

$$E = \frac{hc}{q} \left(\frac{1}{\lambda_{\mathrm{laser}}} - \Delta w \cdot 10^{-7} \right) \cdot 10^9, \tag{2.3.2}$$

where h is the Planck constant, c the speed of light and q the elementary charge.

The Renishaw inVia Raman microscope is used for all Raman measurements. This setup is configured in a back scattering geometry, with a grating of 1800 lines/mm. In all measurements an Ar-ion laser with a wavelength of 514 nm is used, unless specified otherwise. To make sure no contamination obstructs the measurement, the sample is cleaned with semiconductor grade ethanol and wiped with a cleanroom tissue prior to the measurement. All spectra are corrected for the sensitivity of the detector.

Since the multilayer structure is transparent, a significant part of the laser light reaches the substrate. This results in a contribution of the substrate in the measured data. A c-Si wafer substrate shows a strong c-Si TO mode, thereby hindering the determination of crystallinity. A quartz substrate also shows a signal in the same range, however it is much lower. Although both substrates are expected to contribute to the measured data, only samples with quartz substrate are used for this measurement, because of the lower contribution. Because the quartz is transparent, it is possible that the sample stage could also contribute, therefore the sample is positioned in such a way there is no material directly underneath the point of measurement. For determination of the crystallinity a matlab script written by de Grunt is used, with a γ factor of 0.8. For a detailed description of this fitting method, see de Grunt [115].

The Raman shift range is set at $100\,\mathrm{cm}^{-1}$ to $9438\,\mathrm{cm}^{-1}$, which is the maximum range, with an integration time of 30 s and one accumulation. The laser power is set at 32 µW, and the laser spot is approximately 12 μm in diameter. The used settings are considered sufficient for reduction of measurement errors, for a detailed error analysis see appendix B.1.

2.3.4 Photothermal Deflection Spectroscopy

Photothermal deflection spectroscopy (PDS) is a technique to accurately measure the wavelength dependent absorption coefficient. In this thesis a special kind of PDS is used, namely absolute PDS. This special setup is able to measure the absorption, reflection and transmission simultaneously on the same spot. This allows for precise correction of constructive and destructive interference in the thin films of the sample, and results in a more accurate absorption spectrum compared to other PDS techniques [116]. For a detailed description of this setup see Remes *et al.* [116].

In this thesis, PDS is mainly used to compare the wavelength dependent absorption coefficient, providing insight into the defect density of the material. This is distinguished by a change in sub-bandgap absorption. The photon energy range is set at 0.8 eV to 3.6 eV. Only quartz substrate samples are analysed with PDS since wafer substrates do not have a high transmission in the used spectral range. Because of the high sensitivity of this setup the sample is cleaned with semiconductor grade ethanol and wiped with a cleanroom tissue before positioning the sample in the setup.

2.3.5 X-ray Photoelectron Spectroscopy

X-ray Photoelectron Spectroscopy (XPS) is a technique to determine the elemental composition of the sample. In XPS, the sample is illuminated with an X-ray beam, and the kinetic energy and number of electrons emitted from the sample is measured. Using conservation of energy, the binding energy is calculated from the measured data. Elements have characteristic binding energies, and therefore produce characteristic XPS peaks. This makes identification of different elements possible. The relative intensities of the peaks directly show the relative amounts of each element.

To determine the composition of the different layers, a monolayer sample of each composition is created and measured with XPS. All XPS measurements are performed by M.W.G.M. Verhoeven of the department of Chemical Engineering and Chemistry of the Technical University of Eindhoven, using a Thermo Scientific K-Alpha setup. To remove contamination, the surface of the film is etched with an ion gun prior to measurements.

2.3.6 Dark Conductivity

The only electrical measurement technique used in this thesis is the dark conductivity setup. This setup supplies a given voltage V to two contacts on the sample, and measures the current I. Afterwards the conductivity σ can be calculated:

$$\sigma = \frac{d}{tl}\frac{I}{V}, \tag{2.3.3}$$

where d is the distance between the two contacts, t the thickness of the layer and l the length of the contacts. By repeating this measurement at different temperatures, the temperature dependent conductivity can be obtained:

$$\sigma(T) = \sigma_0 \exp\left(-\frac{E_{\text{act}}}{k_{\text{b}}T}\right), \tag{2.3.4}$$

where T is temperature, σ_0 is the pre-exponential factor, E_{act} the activation energy and k_{b} the Boltzmann constant. After the data collection, the data is fitted to obtain σ_0 and E_{act}. Then the conductivity at room temperature can be calculated using equation 2.3.4.

In order to control the temperature of the sample, the sample stage is equipped with a thermal controller. A voltage of 100 V is applied to the contacts, and the current is measured with a Keithley 6517A electrometer. The temperature range starts at 130 °C, which is the annealing temperature of the contacts, and then decreases with 10 °C steps to 60 °C. This measurement is performed both in the dark and in the light. Although the measurement in the light is not with a calibrated light source, it still gives an indication of light conductivity. Only quartz substrate samples are used for this measurement, since Si wafer substrates are conductive and would interfere with the measurement.

Photoluminescence Scaling & Modelling

3

First a scaling method is presented to scale an obtained photoluminescence spectrum, using a Raman spectroscope. Next multiple fitting functions are derived to fit the spectra, consisting of three parts; quantum confinement, interface state recombination and defects. For quantum confinement a detailed derivation is presented to relate the nanoparticle size distribution to the obtained spectra. Finally an error analysis is presented to support the used fitting function.

3.1 Photoluminescence Scaling

If we assume the minimum size of a Si NP is two atoms, it can be assumed that all Si-Si bonds reside inside the Si NPs. The total amount of Si-Si bonds does not change during phase separation or crystallization of a-Si, which makes this a constant. The amount of Si-Si bonds can be measured by measuring the phonon modes of Si. These phonon modes are measured with a Raman spectroscope, and by expanding the measured wavelength range, the PL spectrum can be obtained simultaneously. By dividing the measured spectrum y by the integrated intensity of the a-Si and c-Si TO mode, the PL is scaled to the amount of Si-Si bonds:

$$y_{\text{Si-Si}} = \frac{y}{\gamma I_{\text{TO,a-Si}} + I_{\text{TO,c-Si}}}. \tag{3.1.1}$$

Again γ is used to account for the difference in cross-section of the a-Si and c-Si TO mode excitations, which is set at 0.8 [80–82].

This poses a reliable scaling method, since all necessary information is obtained in a single measurement. Another benefit is that the PL spectrum, which is a bulk measurement, is related to the density of Si-Si bonds in the sample, which effectively indicates the NP density.

The scaling bypasses the effect of NP density and sample thickness on the PL intensity, as these factors both influence the amount of Si-Si bonds in the sample. The other factors influencing PL intensity include contamination, excitation power [54, 55], temperature [52, 56] and sample angle. Contamination is removed by cleaning the sample prior to the measurement. Excitation power and temperature are assumed to be constant because of the limited measurement time. And to establish the angle dependence of this method, an experiment must be performed.

3.2 Photoluminescence Modelling

To give a physical reasoning for the used fitting functions, a model is derived from theoretical and experimental data. As discussed in section 1.2.5, the PL mechanisms are divided into three types; QC, ISR and defects. For QC a theoretical model is derived to relate the PL spectrum to the size distribution of the NPs. For ISR and defects a normal distribution is used with specific limits to the fitting parameters, based on literature.

3.2.1 Quantum Confinement

In this section a derivation is presented for the photoluminescent NP size distribution, and the resulting PL spectrum. First the size distribution of the two possible structures is discussed: monolayer and multilayer. Then clustering of NPs is considered, as clustered NPs are believed to have a low PL intensity. Finally the fitting functions are presented, and some of the limits of the fitting parameters are discussed, which also depend on the phase of the Si NPs.

Size Distributions

It has been shown that individual NPs show atomic-like emissions, subject to quantum confinement [117]. In ensembles of NPs this sharp spectral feature is usually broadened, introduced by size variations of the NPs [117]. To model the PL of ensembles of NPs using QC as the PL mechanism, it is first necessary to elaborate on the size distribution, since it strongly influences QC.

The size distribution of the NPs depends on the structure of the sample. It is believed that in a monolayer structure, the NP size distribution follows a log-normal distribution [43, 118, 119], unless the growth process is not random but controlled [43]. The log-normal function is given by equation 3.2.1.

$$f_{\text{mono}}(a) = \frac{1}{a - a_{\min}} \exp\left[-\frac{(\ln(a - a_{\min}) - \mu_l)^2}{2\sigma_l^2}\right] \tag{3.2.1}$$

μ_l and σ_l are shape parameters, governing the peak position and width respectively. $a_{\min}$ is a location parameter, shifting the distribution, and it defines the minimum NP size. Because of the factor $\ln(a - a_{\min})$ this function only exists for $a > a_{\min}$. This function is not normalized by integration and equating to 1; $\int f(a)\,\mathrm{d}a = 1$, since the amplitude of this function will be fitted, thereby making normalization redundant.

For a multilayer structure, the Si-rich layer thickness strongly limits the maximum NP size [4, 47, 66, 67, 75]. For a single Si-rich layer inside a multilayer stack, a logit-normal distribution is expected, which is a function with two boundaries, given by equation 3.2.2:

$$f_{\text{single}}(a, L) = \frac{1}{(a - a_{\min})(L - a)} \exp\left[-\frac{(\ln(\frac{a-a_{\min}}{L-a}) - \mu_l)^2}{2\sigma_l^2}\right], \tag{3.2.2}$$

where L represents the maximum diameter of the NP, which is the Si-rich layer thickness. μ_l and σ_l govern the peak position and width respectively. Because of the factor $\ln(\frac{a-a_{\min}}{L-a})$ this function only exists for $a_{\min} < a < L$. Please note that this function is again not normalized. The log-normal and logit-normal distributions are illustrated in figure 3.1.

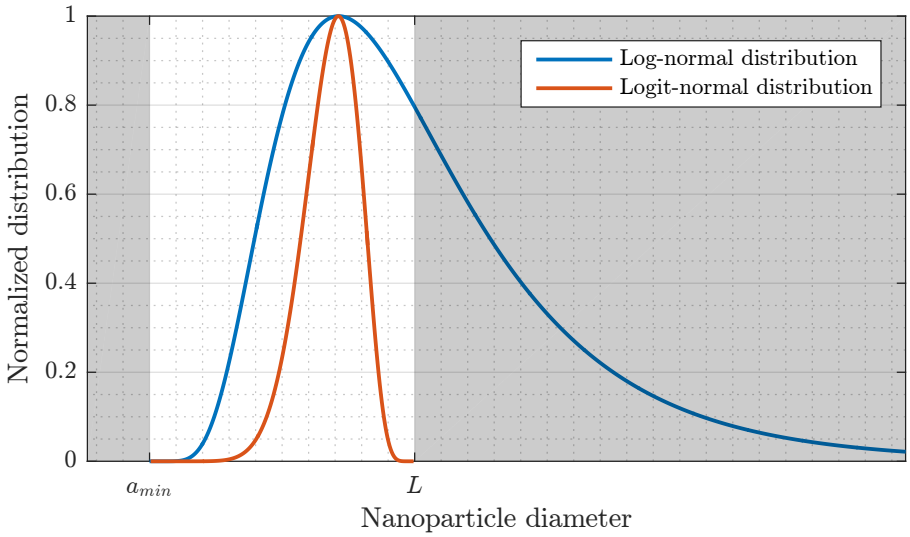

Figure 3.1: The log-normal and logit-normal distributions, both normalized at their maximum. Both functions start at $a_{\min}$, and only the logit-normal function is limited by L. The values of μ_l and σ_l are arbitrary.

When measuring the PL of a multilayer structure, the PL of all layers is measured simultaneously. Hence the PL spectrum is the sum of the PL spectrum of each layer. If the size distribution varies among these layers, the PL spectrum will also vary. A difference in size distribution could occur because of a different Si-rich layer thickness.

The Si-rich layer thickness is set during the deposition, however there is a certain spread in the final layer thickness, since the deposition has limited precision. Therefore it is expected that the Si-rich layer thickness follows a normal distribution, given by equation 3.2.3. μ_n is the mean, which represents the imposed layer thickness, and σ_n is the standard deviation, which is set at 0.3 nm, determined from TEM images of multilayer samples, see appendix A.1.

$$G_{\text{layer}}(L) = \frac{1}{\sigma_n\sqrt{2\pi}} \exp\left[-\frac{(L - \mu_n)^2}{2\sigma_n^2}\right] \tag{3.2.3}$$

For a multilayer in which the Si-rich layers are in the order of nanometres, this variation is significant. The size distribution of NPs for a multilayer is therefore more complicated than for a monolayer. It is calculated by multiplying equation 3.2.2 with equation 3.2.3, and integrating over L:

$$f_{\text{multi}}(a) = \int_{a_{\min}}^{\infty} f_{\text{single}}(a, L) G_{\text{layer}}(L)\, \mathrm{d}L. \tag{3.2.4}$$

Probability of Isolated Nanoparticles

Large NPs are believed to have low PL intensity because of reduced QC [25, 26, 32, 120, 121]. The larger surface area also results in a higher chance on non-radiative surface defects [122]. Clustered NPs are basically large NPs, therefore they are expected to have a low PL intensity as well, hence can be neglected when fitting the PL spectrum. To account for clustering this section will elaborate upon the probability that a NP is isolated, i.e. not clustered. Although the presented derivation is based on c-Si NPs, the same derivation can be performed for a-Si NPs. This calculation is based on a theoretical model derived by van Sebille *et al.* [123]. First the total atomic density of the Si-rich layer ρ_{layer} is necessary, given by:

$$\rho_{\text{layer}} = \Gamma_{\text{c-Si}}\rho_{\text{c-Si}} + \Gamma_{\text{a-Si}}\rho_{\text{a-Si}} + \Gamma_{\text{SiO}_2}\rho_{\text{SiO}_2}, \tag{3.2.5}$$

where $\rho_{\text{c-Si}}$ and $\rho_{\text{a-Si}}$ are the atomic densities of c-Si and a-Si respectively, and ρ_{SiO_2} is the molecular density of SiO_2. $\Gamma_{\text{c-Si}}$, $\Gamma_{\text{a-Si}}$ and Γ_{SiO_2} are the atomic and molecular percentages, given by the following relations.

$$\Gamma_{\text{c-Si}} = X_{\text{c}} \left(1 - \frac{x}{2}\right) \cdot 100\% \tag{3.2.6}$$

$$\Gamma_{\text{a-Si}} = (1 - X_{\text{c}}) \left(1 - \frac{x}{2}\right) \cdot 100\% \tag{3.2.7}$$

$$\Gamma_{\text{SiO}_2} = \frac{x}{2} \cdot 100\% \tag{3.2.8}$$

Here x is the $\frac{[\text{O}]}{[\text{Si}]}$ fraction in the composition of the deposited Si-rich layer, SiO_x. X_{c} is the crystallinity of the annealed layer. Now the atomic density of the c-Si in the layer can be calculated:

$$\rho_{\text{c-Si,layer}} = \Gamma_{\text{c-Si}}\rho_{\text{layer}}. \tag{3.2.9}$$

This results in the total c-Si NP density, $n_{\text{c-Si}}$, given by:

$$n_{\text{c-Si}} = \frac{\rho_{\text{c-Si,layer}}}{N_{\text{c-Si,NP}}} a, \tag{3.2.10}$$

where $N_{\text{c-Si,NP}} = \frac{1}{6}\pi a^3 \rho_{\text{c-Si}}$ is the number of atoms in a c-Si NP. For simplicity $n_{\text{c-Si}}$ is assumed to be independent of NP size, which is achieved by fixing a

at the mean NP size. For a monolayer the mean NP size can be calculated with $exp\left[(\mu_l + \sigma_l^2)/2\right]$. For a multilayer the mean is not analytically defined, however the mean NP size is likely to be close to the Si-rich layer thickness, hence for simplicity $a = L$ is taken. Finally the probability that a NP is isolated, i.e. not clustering, is given by the following two equations [124]. Equation 3.2.11 holds for a monolayer, and equation 3.2.12 for a multilayer, which again depend on the NP diameter a.

$$P_{\text{i,mono}}(a) = \exp\left[-\frac{6\rho_{\text{c-Si,layer}}}{\rho_{\text{c-Si}}\exp\left[(\mu_l + \sigma_l^2)/2\right]^2}\left(\frac{a}{2}\right)^2\right] \tag{3.2.11}$$

$$P_{\text{i,multi}}(a) = \exp\left[-\frac{6\rho_{\text{c-Si,layer}}}{\rho_{\text{c-Si}}L^2}\left(\frac{a}{2}\right)^2\right] \tag{3.2.12}$$

Fitting Functions

Now that the size distributions and the probability of isolated NPs is known, the size distribution of photoluminescent NPs can be calculated. The size distribution of photoluminescent NPs in a monolayer and a multilayer are obtained by the multiplication of 3.2.11 with equation 3.2.1, and 3.2.12 with 3.2.4.

$$F_{\text{mono}}(a, \mu_l, \sigma_l) = P_{\text{i,mono}}(a) f_{\text{mono}}(a, \mu_l, \sigma_l) \tag{3.2.13}$$

$$F_{\text{multi}}(a, \mu_l, \sigma_l) = P_{\text{i,multi}}(a) f_{\text{multi}}(a, \mu_l, \sigma_l) \tag{3.2.14}$$

The fitting parameters of these two functions are μ_l and σ_l, which are the shape parameters of the log-normal and logit-normal distributions. The limits for μ_l are set at -3 and +3 respectively, and σ_l is allowed to vary between 0.03 and 3. These values are chosen to make sure that the distribution does not become incredibly sharp, however the limits are rather arbitrary.

Now that the photoluminescent size distribution is known, the NP size needs to be related to the emission energy. A quantum mechanical derivation was presented in section 1.2.1, resulting in equation 1.2.10. This derivation does not represent experimental data very well, see figure 3.2. For this reason the PL peak position is fitted with the following function:

$$E_{\text{g}} = E_{\text{bulk}} + \frac{1}{\alpha m_0}\frac{3\hbar^2\pi^2}{2a^2}, \tag{3.2.15}$$

here α is the fitting parameter, which together with m_0 forms the effective mass m^*. Fitting this function to experimental data results in $\alpha = 0.45 \pm 0.06$, which is very close to the theoretical value of 0.48. The difference between the derivation and the fit is thus very small, see figure 3.2.

Although neither the derivation nor the fit describe the experimental data well, there is no physical reason to use a different function. A derivation presented by

Conibeer *et al.* [15], based on the same quantum mechanical derivation, resulted in the yellow line in figure 3.2, and is also considered inadequate. Therefore the original derivation, described in section 1.2.1, will be used for bandgap calculations of Si NPs.

The NP diameter a thus is related to the energy by equation 3.2.16. For clarity the result of equation 3.2.16 is not presented in equation 3.2.13 or equation 3.2.14, since this would result in two very complex functions.

$$a(E_g) = \sqrt{\frac{3\pi^2\hbar^2}{2m^*(E_g - E_{bulk})}} \tag{3.2.16}$$

The presented derivation is valid for both a-Si and c-Si NPs. However the minimum particle size a_{min} and bulk bandgap E_{bulk} are different for these two phases, which is discussed in the following two paragraphs.

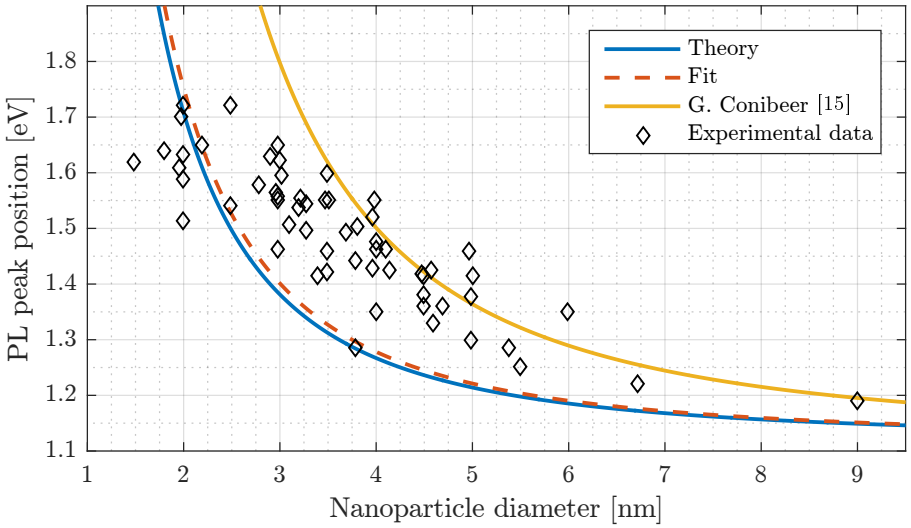

Figure 3.2: The theoretical and fitted PL peak position as function of NP diameter. The yellow line represents a model derived by Conibeer *et al.* [15]. The experimental data is extracted from figure 1 of Küsová *et al.* [83]

Amorphous Nanoparticles

In literature no minimal size of a-Si NPs is reported. It is therefore assumed that the minimal size of a-Si NPs is two atoms, which will distinguish a-Si from the SiO_2 matrix. The atomic radius of silicon is emperically determined to be 0.11 nm [125], which results in a minimal NP size of $a_{min} = 0.2\,\text{nm}$.

The bandgap of bulk a-Si is less well defined compared to the bandgap of bulk c-Si. This makes it difficult to directly relate the NP diameter a to the emission

energy E_g. Since the PL emission of bulk a-Si shows a spread which resembles a normal distribution, a normal distribution is used to define the bandgap:

$$F_{\text{norm}}(E) = \frac{1}{\sigma_n\sqrt{2\pi}} \exp\left[-\frac{(E-\mu_n)^2}{2\sigma_n^2}\right]. \tag{3.2.17}$$

The mean μ_n and standard deviation σ_n are set at 0.1 eV and 1.26 eV respectively. These values have been extracted from experimental data of a-Si:H by Street [126]. This results in the following relation for NP diameter and emission energy:

$$a(E_g) = \sqrt{\frac{3\pi^2\hbar^2}{2m^*}} \int_0^{E_g} (E_g - E)^{-\frac{1}{2}} F_{\text{norm}}(E)\,\mathrm{d}E. \tag{3.2.18}$$

Crystalline Nanoparticles

Since the critical nucleation radius for crystalline silicon is calculated to be approximately 0.57 nm [64, 65], the minimal NP diameter a_{min} is set to 1.14 nm. Because of the well defined bandgap of c-Si, no normal distribution is necessary to represent it. The bandgap of bulk c-Si, E_{bulk}, is therefore set at 1.12 eV.

3.2.2 Interface State Recombination

As mentioned before, ISR will be fitted with a normal distribution, given by equation 3.2.17. As shown in figure 1.8, the peak position is reported between 1.3 eV and 1.7 eV. In literature no continuous band is reported, however for simplicity it is assumed that the ISR peak position can vary between the previously mentioned values, therefore $1.3\,\text{eV} \leq \mu_n \leq 1.7\,\text{eV}$. The standard deviation is not reported in literature. However instead of not limiting this parameter, some limits are chosen; $0.01\,\text{eV} \leq \sigma_n \leq 0.2\,\text{eV}$, based on reported data of several defects, see table A.1.

3.2.3 Defects

As presented in section 1.2.5, there are many photoluminescent defects reported in literature. Generally these defects are approximated with a normal distribution as given by equation 3.2.17. A selection of the most relevant defects, and the limits for μ_n and σ_n are presented in table 3.1.

Table 3.1: Reported photoluminescent defects in Si NPs embedded in SiO_2 at room temperature, and the limits to the two fitting parameters. If only one value is given, only one value was reported, and the fitting parameter is fixed.

Defect	μ_n limits [eV]		σ_n limits [eV]		References
Si=O		1.66	0.12	0.16	[34]
NBOHC		1.91	0.02	0.15	[24, 35, 36]
Si/SiO_2 interface	2.06	2.07		0.25	[10, 29, 37]

3.3 Fitting Procedure

Now that all fitting functions are described, the fitting procedure can be specified. In literature the PL spectrum is occasionally a combination of multiple contributions [11, 20–22, 29, 127, 128]. Thus it is reasonable to combine the described fitting functions into one function, F_{tot}:

$$F_{\text{tot}} = \sum_i \alpha_i F_{\text{i}}, \tag{3.3.1}$$

where α_i is the amplitude of the fitting function F_{i}. The subscript i indicates the different fitting functions, i.e. PL contributions.

By using more fitting functions, there are more fitting parameters, which could result in overfitting. To make a grounded decision for which functions to combine, a fitting error analysis is performed. By fitting the same spectrum with different combinations of PL contributions, it is possible to determine which are important and which are superfluous. When the mean square error (MSE) decreases drastically the added fitting function could be important.

For this analysis a representative PL spectrum is fitted with different combinations of fitting functions. This sample is an annealed multilayer sample with Si-rich layer composition of $SiO_{0.9}$, Si-rich layer thickness of 3 nm, and a buffer layer thickness of 1 nm. The result of this analysis is shown in figure 3.3.

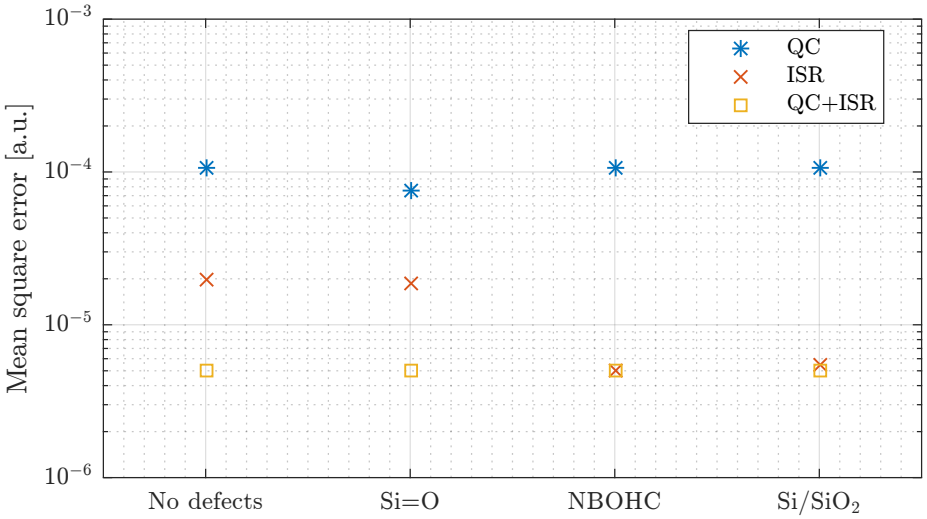

Figure 3.3: The MSE of different fitting functions. The labels on the x-axis represent added functions to the main fitting functions, which are indicated by the legend.

As expected the MSE decreases when the number of fitting functions increases. QC on its own is not enough to obtain a good fit, and even with added defects it still produces a large MSE. ISR shows good results, especially in combination with the NBOHC or the Si/SiO_2 interface defect function. This indicates that there is some contribution present around the 2 eV. When QC and ISR are combined the MSE does not change significantly anymore when defect functions are added.

The best result with the least amount of fitting parameters is obtained with the ISR function together with either the NBOHC function or the Si/SiO_2 defect function. The NBOHC is one of the best characterized defects in SiO_2 and is therefore chosen instead of the Si/SiO_2 defect. The ISR-NBOHC fit is shown in figure 3.4. However, although a good fit is produced, it does not mean that the results are interpreted correctly. As shown in figure 3.3 many combinations result in a good fit, complicating the interpretation. The fact that the ISR fitting parameters have rather large limits also indicates that the ISR function can fit many datasets. For this reason the ISR-NBOHC function will mainly be used to give an indication of the low and high energy contributions, between 1.3 eV to 1.7 eV and around 2 eV respectively.

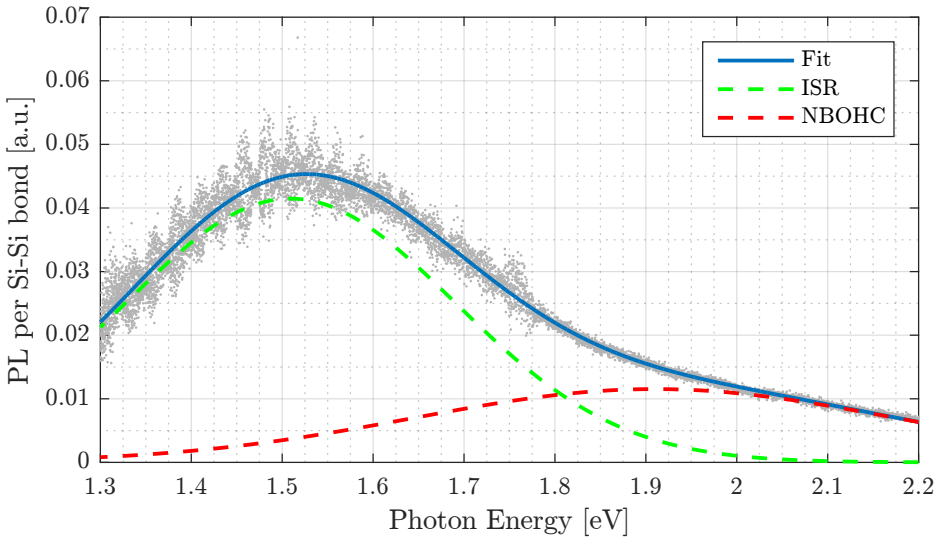

Figure 3.4: The PL spectra per Si-Si bond of an annealed multilayer sample with Si-rich composition of $SiO_{0.9}$ and thickness of 3 nm. The grey datapoints are the original data, the solid blue line is the obtained fit. The green and red dashed lines are the ISR and NBOHC fit function respectively.

Results & Discussion

4

The presented method and model are applied to experiments, divided into four groups; validation, passivation of dangling bonds, excess silicon content and Si-rich layer thickness. First some validating experiments are presented, testing the scaling method. Next passivation, excess silicon content and the Si-rich layer thickness are investigated, since these influence the PL spectrum and intensity. At the end of each section the presented results are discussed.

4.1 Validation

In this section two experiments are performed to validate the described scaling method. First two different excitation wavelengths are used in order to distinguish between Raman phonon modes and the PL spectrum. Next a sample is deliberately misaligned in order to measure at different angles.

4.1.1 Excitation Wavelength

By exciting the sample with a different laser wavelength, Raman phonon modes can be distinguished from PL. The position of the Raman phonon modes is independent of excitation wavelength when expressed in Raman shift. PL however, is expected to remain in the same wavelength range, i.e. when expressed in Raman shift the PL peak shifts if the excitation wavelength is changed, see equation 2.3.1.

Experimental Details

For this experiment two different laser excitation wavelengths are used: 514 nm and 633 nm. The intensity of these two lasers are different, however it is not expected to influence the result of this experiment. Two multilayer samples with Si-rich composition of $SiO_{0.9}$ are measured; one annealed and one TF passivated at 600 °C.

Results

The result of this experiment is presented both in Raman shift and eV, see figure 4.1. In the 514 nm excited spectra the peak of the c-Si TO mode, positioned at 520 cm^{-1} [80], is clearly visible, see figure 4.2. The features below 520 cm^{-1} are attributed to a-Si phonon modes. These modes indeed remain at the same position when expressed in Raman shift, see figure 4.1**(a)** and **(b)**. The broad peak above 2000 cm^{-1} does shift, indicating that it is PL and not a Raman phonon mode. Since a passivated sample has a lower defect density and thus a higher PL intensity, the shift in PL is

more pronounced in figure 4.1**(b)**. When expressed in eV, the phonon modes shift while the PL peak remains similar, see figure 4.1**(c)** and **(d)**.

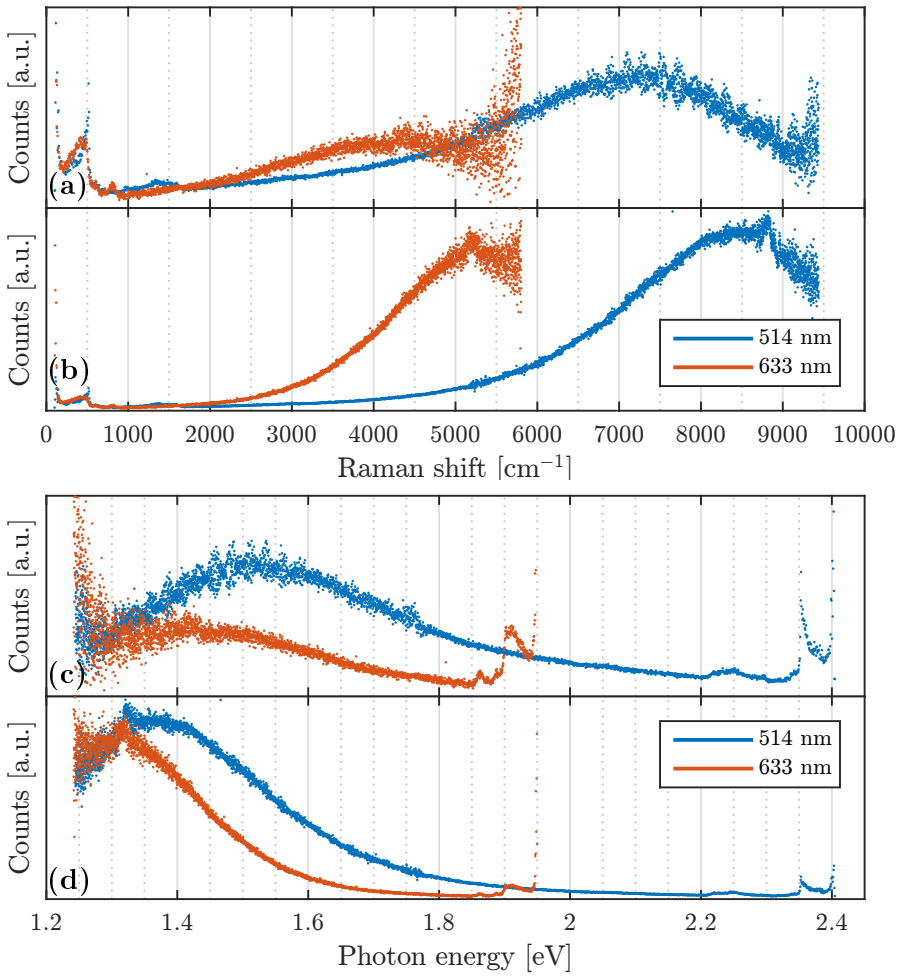

Figure 4.1: The Raman spectra measured with different excitation wavelength, expressed in Raman shift, **(a)** and **(b)**, and eV, **(c)** and **(d)**. Figures **(a)** and **(c)** represent the spectra of an annealed sample, and figures **(b)** and **(d)** represent a TF passivated sample. The intensity of the datasets are scaled in order to make comparison of the Raman phonon modes easy, therefore no values on the y-axis are given. Only one third of the datapoints is presented for clarity.

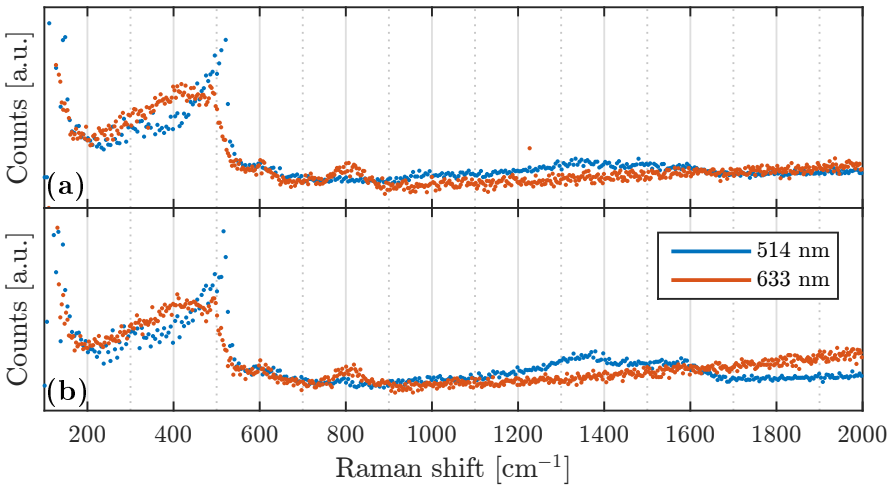

Figure 4.2: The Raman spectra below 2000 cm^{-1} expressed in Raman shift of an annealed sample **(a)** and TF passivated sample **(b)**, measured with different laser excitation wavelengths, indicated by the legend. The intensity of the two datasets are scaled in order to make comparison of the Raman phonon modes easy, therefore no values on the y-axis are given. Only one third of the datapoints is presented for clarity.

Discussion

A clear shift is visible in the peak above 2000 cm^{-1}, indicating that it is PL and not a Raman phonon mode. What stands out is that in the spectra excited with a 633 nm excitation wavelength, the shape of the a-Si and c-Si modes is different. This can be explained by a lower absorption coefficient in the multilayer at 633 nm, compared to 514 nm. This results in more signal from the substrate. The substrate is quartz, which shows phonon modes associated with the symmetric and asymmetric bending of SiO_2 around an below 500 cm^{-1} [87], see figure 4.3. Therefore a signal from the substrate will interfere with the a-Si and c-Si TO modes, and effectively reduce the c-Si peak which is clearly visible in the 514 nm excited spectra.

Another mode is visible around 800 cm^{-1}, more pronounced in the 633 nm excited spectrum, see figure 4.2. This is again a mode originating from the substrate, see figure 4.3, and is attributed to the stretching mode of SiO_2 [87, 129]. The peaks between 1000 cm^{-1} to 1250 cm^{-1} in figure 4.3 are associated with the asymmetric stretching mode of SiO_2 [62, 108–114].

In the 514 nm excited spectra, another contribution is present around 1400 cm^{-1}, more pronounced in figure 4.2**(b)**. These peaks are not evident from the 633 nm excited spectra, which indicate it originates from the multilayer. They could be attributed to O-O stretching vibrations, caused by interstitial O_2 [130]. However, since the composition of both the Si-rich and buffer layers only contain silicon suboxides, i.e. oxygen poor silicon oxide, it is unlikely that interstitial oxygen can form. It

is more likely that it is a hydrogen related mode, since the intensity is higher after passivation, however these modes are often positioned around 2000 cm^{-1} [129].

The PL peak shifts to lower energy when exciting with a longer excitation wavelength, see figure 4.1**(c)** and **(d)**. This can be explained by the fact that low energy states are more easily excited than high energy states, resulting in a shift to lower energy when reducing the excitation energy.

Since the 633 nm laser results in more signal from the substrate, and reduces the measurement range, the 514 nm laser is used for all other experiments. Above 1700 cm^{-1} no other phonon modes are visible, and therefore the signal beyond 1700 cm^{-1} is attributed to PL only, which roughly corresponds to a photon energy of 2.2 eV when excited with a 514 nm source.

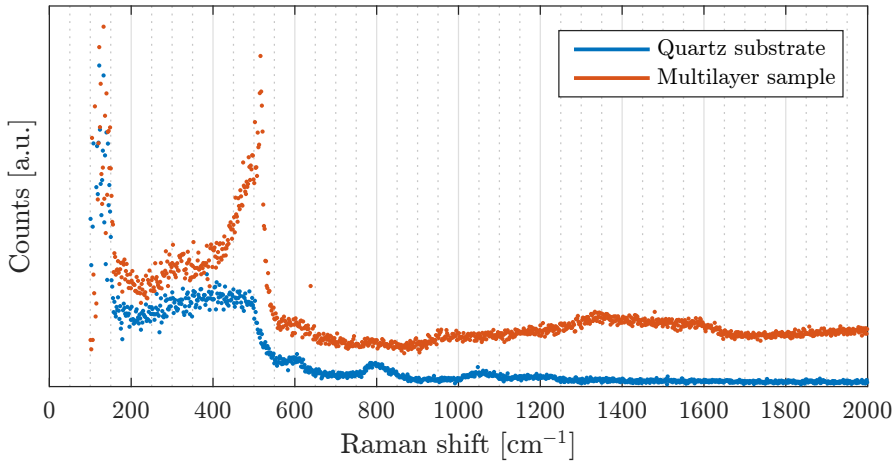

Figure 4.3: The Raman spectra of a bare quartz substrate and a multilayer sample deposited on a quartz substrate, excited with a 514 nm laser. The composition of the Si-rich layer in the multilayer sample is $SiO_{0.9}$. The intensity of the data is scaled for clarity.

4.1.2 Misalignment Angle

As discussed in section 1.2.5, one of the reasons that direct comparison of PL intensity is doubtful is the possibility of misalignment. Misalignment could result in an increased reflection of the excitation beam, resulting in a different intensity. The misalignment angle β is schematically shown in figure 4.4. In the Raman setup, the detector is optically positioned behind the lens, which means that the backscattered light needs to enter the lens in order to reach the detector. It is therefore expected that the signal intensity decreases with increasing angle, which leads to a low signal to noise ratio.

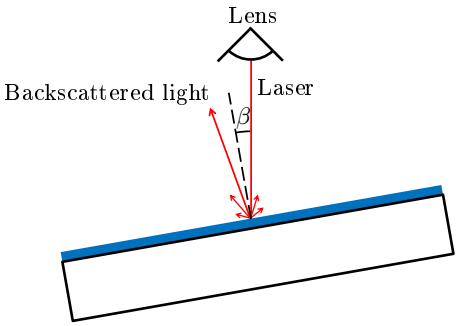

Figure 4.4: Schematic of the misalignment angle during a Raman measurement.

Experimental Details

An annealed multilayer sample with Si-rich layer composition of $SiO_{0.9}$ is measured at four different angles. The angle is set by placing a 300 μm thick c-Si wafer partly beneath the measured sample. The angle is calculated from the horizontal distance between the point of contact of the sample on the sample stage, and the point of contact of the sample on the c-Si wafer. The measurement error of this method is estimated at 2°.

Results

The effect of misalignment of the sample is presented in figure 4.5. No significant change in spectrum is visible, unless the angle becomes larger than 7°±2°. This is also supported by the fact that in figure 4.5b, the differences in integrated intensities are insignificant compared to the error margins, up to an angle of at least 7°±2°.

Discussion

No significant change is seen in figure 4.5 for angles up to 7°±2°, and the differences are insignificant compared to the error margins of the measurement. At an angle of 15°±2° the signal intensity is very low, which could be attributed to the fact that in the Raman setup, the backscattered light needs to enter the lens in order to reach the detector. At a misalignment angle of 15°±2° most of the backscattered light does not enter the lens, resulting in a very low signal to noise ratio.

A misalignment of more than 7°±2° is not expected since the sample is cleaned prior to the measurement, and the sample stage is flat. This experiment shows that the presented method is a reliable scaling method, which can overcome sample misalignment to a certain extent.

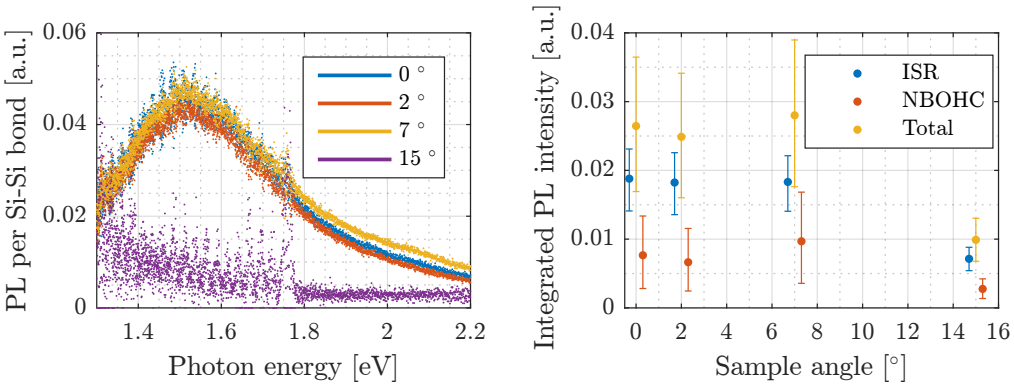

Figure 4.5: The PL spectra per Si-Si bond **(a)** and integrated intensities **(b)** for different misalignment angles. In figure **(a)** only one third of all datapoints is shown for clarity. The horizontal offset in the datapoints in figure **(b)** is for clarity.

4.2 Passivation of Dangling Bonds

As explained in section 1.2.5, passivation of dangling bonds is believed to increase PL of Si NPs. In this experiment three passivation techniques are considered; tube furnace passivation, rapid thermal process passivation and hydrogen plasma passivation. These techniques are performed at three different temperatures. The PL spectra are used to distinguish changes in the electronic structure, while FTIR is used to identify structural variations. PDS is considered to identify changes in absorption, with special interest in sub-bandgap absorption as it indicates changes in defect densities. First TF and RTP passivation are presented, then hydrogen plasma passivation is presented.

4.2.1 Tube Furnace & Rapid Thermal Process Passivation

Experimental Details

For these experiments multilayer samples are used with a Si-rich layer composition of $SiO_{0.3}$ and buffer layer composition of $SiO_{1.3}$. The Si-rich layer thickness is 1.2 nm, and the buffer layer thickness is 2.4 nm. Hydrogen passivation using furnaces is commonly performed between 400 °C to 500 °C [11, 13, 33, 53, 131]. Therefore this experiment is performed at 400 °C. 600 °C is also investigated since higher temperatures are expected to decrease the P_b center density further, and temperatures as high as 650 °C have been used in literature [132]. Lower temperatures require less energy, which is interesting for production processes, and consequently 200 °C is also considered. The settings for the TF and RTP passivation are presented in table 4.1.

Table 4.1: Passivation settings for the TF and RTP.

Process	Maximum temperature [°C]	Time at maximum temperature [min]	Gas	Gas flow [slm]
TF	200	60	FG	10
	400	60	FG	10
	600	60	FG	10
RTP	200	10	FG	8
	400	10	FG	8
	600	10	FG	8

Results

In figure 4.6**(a)** the PL spectra after tube furnace annealing (TFA) and subsequent TF passivation are shown. A clear increasing trend is visible with increasing passivation temperature. Passivation at 200 °C shows a strong increase in PL, while 400 °C only shows a minor change, compared to 200 °C. Passivation at 600 °C shows an even further increase in PL, mainly of the low energy contribution. This is illustrated in figure 4.7**(a)**, where the integrated intensities of the low and high energy contributions are presented.

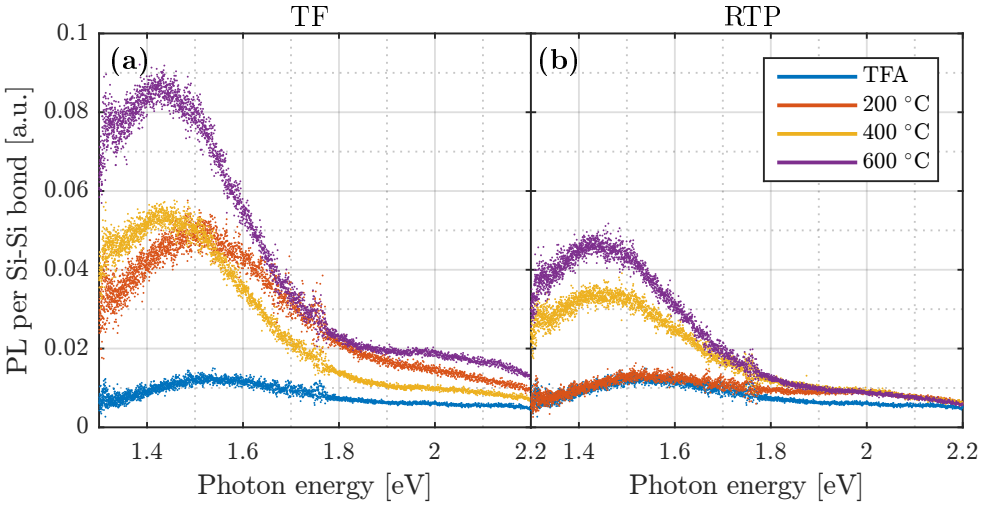

Figure 4.6: The PL spectra per Si-Si bond after TFA and each passivation temperature, indicated by the legend. Figures **(a)** and **(b)** represent the TF passivated and the RTP passivated series, respectively. Only one third of all datapoints is shown for clarity.

The PL spectra after RTP passivation are shown in figure 4.6**(b)**. What is evident, is that the overall intensity is lower, compared to TF passivation. Mainly the low energy contribution increases, and it shows an increasing trend with increasing

passivation temperature, presented in figure 4.7**(b)**. Interestingly, no significant change in PL is visible after passivation at 200 °C, while for TF passivation a strong increase is already visible at this temperature. What stands out is that even at low temperature, TF passivation increases the integrated intensity to a greater extend than high temperature passivation with RTP passivation, which is also visible when looking at the PL spectra, figure 4.6. The total integrated intensity is plotted in figure 4.8, where again a strong difference in intensity is visible.

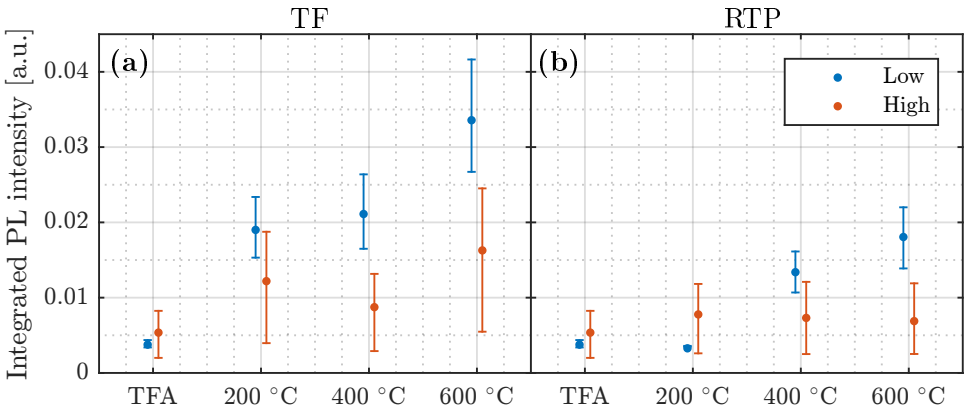

Figure 4.7: The integrated intensities of the low and high energy contributions after the different processes, indicated by the x-axis. Figures **(a)** and **(b)** represent the TF passivated and RTP passivated series.

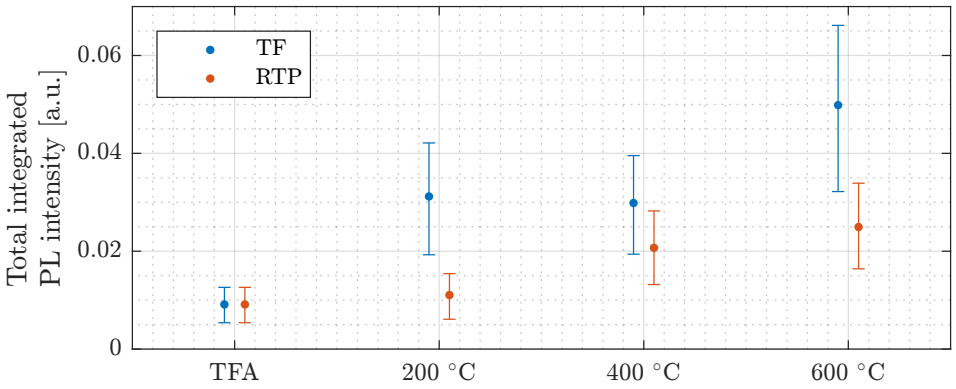

Figure 4.8: The total integrated PL intensity after the different processes, indicated by the x-axis and the legend. The error bars show the standard deviation.

The peak position of the low energy contribution is presented in figure 4.9. For both passivation processes a clear decrease in peak position is visible with increasing

passivation temperature. Interestingly a distinct step is visible between 200 °C and 400 °C. For all passivation temperatures, TF passivation shows a larger decrease in peak position, compared to RTP passivation.

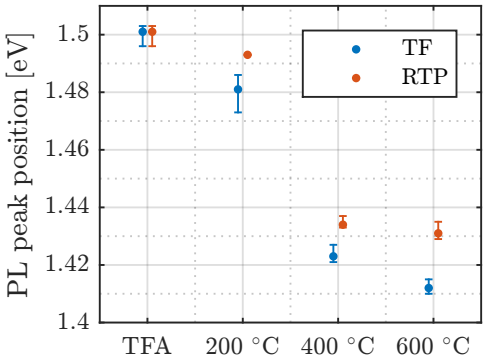

Figure 4.9: The peak position of the low energy contribution after the different processes, indicated by the x-axis and the legend. The error bars show the standard deviation.

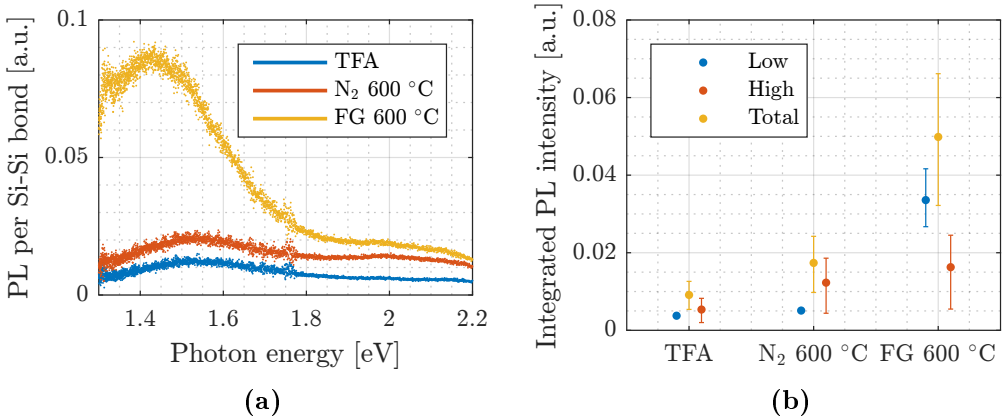

Figure 4.10: The PL spectra per Si-Si bond **(a)** and the integrated intensities **(b)** of as annealed (TFA), annealed at 600 °C (N_2 600 °C) and passivated at 600 °C (FG 600 °C). In figure **(a)** only one third of all datapoints is shown for clarity.

To examine whether the change in integrated intensity is caused by passivation or a change in composition, one sample is also annealed in N_2 gas at 600 °C after the initial annealing step. The resulting PL spectrum is shown in figure 4.10**(a)**, together with the spectra after TFA and after TF passivation at 600 °C. Although a slight overall increase is visible after annealing at 600 °C, the measurement error

is significant, see figure 4.10**(b)**. Passivation at 600 °C clearly shows a much greater change in intensity.

To examine changes in the composition of the material, FTIR spectra are measured. One set of spectra is shown in figure 4.11, where the roman numerals indicate different peaks. Peak (i) is associated with Si-O-Si bending [109–113]. In the as deposted spectrum, peak (i) consists of two contributions, the Si-O-Si bending as well as $Si{=}H_2$ related bending modes, which are positioned around 890 cm^{-1} [129]. Peaks (ii) and (iii) are the Si-O-Si asymmetric stretching TO and LO respectively [62, 108–114]. Peak (iii) clearly forms the shoulder of peak (ii), which is also reported in literature [108]. Peak (iv) consists of several contributions, which are likely to be Si-H or $Si{=}H_2$ related stretching modes [129].

A large change is visible between as-deposited and after annealing. Mainly SiO_2 modes increase, and all hydrogen related modes disappear. No significant change is present after passivation at 600 °C, compared to TFA, and interestingly no increase in hydrogen related modes is visible. In fact, none of the processes after annealing showed a significant effect on the FTIR spectrum, and therefore no other spectrum is shown. The crystallinity reached after the initial annealing step is 0.37 ± 0.004, and no significant change is visible after subsequent passivation.

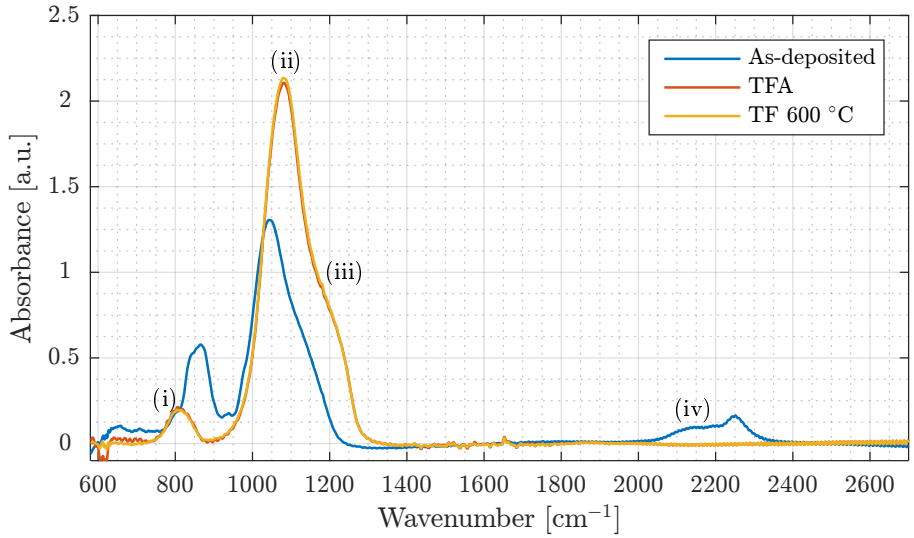

Figure 4.11: The FTIR absorption spectrum of as-deposited, TFA, and after TF passivation at 600 °C. The roman numerals indicate different peaks.

The results of the PDS measurements are presented in figure 4.12. The result of the 600 °C TF passivated sample is shown, together with as-deposited and TFA. First a strong increase in absorption is visible after annealing, however passivation does not result in a significant change. None of the passivation techniques resulted

in a significant change in sub-bandgap absorption, and therefore no other PDS measurements are shown.

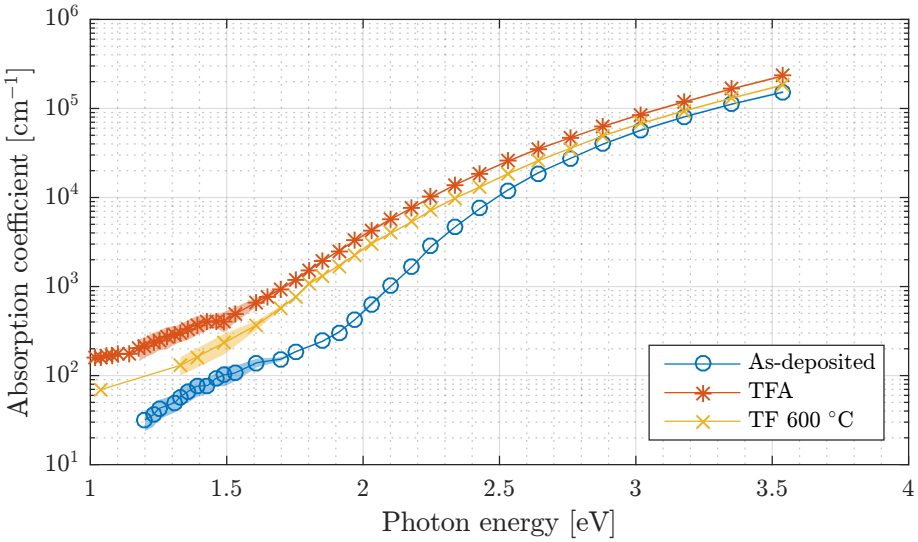

Figure 4.12: The spectral absorption coefficient of as-deposited, TFA, and after TF passivation at 600 °C. The shaded area behind the lines, visible at low photon energies, represents the standard deviation.

Discussion

Remarkably, the PL spectra after TF passivation at 200 °C and 400 °C show a similar intensity. This is contrary to the expectation that passivation increases with temperature, and mainly influences low energy PL because of the higher chance off surface defects for large NPs [122]. The fact that this trend is not visible in the RTP passivation series, and the Si-rich layer composition experiment which will be presented in section 4.3, indicates that the scaling of the PL spectrum of the TF passivation at 200 °C sample is wrong. The large step in peak position between 200 °C and 400 °C, which is visible for both TF and RTP passivation, also suggests that the intensity should follow a similar trend, which supports the conclusion. For this reason the intensity of this measurement is neglected.

All TF passivation processes and RTP passivation processes above 200 °C show both an increase in PL intensity, as well as a relative increase of the low energy contribution. The increase in the low energy contribution indicates passivation of P_b centers. This is supported by the shift in peak position: the peak of the low energy contribution shifts toward lower energy for higher passivation temperature, presented in figure 4.9. This can be explained by QC; large NPs have a higher chance off surface defects, and by passivation these defects are removed, resulting in an increase in the contribution of large NPs, which have a lower bandgap. The

step between 200 °C and 400 °C, and the small difference between 400 °C and 600 °C, indicates that temperatures in excess of 200 °C are necessary for efficient passivation of P_b centers. This is supported by the negligible change in intensity between TFA and 200 °C passivation, see figure 4.7**(b)**.

Between 400 °C and 600 °C, the peak shifts slightly, while the integreated intensity of the low energy contribution still increases significantly. These two effects suggest that the size distribution of photoluminescent NPs remains similar, while the amount of photoluminescent NPs increases. Hence the distribution of P_b centers among NPs remains similar, while the amount of P_b centers decreases. It also suggests that higher temperatures result in faster passivation.

The peak position after RTP passivation is higher than for TF passivation at each temperature, which demonstrates that longer passivation results in a lower P_b center density. The fact that the integrated intensity of the low energy contribution after TF passivation is higher than after RTP passivation supports this idea. The beneficial effects of a larger thermal budget, defined as the integral of temperature over time, have also been reported in literature [33, 69].

Interestingly the PL slightly increases when annealing a high temperature annealed sample at 600 °C in N_2 gas, presented in figure 4.10. Although the change in intensity is small, and the measurement error is significant, a discussion is presented to identify possible causes for the change, since 600 °C is higher than the conditions commonly used in literature [11, 13, 33, 53, 131]. Since the sample is already annealed at 1000 °C for an hour, it is expected that there is no significant phase separation occurring at 600 °C anymore. Nor can the change be due to crystallization of a-Si, since that requires temperatures in excess of 900 °C [62]. Also no evidence for phase separation is seen in the FTIR measurements, figure 4.11, and no significant change in crystallinity is measured. This increase in PL could be due to removal of P_b centers by restructuring in the Si/SiO_2 interface region. For instance a strained Si-O bond ruptures, forming a NBOHC. This NBOHC then bonds with a P_b center, leaving behind a so called E'-center, which is a dangling bond of a silicon atom bonded to three oxygen atoms, illustrated in figure 4.13**(a)**. This is a well known non-radiative defect in SiO_2, however energies in excess of 5 eV are required to excite this defect [133, 134], which is significantly higher than the energy of the charge carriers excited in the NPs. Because of this high energy it is very unlikely that any recombination occurs at E'-centers. This could explain the increase in PL; as P_b centers are exchanged for E'-centers, 'active' non-radiative defects are exchanged for 'in-active' ones.

What also stands out is that the PL intensity mainly increases around 2 eV, visible in figure 4.10**(b)**, indicating increased radiative defect activity. This could also be explained by restructuring. For example: a strained Si-O bond breaks, and now the silicon part of the broken Si-O bond bonds with a P_b center, illustrated in figure 4.13**(b)**. This kind of restructuring is beneficial, since the binding energy of a Si-Si bond is 2.3 eV [135], while the binding energy of a Si-O bond is 4.7 eV [135],

leading to an excess energy of 2.4 eV. Of course many different combinations and restructuring mechanisms are possible.

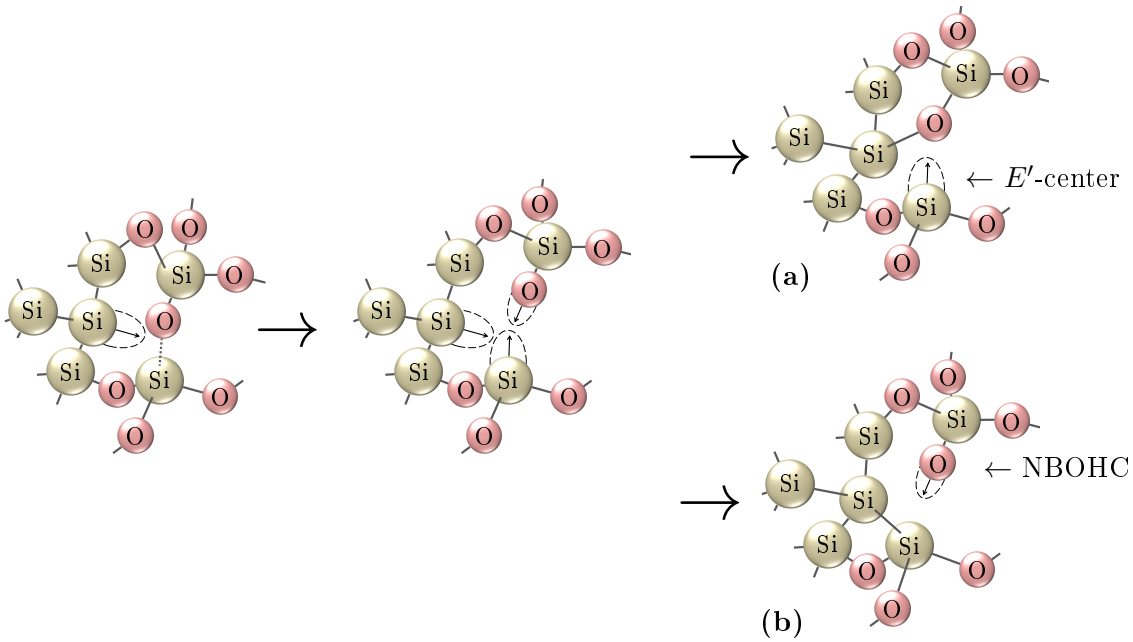

Figure 4.13: The removal of a P_b center by restructuring of the Si/SiO_2 interface, either resulting in an E'-center **(a)** or a NBOHC **(b)**. The arrows denote the unpaired spin and the dashed balloons represent their orbitals. The dotted line represents a strained Si-O bond.

The FTIR measurements, presented in figure 4.11, show a strong difference between as-deposited and TFA. As-deposited shows hydrogen related modes, peak (iv), indicating a high hydrogen concentration, which is a typical property of samples fabricated with PECVD [28, 71, 73]. After annealing these hydrogen related modes disappear, suggesting hydrogen effusion. Even after passivation these hydrogen modes are not visible, indicating that as-deposited contains a high concentration of hydrogen, which is not reached after passivation. After TF passivation at 600 °C there is no significant change in the FTIR spectrum, compared to after annealing, indicating no significant changes to the composition. This is supported by the insignificant changes in crystallinity.

Although a strong increase in PL is visible after passivation, no significant change in sub-bandgap absorption can be measured with PDS, figure 4.12. Between as-deposited and annealed a clear increase in overall absorption is visible, which can

be attributed to hydrogen effusion and c-Si NP formation [82]. After passivation it is expected that the P_b center density is decreased, resulting in a decrease in sub-bandgap absorption, however this was not observed. It is expected that the absorption coefficient above approximately 2 eV remains similar after passivation, since this range is related to band-to-band transitions in the amorphous matrix and the NPs. The difference in the high energy absorption can be attributed to the post-processing of the PDS data. The difference in sub-bandgap absorption is insignificant, indicating that PDS is less sensitive to changes in defect densities than PL.

4.2.2 Hydrogen Plasma Passivation

Experimental Details

Multilayer samples with a Si-rich layer composition of $SiO_{0.3}$ and buffer layer composition of $SiO_{1.3}$ are fabricated with PECVD. The thicknesses of these layers are 1.2 nm and 2.4 nm respectively. Hydrogen plasma passivation is performed at 30 °C, 90 °C and 205 °C, and at each temperature it is performed both with and without 347 $mWcm^{-1}$ plasma. Three different cooling strategies are applied after passivation with plasma at 205 °C; regular cooling in N_2 at 1.5 μbar, cooling in H_2 at 12.5 mbar, and cooling in H plasma at 12.5 mbar[1]. A high partial pressure of hydrogen in the cooling atmosphere is expected to reduce hydrogen effusion from the sample. And by applying plasma during cooling, passivation is expected to continue, while at the same time hydrogen effusion is suppressed. These three cooling strategies will be refered to as N_2, H_2 and H plasma respectively. The settings for the hydrogen passivation processes are presented in table 4.2.

Table 4.2: Passivation settings for hydrogen plasma passivation.

Process	Substrate temperature [°C]	Time [min]	Gas	Gas flow [sccm]	Plasma power [$mWcm^{-1}$]	Cooling strategy
PECVD	30	30	H_2	200	0	N_2
	90	30	H_2	200	0	N_2
	205	30	H_2	200	0	N_2
	30	30	H_2	200	347	N_2
	90	30	H_2	200	347	N_2
	205	30	H_2	200	347	N_2
	205	30	H_2	200	347	H_2
	205	30	H_2	200	347	H plasma

[1] 12.5 mbar is the highest operating pressure of the used PECVD setup.

Results

The PL spectra of the hydrogen plasma passivation series are presented in figure 4.14. An increase in PL is visible after passivation, except for passivation at 90 °C with plasma, see figure 4.14**(a)**. For all hydrogen plasma passivation processes the increase in PL intensity is much smaller than after TF or RTP passivation, see figure 4.6.

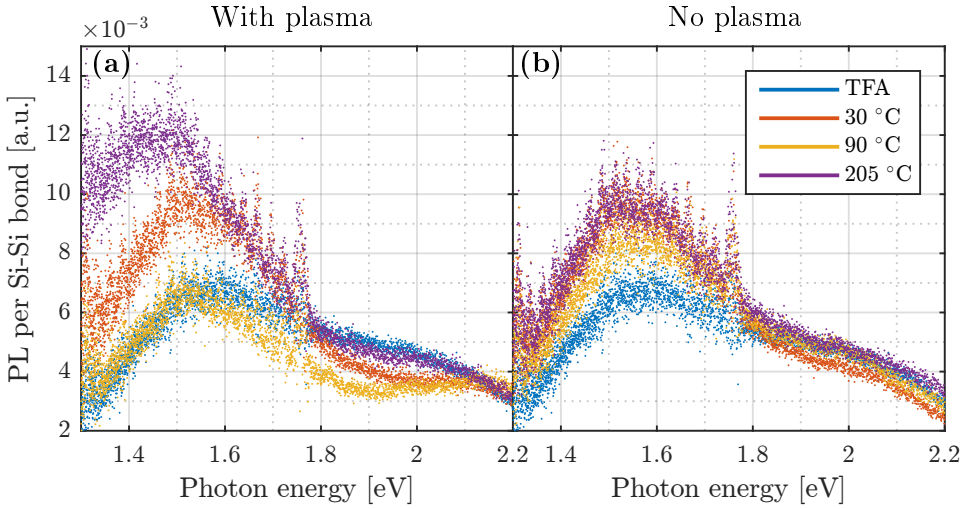

Figure 4.14: The PL spectra per Si-Si bond after TFA and each passivation temperature of the hydrogen plasma passivated series, indicated by the legend. Figures **(a)** and **(b)** represent with and without 347 mWcm^{-1} plasma, respectively. Only one third of all datapoints is shown for clarity.

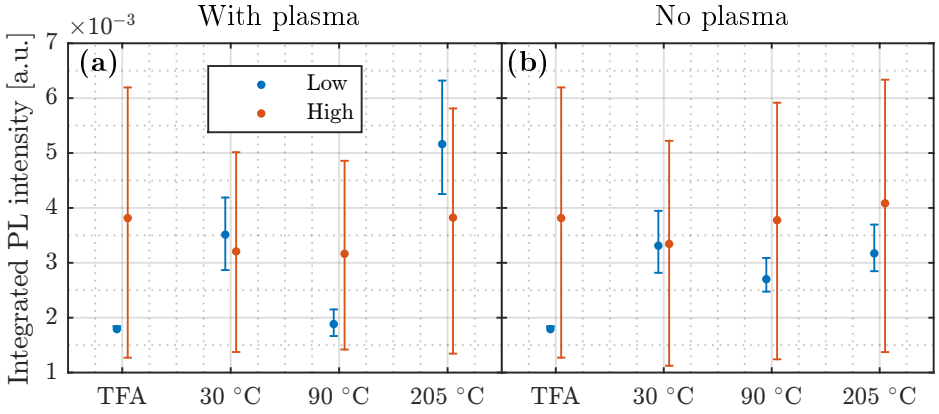

Figure 4.15: The integrated intensities of the low and high energy contributions after TFA and the different hydrogen plasma passivation processes, indicated by the x-axis. Figures **(a)** and **(b)** represent with and without 347 mWcm^{-1} plasma, respectively.

The integrated intensities of the low and high energy contributions are presented in figure 4.15. All observed changes to the high energy contribution are insignificant, compared to the measurement error. The low energy contribution increases after passivation, with the exception of the 90 °C process with plasma. Without plasma there is no significant dependence on temperature visible in the intensity of the low energy contribution after the initial increase.

The PL spectra and integrated intensity of the different cooling strategies are presented in figure 4.16. A decrease in the high energy contribution is visible, however the measurement error is significant. The low energy contribution remains similar for the different cooling strategies.

The peak position of the low energy contributions is presented in figure 4.17**(a)**, and again a decrease in peak position is visible, just as for TF and RTP passivation. The shift is largest for the processes with plasma. Without plasma the change is negligible compared to the measurement error, except for the highest temperature. The different cooling strategies result in an increase in peak position.

The total integrated PL intensities of all hydrogen plasma passivation processes are shown in figure 4.17**(b)**. All changes in integrated intensity are considered insignificant.

No FTIR spectra are presented since no significant change is visible. The crystallinity after annealing is 0.34 ± 0.005, and again did not change significantly after subsequent passivation.

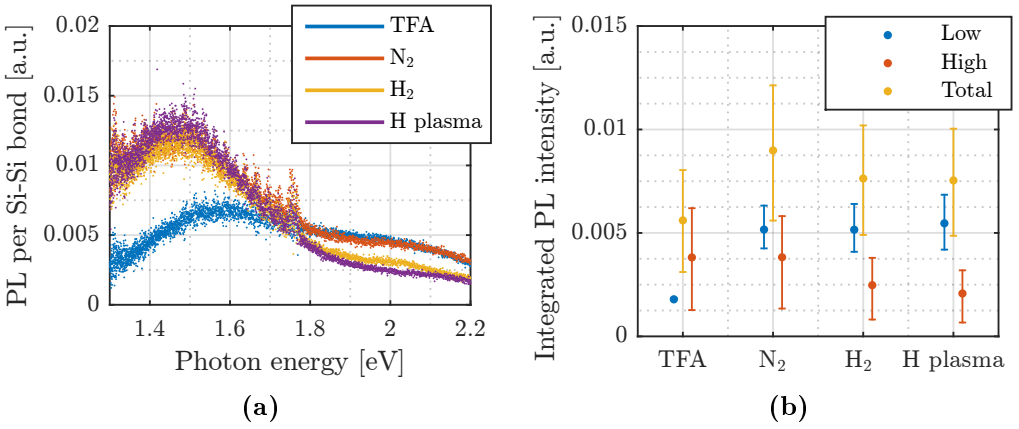

Figure 4.16: The PL spectra per Si-Si bond **(a)** and the integrated intensities **(b)** of the different cooling methods. In figure **(a)** only one third of all datapoints is shown for clarity.

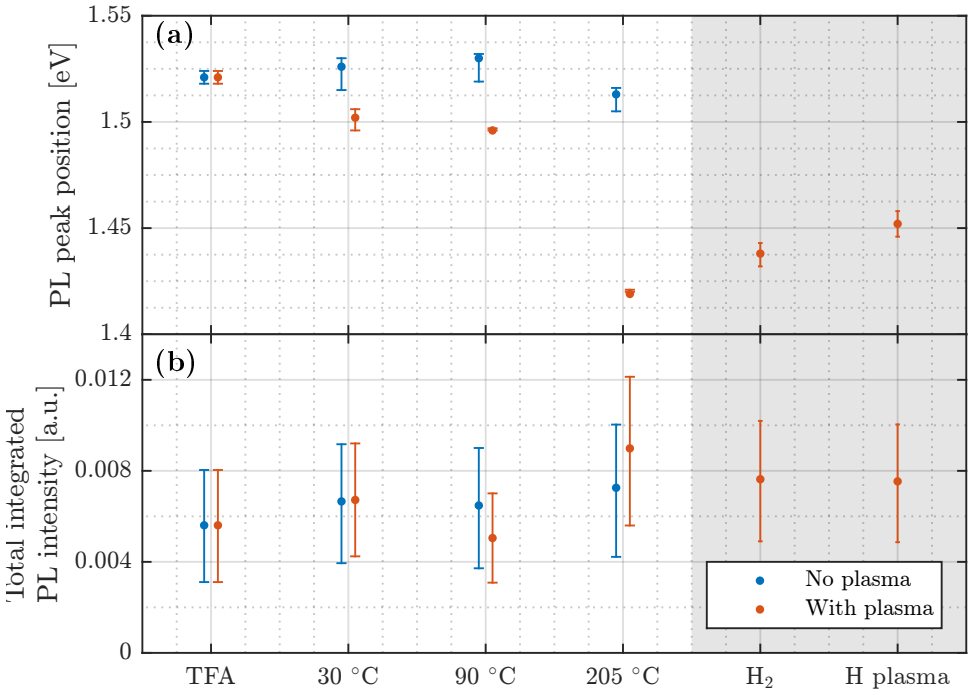

Figure 4.17: The peak position of the low energy contribution **(a)**, and the total integrated PL intensity **(b)** of the different plasma passivation processes. The error bars show the standard deviation. The x-scale indicates the processing; TFA, the temperatures of the passivation processes. In the shaded area the integrated intensity of the hydrogen atmosphere cooled and hydrogen plasma cooled samples is also shown, indicated by H_2 and H plasma on the x-axis. The horizontal offset is for clarity.

Discussion

The low energy contribution increased, even after passivation without plasma at 30 °C. This is interesting because of the low temperature, and the low pressure. Together with the fact that RTP passivation showed no significant increase in the low energy contribution after passivation at 200 °C, see figure 4.7, it is likely that the scaling of the PL spectrum of the TFA sample is faulty. Because of the unexpected behaviour of the intensity of the sample passivated with plasma at 90 °C, it is likely that the scaling of this spectrum is faulty.

After passivation at 205 °C with plasma, a slight increase in the low energy contribution is visible, compared to without plasma. Since no significant change in the intensity was visible after RTP passivation at 200 °C, this could be an indication of the effect of plasma, which could lead to passivation at lower temperatures.

Even though the scaling of some of the spectra might be wrong, the peak position of the low energy contribution is still relevant, visible in figure 4.17. Without plasma the peak position remains similar, suggesting no changes in the photoluminescent NP distribution. The slight decrease in peak position after passivation with plasma at low temperatures, and the strong drop at 205 °C, indicates that plasma passivation requires temperatures in excess of 90 °C, and the clear difference between with and without plasma shows the beneficial effect of plasma.

The increase in peak position after cooling in H_2 gas, or in H plasma, suggests that relatively more small NPs contribute. This could indicate that hydrogen binds stronger to large NPs than to small NPs. When cooled in a N_2 atmosphere, hydrogen is released quicker from small NPs, resulting in a lower peak position. When cooled in a hydrogen atmosphere, hydrogen effusion is reduced, and hydrogen release from small NPs is reduced. This is however not reported in literature.

4.3 Excess Silicon Content

Clustered NPs are expected to have a low PL intensity because of their larger size, which leads to reduced confinement [25, 26, 32, 120, 121], and higher chances on surface defects [122]. A way to reduce clustering is reducing the excess silicon content of the Si-rich layer. By reducing the excess silicon content, the NP density is reduced, leading to larger NP spacing. This both has a positive and negative effect; clustering is reduced, but both the tunneling probability and conduction through large Si clusteres is reduced, obstructing charge transport. Based on calculations by Green *et al.*, NP spacing up to 2 nm provides an acceptable mobility of $10^{-1}\,\mathrm{cm^2V^{-1}}$ [45]. To establish an ideal excess silicon content, a model derived by Tournus [124] and expanded by van Sebille *et al.* [123] is used to determine the distribution of NPs inside a Si-rich layer of 3 nm. This model assumes that all NPs are the same size; the thickness of the Si-rich layer.

The model provides a probability density function for the 2D center-to-center distance of NPs in a monolayer, which will be used to model the NP spacing inside a single Si-rich layer inside a multilayer stack. Since the PL measurements are scaled to the amount of Si-Si bonds, which effectively is a measure of the NP density, it is convenient to express the distribution of NPs as a fraction of the total. The fraction of clustered NPs is identified by integrating the probability density function from 0 to two times the radius of a NP, which is 3 nm. The fraction of NPs contributing to charge transport by tunneling is calculated by integrating from 3 nm to 5 nm, which means integrating from touching NPs up to a spacing of 2 nm. The photoluminescent NP fraction is obtained by integrating from 3 nm to infinity, or 1 minus the clustered NP fraction. The result of this calculation as a function of $\frac{[O]}{[Si]}$ fraction is presented in figure 4.18.

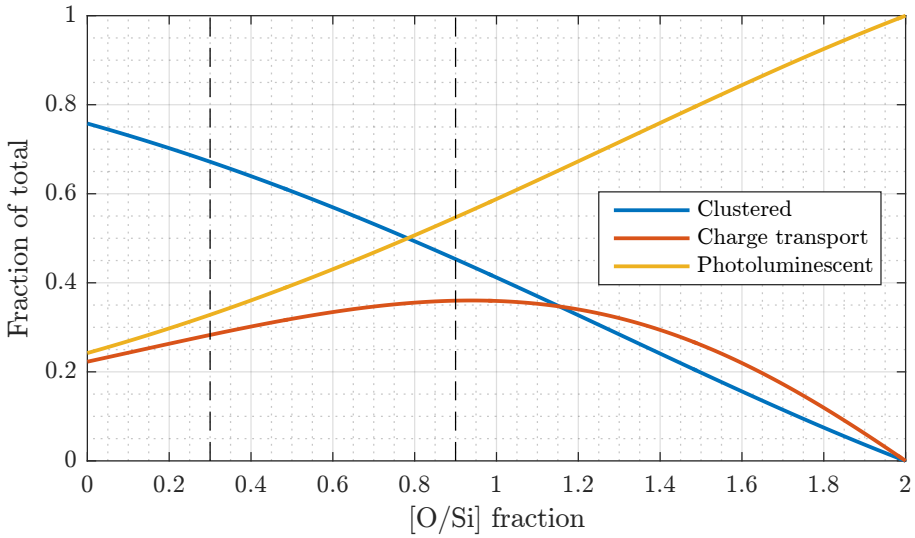

Figure 4.18: The distribution of NPs among the three groups as a function of $\frac{[O]}{[Si]}$ fraction. This is calculated for a crystallinity of 0.3, and a Si-rich layer thickness of 3 nm. The vertical dashed lines represent a $\frac{[O]}{[Si]}$ fraction of 0.3 and 0.9 respectively.

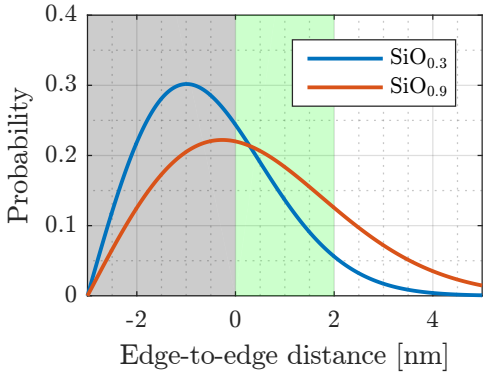

Figure 4.19: The edge-to-edge distance probability density function for NPs with a diameter of 3 nm in a Si-rich layer with a crystallinity of 0.3 for two compositions. The grey shaded area indicates clustered NPs, and the green shaded area indicates NPs properly spaced for charge transport based on tunneling.

A clear decrease in clustered NPs is visible with increasing $\frac{[O]}{[Si]}$ fraction, i.e. decreasing excess silicon content. A maximum is visible in the charge transport fraction, which can be explained by the probability density functions, presented in figure 4.19. By decreasing the excess silicon content, the distribution stretches

towards larger NP spacing. At low $\frac{[O]}{[Si]}$ fraction, clustering dominates, and at high $\frac{[O]}{[Si]}$ fraction the NPs are too far apart for efficient tunneling.

The analysis presented in this report is mainly based on PL, however the ultimate goal is to increase the performance of solar cells based on embedded NPs. Therefore charge transport based on tunneling is considered to be the determining factor for finding the optimal composition. The optimal composition for charge transport as a function of crystallinity in a Si-rich layer with a thickness of 3 nm is presented in figure 4.20. For a higher $\frac{[O]}{[Si]}$ fraction, a higher crystallinity is necessary. The green shaded area is an indication of the achievable crystallinity with the used annealing conditions, based on the datapoints. This shows that a composition around $SiO_{0.9}$ will yield the best results with the used conditions, and the $SiO_{0.3}$ composition will have a large clustered NP fraction.

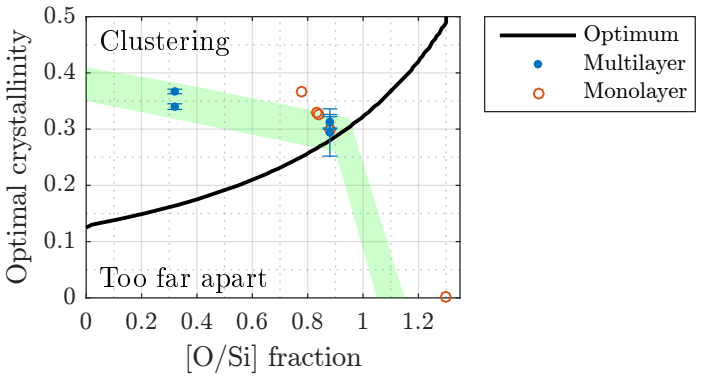

Figure 4.20: The optimal crystallinity as function of $\frac{[O]}{[Si]}$ fraction for a Si-rich layer of 3 nm thick. Above this optimum, clustering of NPs dominates, and below this optimum NPs are too far apart for efficient charge transport. The green shaded area represents crystallinity values achievable with the used annealing conditions.

Experimental Details

In this experiment two multilayer samples are fabricated, each with a different Si-rich layer composition: $SiO_{0.3}$ and $SiO_{0.9}$. The Si-rich and buffer layer thicknesses of the $SiO_{0.3}$ sample are 1.2 nm and 2.4 nm respectively. The Si-rich and buffer layer thicknesses of the $SiO_{0.9}$ sample are 3 nm and 1 nm respectively. Both compositions are annealed, and also passivated with TF passivation. The settings of these passivation processes are presented in table 4.1.

Results

The PL spectra of the different compositions are presented in figure 4.21. A clear increase in PL is visible with decreasing excess Si content, as expected. This is also

clearly visualized in figure 4.22, which shows the integrated intensities of the low and high energy contributions. A strong increase in the low energy contribution is visible in figure 4.22**(b)** after passivation at 400 °C, and an even further increase is visible at 600 °C, which is similar to what is seen in the RTP passivated series, see figure 4.7.

Figure 4.23**(a)** shows the peak position of the low energy contribution, and a clear decrease in peak position is visible. Again a step is visible between 200 °C and 400 °C. The peak also shifts to lower energy for $SiO_{0.9}$, compared to $SiO_{0.3}$.

The total integrated intensity is presented in figure 4.23**(b)**. For $SiO_{0.9}$ the integrated intensity is already higher after annealing, and increases further with increasing passivation temperature compared to $SiO_{0.3}$. What stands out is that at a passivation temperature of 200 °C the integrated intensity of both compositions is almost the same, which is due to the wrong scaling of the $SiO_{0.3}$ sample passivated at 200 °C, which is the same sample as in section 4.2.1.

The light and dark conductivity of $SiO_{0.3}$ is shown in figure 4.24. Because of the low conductivity of the $SiO_{0.9}$ composition, no data was obtained. The conductivity of $SiO_{0.3}$ first decreases after passivation at 200 °C, but afterwards increases with increasing passivation temperature. All $SiO_{0.3}$ samples show an increase in conductivity when illuminated. The difference between dark and light conductivity is larger after passivation.

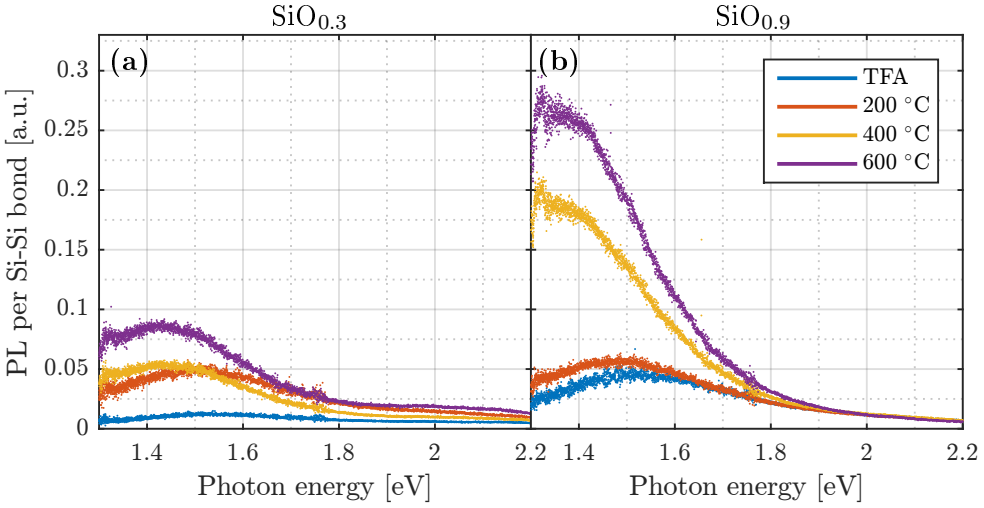

Figure 4.21: The PL spectra per Si-Si bond after TFA and for each TF passivation temperature for the different Si-rich layer compositions. Figures **(a)** and **(b)** represent $SiO_{0.3}$ and $SiO_{0.9}$, respectively. Only one third of all datapoints is shown for clarity.

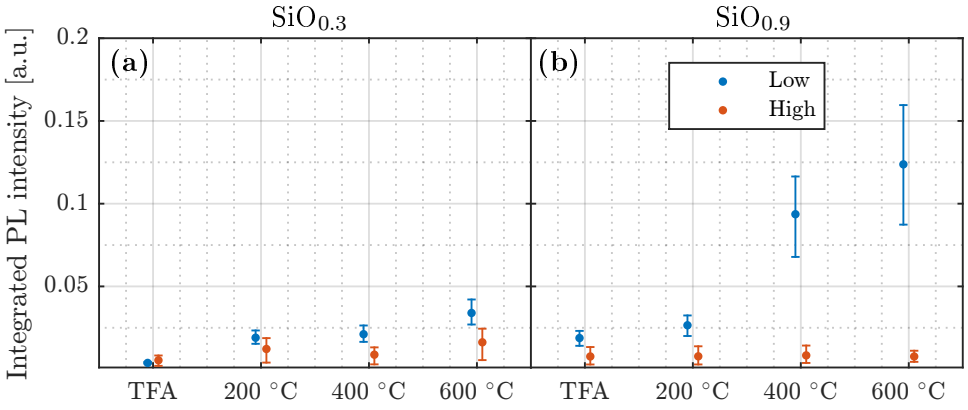

Figure 4.22: The integrated intensities of the low and high energy contributions after TFA and for each passivation temperature for the different Si-rich layer compositions. Figures **(a)** and **(b)** represent $SiO_{0.3}$ and $SiO_{0.9}$, respectively.

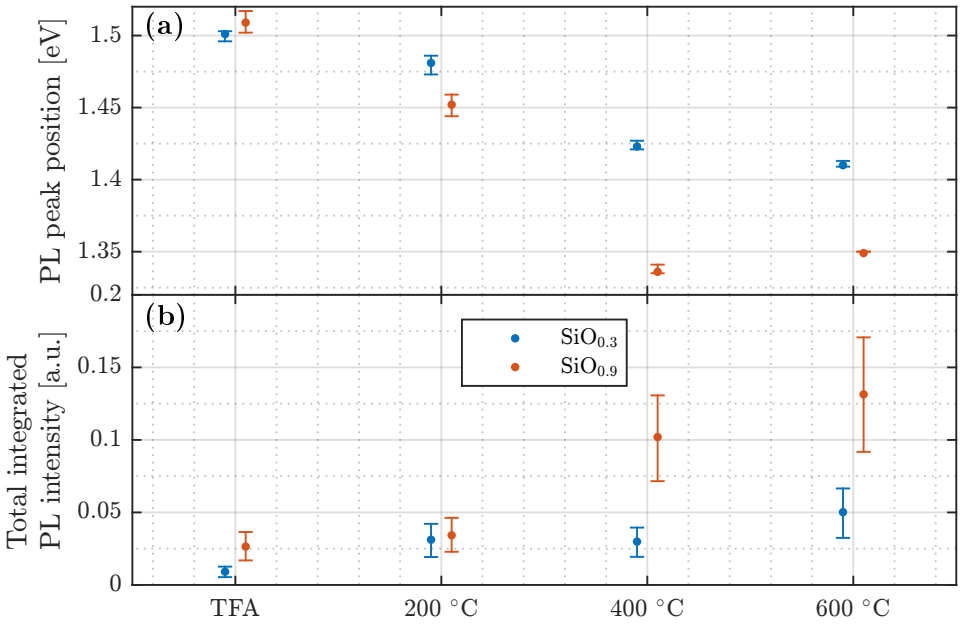

Figure 4.23: The peak position of the low energy contribution **(a)**, and the total integrated PL intensity **(b)** of the two compositions. The error bars show the standard deviation. The x-scale indicates the processing; TFA and the temperatures of the TF passivation processes. The horizontal offset is for clarity.

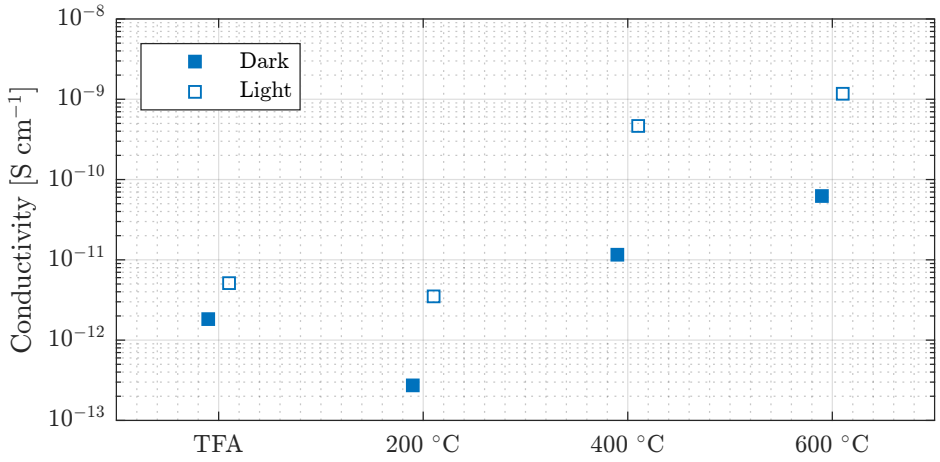

Figure 4.24: The conductivity of a multilayer sample with a Si-rich layer composition of $SiO_{0.3}$ after TFA and for the different TF passivation temperatures, indicated by the x-axis. The horizontal offset is for clarity.

The composition of the as-deposited layers are known, however the composition after annealing is unknown. To identify differences in the final composition, FTIR measurements are performed, shown in figure 4.25. Apart from a small increase in absorption at 1080 cm^{-1}, the Si-O-Si asymmetric stretching TO mode [62, 108–114], the spectra are similar. The crystallinity after annealing of the $SiO_{0.3}$ layer is 0.37 ± 0.004, and for the $SiO_{0.9}$ layer it is 0.29 ± 0.04. This clearly decreased, and the variation increased. After passivation there is no significant change in crystallinity.

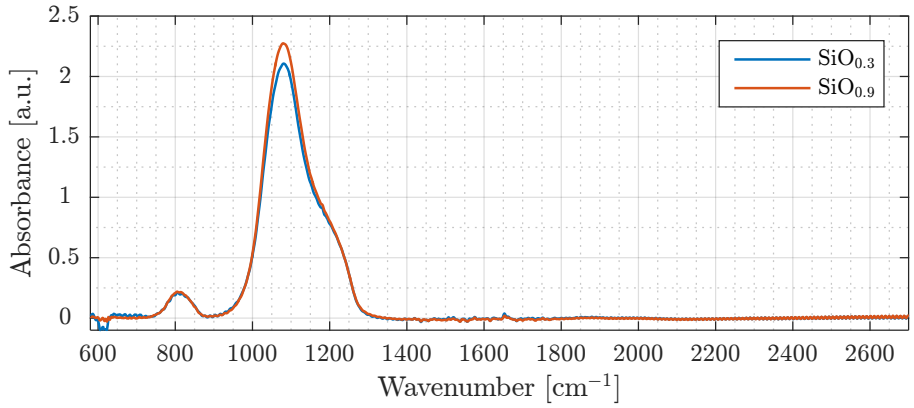

Figure 4.25: The FTIR absorption spectrum of the two multilayer samples with different Si-rich layer compositions after annealing. The composition of the Si-rich layer is presented in the legend.

Discussion

By increasing the amount of excess silicon, a decrease in PL intensity is seen, which has also been reported in literature [27, 136]. This can be explained by the effect of clustering of NPs, which leads to reduced confinement [25, 26, 32, 120, 121], and higher chances on surface defects [122]. By decreasing the excess silicon content, the clustered NP fraction is reduced, and the PL intensity is increased. This is in accordance with the theoretical model by van Sebille *et al.*, presented in figure 4.18.

The fact that mainly the intensity of the low energy contribution increases, indicates that PL due to recombination at NPs increases. The high energy contribution remains similar with different excess silicon contents, suggesting little change in the surrounding matrix. And passivation does not significantly alter the intensity of the high energy contribution, indicating passivation of P_b centers does not influence PL of defects emitting at 2 eV. This is also supported by the fact that charge carriers recombining in these defects must either be excited within these defects, or be excited in NPs with a bandgap larger than 2 eV. Charge carriers can be excited in photoluminescent defects, for instance NBOHCs have an asymmetric absorption band around 1.97 eV with a tail towards higher energies [36, 87]. If the charge carriers are not excited inside the defects, they must come from very small NPs with a bandgap larger than 2 eV. These small NPs are expected to have a low chance on surface defects, hence passivation has a negligible effect on these NPs.

The shift in peak position of the low energy contribution again follows QC, see figure 4.23**(a)**. The higher chance of surface defects for large NPs results in an increase in their contribution after passivation, leading to a shift to lower energies. The difference in peak position for the two compositions can be explained by the difference in Si-rich layer thickness. The fact that the Si-rich layer is thinner in the $SiO_{0.3}$ sample results in a higher peak position; the thinner layer results in smaller NPs which have a higher bandgap.

Interestingly the peak position after annealing is similar, although the Si-rich layer composition and thickness is different. This suggests that after annealing PL due to QC is dominated by other PL mechanisms, which is likely ISR. After passivation the peak shift indicates that PL of QC increases, leading to differences in peak position.

The large shift between passivation at 200 °C and 400 °C is visible in both compositions, which again is an indication that 200 °C is not enough for efficient passivation. Remarkably the peak shifts to higher energy between passivation at 400 °C and 600 °C in the $SiO_{0.9}$ composition, which is in conflict with QC. Because of this highly unexpected behaviour, and the small difference, the difference is ascribed to variations in the sample.

Decreased clustering is also supported by the conductivity measurements. Since $SiO_{0.3}$ shows lower PL intensity, NP clusters are expected. These clusters have reasonable conductivity, since charge transport does not have to rely on tunneling. When defects are passivated, the conductivity increases due to lower recombination

rates, and an increase is visible to some extent, see figure 4.24. Conductivity is expected to increase when the samples are illuminated because of higher charge carrier concentrations, which is also visible. Because of the difficulties encountered with measuring the conductivity of the $SiO_{0.9}$ sample, it is assumed that the conductivity is lower, as is expected from the larger NP spacing and reduced clustering fraction.

The FTIR spectra show only a minor change in absorption around $1080\,cm^{-1}$, indicating that the surrounding matrix is slightly more stoichiometric in $SiO_{0.9}$. This could be due to the fact that the initial composition of the layer was more stoichiometric. Because of the small difference in the FTIR spectra, and higher crystallinity, it can be assumed that $SiO_{0.3}$ contains a higher NP density, which leads to more clustering, supported by the other results. The decrease in crystallinity between $SiO_{0.3}$ and $SiO_{0.9}$ can be explained by the decreasing excess silicon content. This leads to smaller a-Si clusters, of which a larger fraction does not reach the critical crystallization radius. The increase in variation in crystallinity is ascribed to the same effect.

4.4 Si-rich Layer Thickness

As discussed in section 3.2.1, the maximum NP size in a multilayer structure is limited by the Si-rich layer thickness. Thus by varying the Si-rich layer thickness the size distribution of the NPs can be changed. The NP size influences the bandgap of the material, and thereby the PL spectrum.

Experimental Details

For this experiment three multilayer samples are fabricated, with different Si-rich layer thicknesses; 2, 3 and 4 nm. The composition of the Si-rich layer is $SiO_{0.9}$. The samples are annealed at 700 °C, 900 °C and 1000 °C for 1 hour in N_2 gas. These temperatures are chosen because of the phase separation and crystallization inside the Si-rich layer. Phase separation starts around 600 °C [62] to 650 °C [8], thus at 700 °C small a-Si NPs are expected. Crystallization of a-Si starts between 900 °C [62] to 1000 °C [8], hence the maximum number of a-Si NPs are expected at 900 °C. At the maximum temperature, 1000 °C, some of the a-Si NPs become c-Si, and the highest crystallization is reached. To see the effect of passivation, all samples are also passivated at 600 °C in the TF after annealing.

Results

The resulting PL spectra are shown in figure 4.26. The left and right column of figures represent before and after TF passivation, and it is clear that the PL intensity of all samples increases after TF passivation, as expected from earlier results. What stands out is that after annealing at 700 °C, the PL intensity is higher than when annealed at higher temperatures. This is also visible in the total integrated intensity,

figure 4.27**(d) (e) (f)**, where the increase in PL intensity after passivation is also visible.

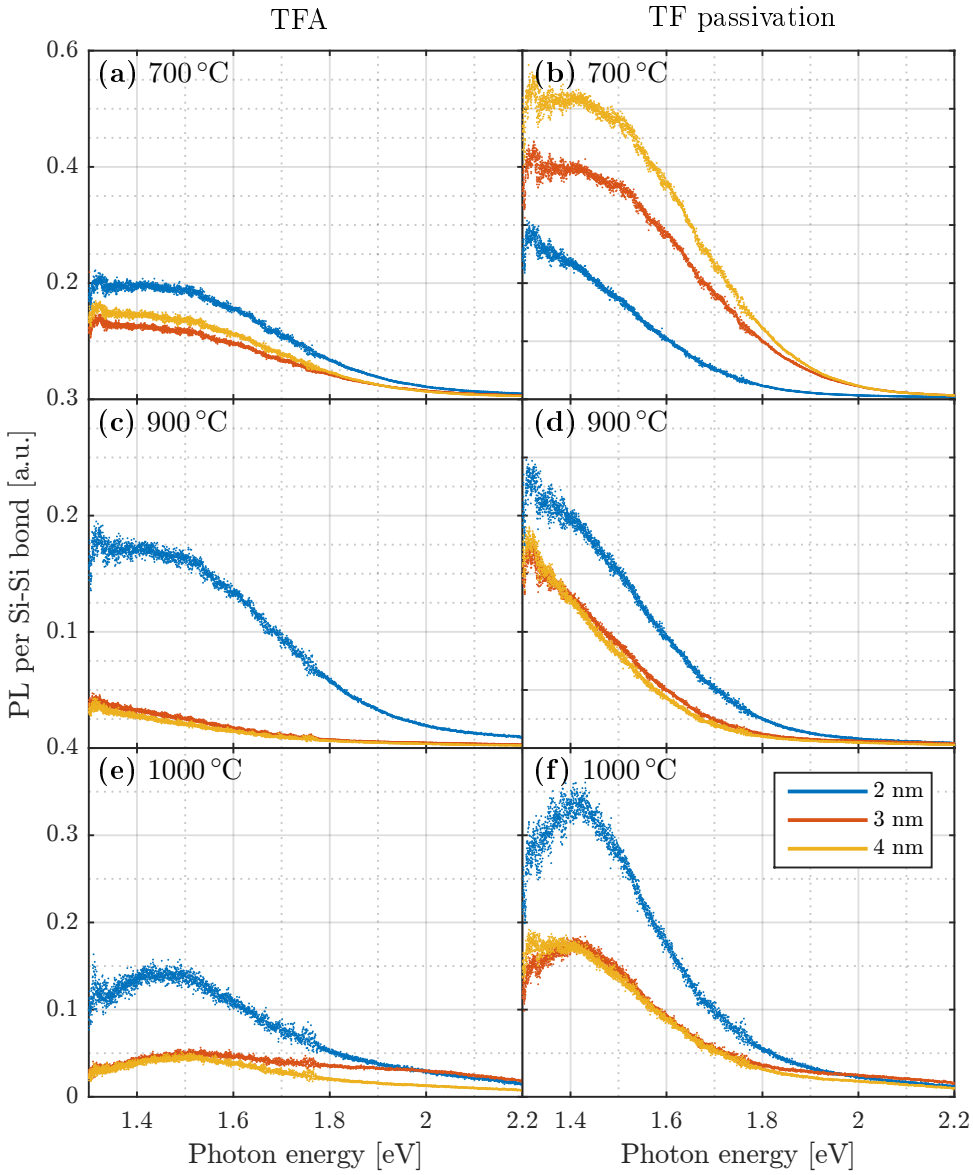

Figure 4.26: The PL spectra per Si-Si bond after TFA and subsequent TF passivation with varying Si-rich layer thickness and varying annealing temperature. The annealing temperature is indicated in the respective figure. The left and right column represent before and after TF passivation at 600 °C, respectively. Only one third of all datapoints is shown for clarity.

A difference in peak position is already visible in figure 4.26. Therefore the peak position of the low energy contribution is plotted in figure 4.27 **(a) (b) (c)**. Between 700 °C to 900 °C, a decrease in peak position of the low energy contribution is visible, except for the 2 nm thick Si-rich layer. At 900 °C the peak has reached the limits of the fitting function, which is why the position remains at 1.3 eV. It is likely that the actual peak is below 1.3 eV when looking at their spectra, see figure 4.26**(d)**. Between 900 °C to 1000 °C, an increase in peak position is present. At 1000 °C the peak position increases with layer thickness before passivaiton, and decreases after passivation.

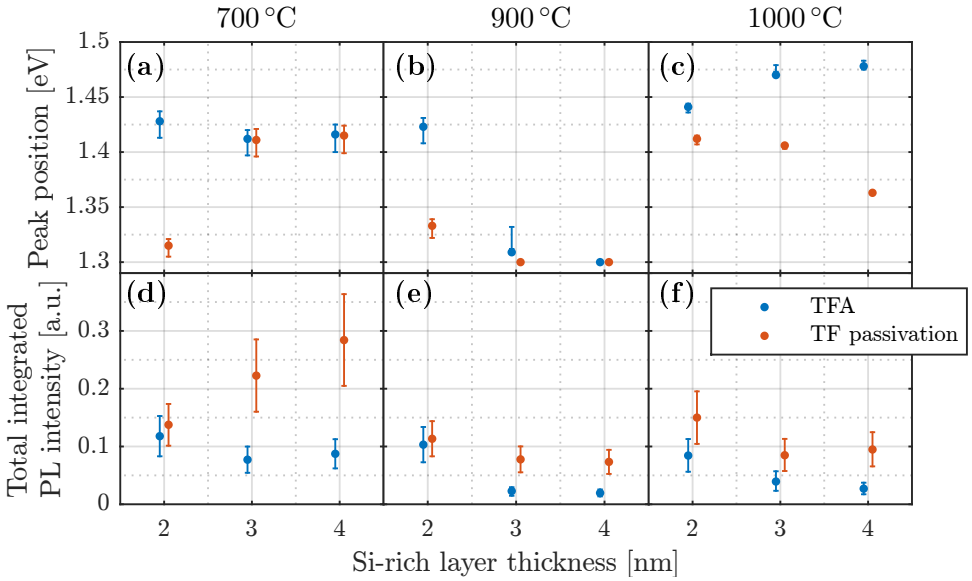

Figure 4.27: The peak position of the low energy contribution and the total integrated PL intensity for the three different Si-rich layer thicknesses and different annealing temperatures. The annealing temperature is written above the figures. The error bars show the standard deviation. The horizontal offset is for clarity.

The integrated intensity of the low and high energy contributions are presented in figure 4.28. Interestingly, a higher annealing temperature results in a lower intensity of the low energy contribution. What also stands out is that the 2 nm thick Si-rich layer shows the highest intensity of the low energy contribution, except after passivation of the 700 °C annealed sample. The intensity of the high energy contribution is always similar or lower than the low energy contribution, which is comparable to the previously presented results.

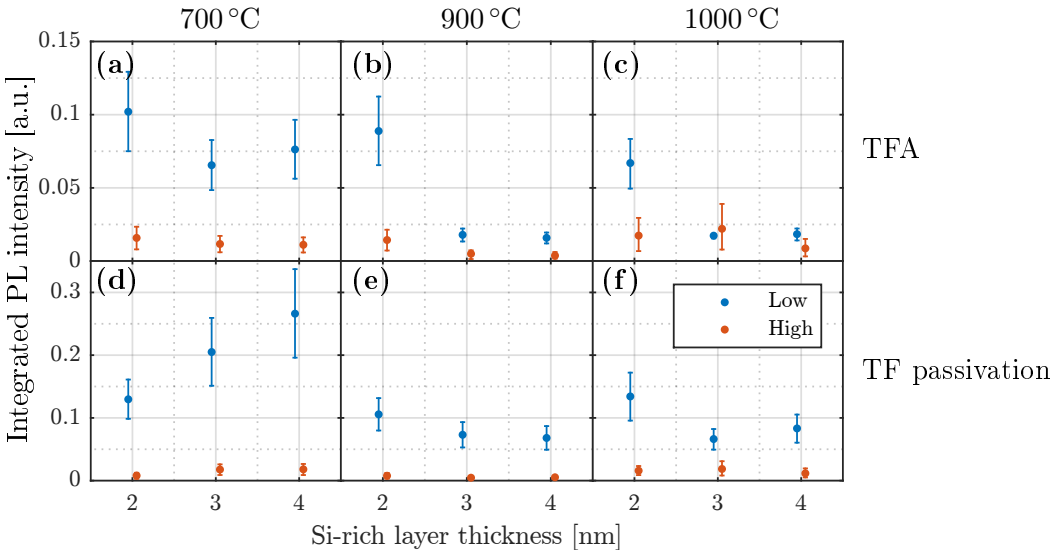

Figure 4.28: The integrated intensity of the low and high energy contribution for the three different Si-rich layer thicknesses and different annealing temperatures. The top and bottom row indicate before and after TF passivation. The annealing temperature is written above the figures. The error bars show the standard deviation.

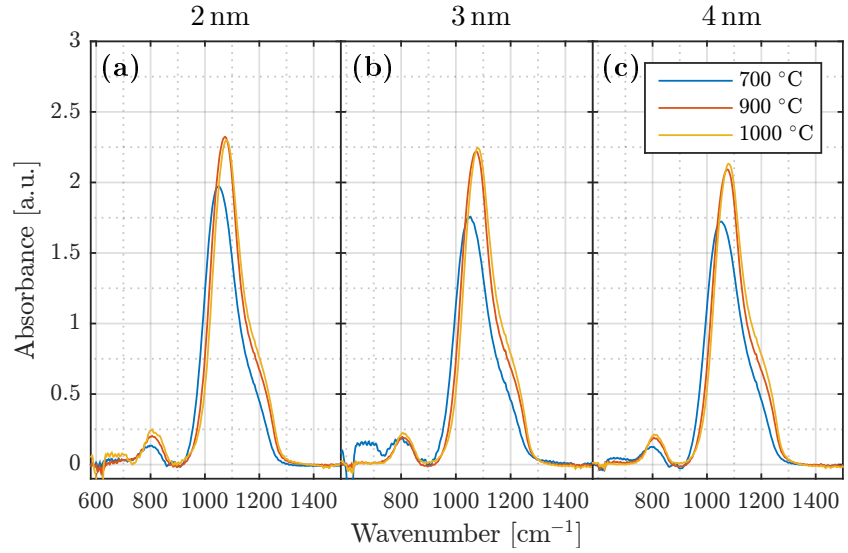

Figure 4.29: The FTIR absorption spectra of the three different Si-rich layer thicknesses for different annealing temperatures, indicated by the legend. Figures **(a)**, **(b)** and **(c)** represent 2, 3 and 4 nm respectively, indicated above the figures.

The FTIR measurements are presented in figure 4.29. All Si-rich layer thicknesses show an increase in absorption between 700 °C and 900 °C, and between 900 °C and 1000 °C the absorption remains similar. The spectra consist out of three peaks; Si-O-Si bending at 810 cm^{-1} [109–113], Si-O-Si asymmetric stretching TO 1080 cm^{-1} [62, 108–114], and the Si-O-Si asymmetric stretching LO at 1200 cm^{-1} [108], similar to the spectra visible in figure 4.11 and figure 4.25. The FTIR spectra after passivation are not presented, since the change is insignificant compared to after annealing, comparable to figure 4.11. At 1000 °C c-Si is present in the Raman phonon modes, and the crystallinity of the 2, 3 and 4 nm layer are 0.19 ± 0.04, 0.31 ± 0.01 and 0.31 ± 0.01 respectively.

Discussion

At 700 °C, the 2 nm thick layer shows a strong decrease in peak position after passivation. This shift indicates passivation of P_b centers, and an increase in contribution of large NPs. These NPs are however amorphous, and PL of a-Si NPs around 1.3 eV has not yet been reported based on the performed literature study presented in section 1.2.5. 1.3 eV is very close to the bulk bandgap of a-Si [126], which indicates that the NPs are probably clustered, and form large a-Si patches inside the Si-rich layer. These a-Si patches are weakly confined compared to NPs, and are expected to have a low PL intensity [25, 26, 32, 120, 121]. The fact that there is negligible change in intensity of the low energy contribution, see figure 4.28**(a)** and **(d)**, supports this concept.

The 3 nm and 4 nm layers show a negligible difference in peak position with respect to the 2 nm layer before passivation, and after passivation the peak position hardly changes. The comparable peak position before passivation suggests that the NP size distribution is comparable. The fact that passivation hardly influences the peak position in the 3 nm and 4 nm thick layer, indicates that there is negligible clustering present in these layers. The increase in intensity after passivation is thus ascribed to passivation of P_b centers of isolated NPs. The intensity of the low energy contribution, which is similar before passivation for all layers, and increases with increasing layer thickness after passivation, is an indication that clustering decreases for thicker layers. The clustered NP density is expected to increase with decreasing layer thickness, which is also predicted by the model by van Sebille *et al.* [123], see figure 4.30. Although this model is based on c-Si NPs, the behaviour also applies to a-Si NPs.

The total integrated intensity, presented in figure 4.27**(d)** **(e)** and **(f)**, shows a decrease in intensity between 700 °C and 900 °C, which is in accordance with several reports [25, 26, 32, 120, 121]. The explanation presented in these reports is based on phase separation; higher temperatures lead to increased phase separation and the formation of more and larger a-Si NPs. The PL decreases when these NPs become too large due to decreased QC. This concept is also supported by the shift in peak position; at 900 °C the peak shifts to lower energy. Increased phase separation is

also visible in the FTIR spectra, which show a clear increase in absorption between 700 °C and 900 °C, indicating a higher $\frac{O}{Si}$ fraction in the surrounding matrix.

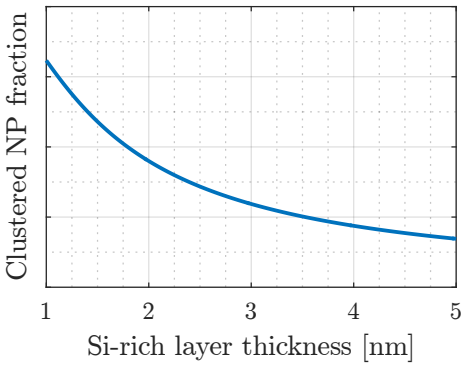

Figure 4.30: The clustered NP fraction in a single Si-rich layer, as a function of Si-rich layer thickness for an arbitrary crystallinity. The y-scale is left blank since only the behaviour is of interest.

At 900 °C the peak position decreases with increasing layer thickness, which can be explained by reduced QC because of the larger thickness. The low peak position indicates the presence of large a-Si patches inside the Si-rich layer, which is also supported by the integrated intensity of the low energy contribution. This intensity decreases with increasing layer thickness, which is in accordance with a reduction of QC.

Between 900 °C and 1000 °C the integrated intensity remains similar. Typically an increase in PL intensity, and a shift to lower energies is seen between these temperatures which is ascribed to the formation of c-Si NPs [32, 34]. In the results presented in this report, none of these effects is visible, see figure 4.27**(b) (c)**. If QC is the main PL mechanism, a possible explanation would be increased confinement by separation of clustered NPs occuring during the crystallization process. TEM images of embedded NPs revealed mainly spherical or near-spherical c-Si NPs [4, 55, 137]. Crystallization of a-Si layers also revealed initially spherical c-Si NPs with diameters smaller than the thickness of the layer [138]. If the a-Si clusters have an arbitrary shape, this could lead to separation of NPs, illustrated by figure 4.31. This separation would result in an increase in QC of both the a-Si and c-Si NPs, resulting in an increase in peak position. This behaviour has not been reported in literature however. If QC is not the main PL mechanism, ISR would be the best option. The mechanism behind ISR is still unknown, therefore no explanation for the increase in peak position can be given.

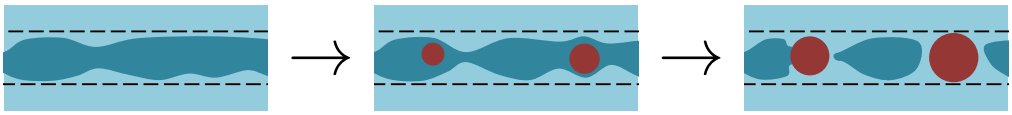

Figure 4.31: Separation of NPs due to the spherical shape of c-Si NPs. The black dotted lines represent the edges of the Si-rich layer. The dark blue and dark red represent a-Si and c-Si respectively.

A clear difference between the peak positions for the different layer thicknesses is visible at 1000 °C, see figure 4.27(**c**). After annealing the peak position increases with increasing layer thickness, which is contradictory to what is to be expected from the maximum NP size and QC [6–13, 46, 51, 76]. A possible explanation would be the higher clustered fraction, present in the thinner layers, which could lead to a lower bandgap. This would however also require a lower integrated intensity of the low energy contribution with decreasing Si-rich layer thickness, which is opposite to the results. It is more likely that after 1000 °C PL is dominated by ISR instead of QC. Interestingly the trend in peak position is inverted after passivation, and then indeed follows QC, and corresponds to literature [6, 7, 46, 51]. The PL intensity increases after passivation, which also follows QC. The 2 nm layer shows again the highest intensity, which is ascribed to stronger confinement in this thin layer. Since after passivation most features can be explained with QC, it is likely that passivation is necessary to increase the contribution of QC in the PL spectra.

The FTIR spectra show what is expected, the absorption peaks increase between 700 °C and 900 °C, and remain similar between 900 °C and 1000 °C. This indicates that phase separation occurs between 700 °C and 900 °C, and is mostly finished around 900 °C, which explains the negligible difference between the 900 °C and 1000 °C spectra. Between 900 °C and 1000 °C, crystallization of the a-Si NPs occurs, leading to a crystallinity around 0.3. Except for the thinnest layer, 2 nm, which shows a significantly lower crystallinity. This can be ascribed to the thickness of the layer, which is rather close to the critical crystallization diameter of 1.14 nm [64, 65], therefore obstructing crystallization.

The changes in the integrated intensity of the high energy contribution are insignificant, which indicate it is independent of Si-rich layer thickness and annealing temperature. The fact that in the preceding results there was also no significant change present, makes it highly unlikely that this contribution is due to matrix defects. Especially since phase separation is clearly visible in the FTIR spectra between annealing at 700 °C and 900 °C, indicating changes in the surrounding matrix. It is possible that the spectra consist of two low energy contributions, of which one causes the PL around 2 eV. A combination of QC and ISR could be the case, however this was not used because of the chance of overfitting the data.

Conclusions & Recommendations

5

The results and discussion presented in previously are summarized and concluded in this chapter. The conclusions of each experiment are concluded separately, and at the end of the conclusions a short section is devoted to the interpretation of the photoluminescence spectra. Recommendations for future research are presented at the end of this chapter, which are divided into material properties and scaled photoluminescence measurements.

5.1 Validation

5.1.1 Excitation Wavelength

In the used Raman setup, a lower excitation wavelength has proven to be beneficial for the PL scaling method, presented in this report. This leads to reduced signal from the substrate, and an increase in measurement range.

5.1.2 Misalignment Angle

The scaling method is independent of misalignment angle, up to an angle of at least $7° \pm 2°$. At larger angles the signal-to-noise ratio decreases rapidly, which is attributed to the fact that the backscattered light needs to enter the lens in order to reach the detector.

5.2 Passivation of Dangling Bonds

5.2.1 Tube Furnace & Rapid Thermal Process Passivation

The higher PL intensity after TF passivation, compared to RTP passivation, indicates that longer processing results in better passivation of P_b centers. The optimal temperature is not established, but a clear indication for a decrease in P_b center densities with increasing passivation temperature up to 600 °C is reported. Temperatures in excess of 200 °C are believed to be necessary for efficient passivation. Photoluminescent defects emitting around 2 eV are not influenced by passivation, which suggest charge carriers are excited inside these defects.

5.2.2 Hydrogen Plasma Passivation

Hydrogen plasma passivation showed little change in PL intensity, compared to TF or RTP passivation. For hydrogen plasma passivation, temperatures in excess of 90 °C

are required. The results show a small beneficial effect of using plasma, opposed to using normal H_2 gas. Cooling at a low pressure in N_2 gas resulted in the lowest P_b center density, as opposed to cooling at a higher pressure in H_2 gas or H plasma.

5.3 Excess Silicon Content

The optimal composition of the Si-rich layer has not been established, however strong evidence is presented which favors a lower excess silicon content. This leads to a lower clustered NP fraction, without drastically changing the surrounding silicon oxide matrix, which is supported by results found in literature [27, 136], and a theoretical model [123]. The contribution of photoluminescent defects emitting around 2 eV is also independent of the initial composition.

5.4 Si-rich layer thickness

At 700 °C a-Si NPs are present. These a-Si NPs are likely to be clustered in the 2 nm thick Si-rich layers. In thicker layers no evidence is visible for clustering. At 900 °C, phase separation causes large a-Si patches to form, which is present in all Si-rich layer thicknesses. At 1000 °C c-Si NPs form, however no strong evidence is found for QC in these NPs. It is likely that ISR is dominant after annealing at 1000 °C, and the contribution of QC increases after subsequent passivation. At lower temperatures peak shifts corresponding to QC are present. The high energy contribution is independent of annealing temperature and subsequent passivation.

5.5 Photoluminescence Mechanisms

In this report, the PL spectra are deconvoluted with two gaussians, the low and high energy contribution. The low energy contribution is likely to be dominated by ISR. Peak shifts in accordance with QC indicate it is a combination of ISR and QC. The high energy contribution is ascribed to matrix defects, however its intensity was independent of any of the induced variables.

Although the results in this report are analysed with two contributions, it is possible that the spectrum is wrongly interpreted. The fact that the integrated intensity of the high energy contribution is independent of any of the induced variables, makes it highly unlikely that it is related to a matrix defect. A different combination of fitting functions, presented in chapter 2.3.6, could result in a completely different interpretation. In literature PL is deconvoluted with as much as three [11, 127] or even four [128] gaussian functions, however a check for overfitting is often lacking. From the analysis presented in this report, it is clear that PL is a useful tool and can identify certain properties, however it should not be used on its own because of the complex interpretation.

5.6 Recommendations

5.6.1 Si Nanoparticles Embedded in SiO_2

Because of the influence of the composition on clustering, the optimal composition of the Si-rich layer needs to be determined. This optimum depends on the annealing conditions, and annealing at 1000 °C has proven to yield c-Si NPs. It would be interesting to anneal at higher temperatures, in order to reach a higher crystallinity, but it is likely that the excess silicon in the buffer layer then starts to crystallize. For this, the composition of the buffer layer should also be changed to contain a lower excess silicon content. The thickness of the Si-rich layer has proven to influence the NP size distribution, and the proper thickness depends on the application.

TF passivation has shown the best results, and should be considered for future passivation. Both higher temperatures, and longer processing times can be investigated, in order to reach the most efficient passivation process.

5.6.2 Scaled Photoluminescence Measurements

The presented scaling method has proven to be useful for comparing PL spectra. However a number of measurement were omitted afterwards because of unexpected behaviour. These faulty measurements are likely to be due to bad scaling, which is ascribed to a wrong fit of the Raman phonon modes. By reducing the noise of the measurement, this effect might be reduced. Therefore the effect of laser intensity should be investigated further, as higher intensities can lead to higher signal-to-noise ratios.

In this report the temperature and excitation power were assumed to be constant, however it would be interesting to investigate these two effects. Higher excitation power will result in higher signal-to-noise ratios, but can also influence the PL spectrum because of higher generation rates and the state filling effect [55]. Temperature also influences the PL spectrum and intensity, and could provide interesting information about the PL mechanisms.

Another variable, present in the used Raman setup, is the lens. By using a different magnification factor, the spot diameter and focal depth can be changed. This could be used to determine PL of the sample on a smaller surface, resulting in more information about the sample homogeneity. The focal depth will influence the contribution of the substrate, and maybe a way of removing the effect of the substrate can be developed.

To ease interpretation of PL spectra, a couple of interesting measurements can be performed. Transmission electron microscopy could identify the NP spacing and size distribution. Electron spin resonance would be helpful to identify the defects present in the material. PL lifetime measurements could identify the number of contributions present, and give insight into the different mechanisms. Measuring the PL spectrum at different temperatures would also provide insight into the mechamisms.

Bibliography

[1] IPCC. Climate Change 2014 Synthesis Report Summary Chapter for Policymakers. *IPCC*, page 31, 2014.

[2] Photovoltaics report. Technical Report November, Faunhofer ISE, Freiburg, 2015.

[3] A. Richter, M. Hermle, and S. W. Glunz. Reassessment of the limiting efficiency for crystalline silicon solar cells. *IEEE Journal of Photovoltaics*, 3(4):1184–1191, 2013.

[4] X. Chen and P. Yang. Preparation and photovoltaic properties of silicon quantum dots embedded in a dielectric matrix: a review. *Journal of Materials Science: Materials in Electronics*, 26(7):4604–4617, 2015.

[5] M. Schnabel, C. Weiss, P. Löper, P. R. Wilshaw, and S. Janz. Self-assembled silicon nanocrystal arrays for photovoltaics. *Physica Status Solidi (a)*, 1661(8):1649–1661, 2015.

[6] G. Conibeer, M. Green, R. Corkish, Y. Cho, E. C. Cho, C. W. Jiang, T. Fangsuwannarak, E. Pink, Y. Huang, T. Puzzer, T. Trupke, B. Richards, A. Shalav, and K. L. Lin. Silicon nanostructures for third generation photovoltaic solar cells. *Thin Solid Films*, 511-512:654–662, 2006.

[7] F. Iacona, G. Franzò, and C. Spinella. Correlation between luminescence and structural properties of Si nanocrystals. *Journal of Applied Physics*, 87(3):1295–1303, 2000.

[8] N. Daldosso, G. Das, S. Larcheri, G. Mariotto, G. Dalba, L. Pavesi, a. Irrera, F. Priolo, F. Iacona, and F. Rocca. Silicon nanocrystal formation in annealed silicon-rich silicon oxide films prepared by plasma enhanced chemical vapor deposition. *Journal of Applied Physics*, 101(11):0–7, 2007.

[9] X. Y. Chen, Y. F. Lu, L. J. Tang, Y. H. Wu, B. J. Cho, X. J. Xu, J. R. Dong, and W. D. Song. Annealing and oxidation of silicon oxide films prepared by plasma-enhanced chemical vapor deposition. *Journal of Applied Physics*, 97(1):014913–1 – 014913–10, 2005.

[10] K. S. Min, K. V. Shcheglov, C. M. Yang, H. A. Atwater, M. L. Brongersma, and A. Polman. Defect-related versus excitonic visible light emission from ion beam synthesized Si nanocrystals in SiO_2. *Applied Physics Letters*, 69(14):2033–2035, 1996.

[11] X. X. Wang, J. G. Zhang, L. Ding, B. W. Cheng, W. K. Ge, J. Z. Yu, and Q. M. Wang. Origin and evolution of photoluminescence from Si nanocrystals embedded in a SiO_2 matrix. *Physical Review B - Condensed Matter and Materials Physics*, 72(19): 195313, 2005.

[12] D. Nesheva, C. Raptis, A. Perakis, I. Bineva, Z. Aneva, Z. Levi, S. Alexandrova, and H. Hofmeister. Raman scattering and photoluminescence from Si nanoparticles in annealed SiO_x thin films. *Journal of Applied Physics*, 92(8):4678, 2002.

[13] S. Godefroo, M. Hayne, M. Jivanescu, A. Stesmans, M. Zacharias, O. I. Lebedev, G. Van Tendeloo, and V. V. Moshchalkov. Classification and control of the origin of photoluminescence from Si nanocrystals. *Nature nanotechnology*, 3(3):174–178, 2008.

[14] D. Lockwood, Z. Lu, and J.-M. Baribeau. Quantum Confined Luminescence in Si/SiO_2 Superlattices. *Physical Review Letters*, 76(3):539–541, 1996.

[15] G. Conibeer, M. Green, E. C. Cho, D. König, Y. H. Cho, T. Fangsuwannarak, G. Scardera, E. Pink, Y. Huang, T. Puzzer, S. Huang, D. Song, C. Flynn, S. Park, X. Hao, and D. Mansfield. Silicon quantum dot nanostructures for tandem photovoltaic cells. *Thin Solid Films*, 516(20):6748–6756, 2008.

[16] A. H. M. Smets, K. Jäger, O. Isabella, R. A. C. M. M. van Swaaij, and M. Zeman. *Solar energy*. UIT Cambridge, 2016. ISBN 9781854184153.

[17] L. Pavesi and R. Turan. *Silicon Nanocrystals - Fundamentals, Synthesis and Applications*. Wiley-VCH, 2010.

[18] V. Kapaklis. Structural characterization of silicon nanocrystals from amorphous silicon oxide materials. *Journal of Non-Crystalline Solids*, 354(2-9):612–617, 2008.

[19] N. Baran, B. Bulakh, Y. Venger, N. Korsunska, L. Khomenkova, T. Stara, Y. Goldstein, E. Savir, and J. Jedrzejewski. The structure of $Si\text{-}SiO_2$ layers with high excess Si content prepared by magnetron sputtering. *Thin Solid Films*, 517(18):5468–5473, 2009.

[20] S. Ossicini, E. Degoli, M. Luppi, and R. Magri. Si nanostructures embedded in SiO_2: Electronic and optical properties. *Optical Properties of Nanocrystals*, 4808:73–84, 2002.

[21] F. Delachat, M. Carrada, G. Ferblantier, A. Slaoui, C. Bonafos, S. Schamm, and H. Rinnert. Structural and optical properties of Si nanocrystals embedded in SiO_2/SiN_x multilayers. *Physica E*, 41(6):994–997, 2009.

[22] E. Degoli and S. Ossicini. Role of defects in Si/SiO_2 quantum wells. *Optical Materials*, 17(1-2):95–98, 2001.

[23] L. Bi, Y. He, and J. Y. Feng. Effect of post-annealing in oxygen atmosphere on the photoluminescence properties of nc-Si rich SiO_2 films. *Journal of Crystal Growth*, 289 (2):564–567, 2006.

[24] Y. He, L. Bi, J. Feng, and Q. Wu. Properties of Si-rich SiO_2 films by RF magnetron sputtering. *Journal of Crystal Growth*, 280(3-4):352–356, 2005.

[25] H. Rinnert, O. Jambois, M. Vergnat, and M. Molinari. Study of the photoluminescence of amorphous and crystalline silicon clusters in SiO_x thin films. *Optical Materials*, 27 (5):983–987, 2005.

[26] H. Rinnert, M. Vergnat, G. Marchal, and A. Burneau. Strong visible photoluminescence in amorphous SiO and SiO:H. *Journal of Luminescence*, 80:445–448, 1999.

[27] O. Jambois, M. Molinari, H. Rinnert, and M. Vergnat. Photoluminescence and electroluminescence of amorphous SiO_x films prepared by reactive evaporation of silicon with oxygen. *Optical Materials*, 27(5):1074–1078, 2005.

[28] Z. Ma, L. Wang, K. Chen, W. Li, L. Zhang, Y. Bao, X. Wang, J. Xu, X. Huang, and D. Feng. Blue light emission in nc-Si/SiO_2 multilayers fabricated using layer by layer plasma oxidation. *Journal of Non-Crystalline Solids*, 302:648–652, 2002.

[29] T. Shimizu-Iwayama, K. Fujita, S. Nakao, K. Saitoh, T. Fujita, and N. Itoh. Visible photoluminescence in Si^+-implanted silica glass. *Journal of Applied Physics*, 75(12): 7779–7783, 1994.

[30] T. Shimizu-Iwayama, S. Nakao, and K. Saitoh. Visible photoluminescence in Si^+-implanted thermal oxide films on crystalline Si. *Applied Physics Letters*, 65(14):1814–1816, 1994.

[31] T. Shimizu-Iwayama, S. Nakao, K. Saitoh, and N. Itoh. Photoluminescence from nanoparticles of silicon embedded in an amorphous silicon dioxide matrix. *Journal of Physics: Condensed Matter*, 6(39):L601–L606, 1994.

[32] H. Z. Song and X. M. Bao. Visible photoluminescence from silicon-ion-implanted SiO_2 film and its multiple mechanisms. *Physical Review B*, 55(11):6988–6993, 1997.

[33] X. Wu, A. Bek, A. M. Bittner, C. Eggs, C. Ossadnik, and S. Veprek. The effect of annealing conditions on the red photoluminescence of nanocrystalline Si/SiO_2 films. *Thin Solid Films*, 425:175–184, 2003.

[34] J. Mei, Y. Rui, Z. Ma, J. Xu, D. Zhu, L. Yang, X. Li, W. Li, X. Huang, and K. Chen. Contribution of multiple emitting centers to luminescence from Si / SiO_2 multilayers with step by step thermal annealing. *Solid State Communications*, 131(11):701–705, 2004.

[35] S. M. Prokes and O. J. Glembocki. Role of interfacial oxide-related defects in the red-light emission in porous silicon. *Physical Review B*, 49(3):2238–2241, 1994.

[36] G. Pacchioni, L. Skuja, and D. L. Griscom. *Defects in SiO_2 and related dielectrics: Science and technology*. Springer Science and Business Media, 2000.

[37] B. Averboukh, R. Huber, K. W. Cheah, Y. R. Shen, G. G. Qin, Z. C. Ma, and W. H. Zong. Luminescence studies of a Si/SiO_2 superlattice. *Journal of Applied Physics*, 92 (7):3564, 2002.

[38] K. S. Seol, Y. Ohki, H. Nishikawa, M. Takiyama, and Y. Hama. Effect of implanted ion species on the decay kinetics of 2.7 eV photoluminescence in thermal SiO_2 films. *Journal of Applied Physics*, 80(11):6444, 1996.

[39] H. Nishikawa, E. Watanabe, and D. Ito. Decay Kinetics of the 4.4 eV Photoluminescence Associated with the Two States of Oxygen-Deficient-Type Defect in Amorphous SiO_2. *Physical Review Letters*, 72(13):2101–2104, 1994.

[40] T.-H. Tsai, M.-Y. Lin, L.-J. Hsiao, W.-K. Choi, and H. Y. Lin. Narrow-band amplified photoluminescence of amorphous silicon quantum dots via the coupling between localized surface plasmon and Fabry-Pérot cavity modes. *Optical Engineering*, 55(2): 027104, 2016.

[41] Y. Kanemitsu, T. Ogawa, K. Shiraishi, and K. Takeda. Visible photoluminescence from oxidized Si nanometer-sized spheres: Exciton confinement on a spherical shell. *Physical Review B*, 48(7):4883–4886, 1993.

[42] M. Burchielli, G. Conte, G. Fameli, C. Felici, M. C. Rossi, A. Rubino, S. Salvatori, and F. Villani. Functional properties of silicon nanocrystals in oxygen-rich amorphous matrices formed by laser irradiation of substoichiometric silicon oxides. *Materials Science and Engineering C*, 19(1-2):175–179, 2002.

[43] V. A. Belyakov, V. A. Burdov, R. Lockwood, and A. Meldrum. Silicon nanocrystals: Fundamental theory and implications for stimulated emission. *Advances in Optical Technologies*, 2008, 2008.

[44] B. J. Hinds, F. Wang, D. M. Wolfe, C. L. Hinkle, and G. Lucovsky. Study of SiO_x decomposition kinetics and formation of Si nanocrystals in an SiO_2 matrix. *Journal of Non-Crystalline Solids*, 227-230:507–512, 1998.

[45] M. A. Green, E. C. Cho, Y. Cho, Y. Huang, E. Pink, T. Trupke, and A. Lin. All-silicon tamdem cells based on artificial semiconductor sythesised using silicon quantum dots in a dielectric matrix. In *20th European Photovoltaic Solar Energy Conference*, pages 1689–1699, Barcelona, 2005. ISBN 9788578110796.

[46] M. Zacharias, J. Heitmann, R. Scholz, U. Kahler, M. Schmidt, and J. Bläsing. Size-controlled highly luminescent silicon nanocrystals: A SiO/SiO_2 superlattice approach. *Applied Physics Letters*, 80(4):661–663, 2002.

[47] N. X. Chung, R. Limpens, and T. Gregorkiewicz. Investigating photoluminescence quantum yield of silicon nanocrystals formed in SiO_x with different initial Si excess. 9562:95620O, 2015.

[48] L. Pavesi, L. D. Negro, C. Mazzoleni, G. Franzo, and F. Priolo. Optical gain in silicon nanocrystals. *Nature*, 408:440–444, 2000.

[49] P. M. Fauchet, L. Tsybeskov, S. P. Duttagupta, and K. D. Hirschman. Stable photoluminescence and electroluminescence from porous silicon. *Thin Solid Films*, 297(70): 254–260, 1997.

[50] G. Ledoux, O. Guillois, D. Porterat, C. Reynaud, F. Huisken, B. Kohn, and V. Paillard. Photoluminescence properties of silicon nanocrystals as a function of their size. *Physical Review B*, 62(23):15942–15951, 2000.

[51] T. Creazzo, B. Redding, E. Marchena, J. Murakowski, and D. W. Prather. Tunable photoluminescence and electroluminescence of size-controlled silicon nanocrystals in nanocrystalline-Si/SiO_2 superlattices. *Journal of Luminescence*, 130(4):631–636, 2010.

[52] H. Rinnert and M. Vergnat. Influence of the temperature on the photoluminescence of silicon clusters embedded in a silicon oxide matrix. *Physica E: Low-Dimensional Systems and Nanostructures*, 16(3-4):382–387, 2003.

[53] R. Limpens, S. L. Luxembo, A. W. Weeber, and T. Gregorkiewicz. Emission efficiency limit of Si nanocrystals. *Scientific Reports*, pages 1–6, 2016.

[54] A. Hryciw, A. Meldrum, K. S. Buchanan, and C. W. White. Effects of particle size and excitation spectrum on the photoluminescence of silicon nanocrystals formed by ion implantation. *Nuclear Instruments and Methods in Physics Research, Section B: Beam Interactions with Materials and Atoms*, 222(3-4):469–476, 2004.

[55] L. V. Dao, X. Wen, M. T. T. Do, P. Hannaford, E. C. Cho, Y. H. Cho, and Y. Huang. Time-resolved and time-integrated photoluminescence analysis of state filling and quantum confinement of silicon quantum dots. *Journal of Applied Physics*, 97(1), 2005.

[56] J. Wang, M. Righini, A. Gnoli, S. Foss, T. Finstad, U. Serincan, and R. Turan. Thermal activation energy of crystal and amorphous nano-silicon in SiO_2 matrix. *Solid State Communications*, 147(11-12):461–464, 2008.

[57] D. J. Griffiths. *Introduction to Quantum Mechanics*. Pearson Education International, 2nd edition, 2005. ISBN 0-13-124405-1.

[58] H. D. Barber. Effective mass and intrinsic concentration in silicon. *Solid-State Electronics*, 10(11):1039–1051, 1967.

[59] ETH Zürich Quantum Device Lab - lecture notes, 2006.

[60] G. Tuttle. Tunneling - lecture notes, 2013.

[61] P. Harrison. *Quantum Wells, Wires and Dots*. Wiley, Leeds, UK, 2 edition, 2005. ISBN 9780470010792.

[62] L. X. Yi, J. Heitmann, R. Scholz, and M. Zacharias. Si rings, Si clusters, and Si nanocrystals - Different states of ultrathin SiO_x layers. *Applied Physics Letters*, 81 (22):4248–4250, 2002.

[63] F. Yun, B. J. Hinds, S. Hatatani, S. Oda, Q. X. Zhao, and M. Willander. Study of structural and optical properties of nanocrystalline silicon embedded in SiO_2. *Thin Solid Films*, pages 137–141, 2000.

[64] M. Zacharias and P. Streitenberger. Crystallization of amorphous superlattices in the limit of ultrathin films with oxide interfaces. *Physical Review B - Condensed Matter and Materials Physics*, 62(12):8391–8396, 2000.

[65] C. Spinella, S. Lombardo, and F. Priolo. Crystall grain nucleation in amorphous silicon. *J. Appl. Phys.*, 84(10):5383–5414, 1998.

[66] D. Song, E.-C. Cho, G. Conibeer, C. Flynn, Y. Huang, and M. A. Green. Structural, electrical and photovoltaic characterization of Si nanocrystals embedded SiC matrix and Si nanocrystals/*c*-Si heterojunction devices. *Solar Energy Materials and Solar Cells*, 92(4):474–481, 2008.

[67] S. Janz, P. Löper, and M. Schnabel. Silicon nanocrystals produced by solid phase crystallisation of superlattices for photovoltaic applications. *Materials Science and Engineering B: Solid-State Materials for Advanced Technology*, 178(9):542–550, 2013.

[68] E.-C. Cho, S. Park, X. Hao, D. Song, G. Conibeer, S. C. Park, and M. A. Green. Silicon quantum dot/crystalline silicon solar cells. *Nanotechnology*, 19(24):245201, 2008.

[69] D. Hiller, S. Goetze, and M. Zacharias. Rapid thermal annealing of size-controlled Si nanocrystals: Dependence of interface defect density on thermal budget. *Journal of Applied Physics*, 109(5):0–5, 2011.

[70] K. Ding, U. Aeberhard, O. Astakhov, U. Breuer, M. Beigmohamadi, S. Suckow, B. Berghoff, W. Beyer, F. Finger, R. Carius, and U. Rau. Defect passivation by hydrogen reincorporation for silicon quantum dots in SiC/SiO_x hetero-superlattice. *Journal of Non-Crystalline Solids*, 358(17):2145–2149, 2012.

[71] Y. Q. Cao, X. Xu, S. X. Li, W. Li, J. Xu, and K. Chen. Improved photovoltaic properties of Si quantum dots/SiC multilayers-based heterojunction solar cells by reducing tunneling barrier thickness. *Frontiers of Optoelectronics*, 6(2):228–233, 2013.

[72] N. R. Mavilla, C. S. Solanki, and J. Vasi. Raman spectroscopy of silicon-nanocrystals fabricated by inductively coupled plasma chemical vapor deposition. *Physica E: Low-Dimensional Systems and Nanostructures*, 52:59–64, 2013.

[73] Y. Cao, P. Lu, X. Zhang, J. Xu, L. Xu, and K. Chen. Enhanced photovoltaic property by forming p-i-n structures containing Si quantum dots / SiC multilayers. *Nanoscale research letters*, 9(634):2–7, 2014.

[74] D. Hiller, S. Gutsch, A. M. Hartel, P. Löper, T. Gebel, and M. Zacharias. A low thermal impact annealing process for SiO_2-embedded Si nanocrystals with optimized interface quality. *Journal of Applied Physics*, 115(13):134311, 2014.

[75] M. L. Ciurea and A. M. Lepadatu. Tuning the properties of Ge and Si nanocrystals based structures by tailoring the preparation conditions Review. *Digest Journal of Nanomaterials and Biostructures*, 10(1):59–87, 2015.

[76] W. Liao, X. Zeng, X. Wen, X. Chen, and W. Wang. Annealing and excitation dependent photoluminescence of silicon rich silicon nitride films with silicon quantum dots. *Vaccum*, 121:147–151, 2015.

[77] G. Franzò, A. Irrera, E. C. Moreira, M. Miritello, F. Iacona, D. Sanfilippo, G. Di Stefano, P. G. Fallica, and F. Priolo. Electroluminescence of silicon nanocrystals in MOS structures. *Applied Physics A*, 74:1–5, 2002.

[78] F. Iacona, G. Franzò, E. C. Moreira, and F. Priolo. Silicon nanocrystals and $Er_3{}^+$ ions in an optical microcavity. *Journal of Applied Physics*, 89(12):8354–8356, 2001.

[79] G. Viera, S. Huet, and L. Boufendi. Crystal size and temperature measurements in nanostructured silicon using Raman spectroscopy. *Journal of Applied Physics*, 90(8): 4175–4183, 2001.

[80] C. Smit, R. A. C. M. M. Van Swaaij, H. Donker, A. M. H. N. Petit, W. M. M. Kessels, and M. C. M. Van de Sanden. Determining the material structure of microcrystalline silicon from Raman spectra. *Journal of Applied Physics*, 94(5):3582–3588, 2003.

[81] A. T. Voutsas, M. K. Hatalis, J. Boyce, and A. Chiang. Raman spectroscopy of amorphous and microcrystalline silicon films deposited by low-pressure chemical vapor deposition. *Journal of Applied Physics*, 78(12):6999–7006, 1995.

[82] M. van Sebille, R. A. Vasudevan, R. J. Lancee, R. A. C. M. M. van Swaaij, and M. Zeman. Optical characterization and density of states determination of silicon nanocrystals embedded in amorphous silicon based matrix. *Journal of Physics D: Applied Physics*, 325302(48):1–17, 2015.

[83] K. Küsová, L. Ondič, E. Klimešová, K. Herynková, I. Pelant, S. Daniš, J. Valenta, M. Gallart, M. Ziegler, B. Hönerlage, and P. Gilliot. Luminescence of free-standing versus matrix-embedded oxide-passivated silicon nanocrystals : The role of matrix-induced strain. *Applied Physics Letters*, 101:143101, 2012.

[84] N. Daldosso, M. Luppi, S. Ossicini, E. Degoli, R. Magri, G. Dalba, P. Fornasini, R. Grisenti, F. Rocca, L. Pavesi, S. Boninelli, F. Priolo, C. Spinella, and F. Iacona. Role of the interface region on the optoelectronic properties of silicon nanocrystals embedded in SiO_2. *Physical Review B*, 68(8):1–8, 2003.

[85] F. Himpsel, F. McFeely, A. Taleb-Ibrahimi, J. Yarmoff, and G. Hollinger. Microscopic structure of the SiO_2/Si interface. *Physical Review B*, 38(9):6084–6096, 1988.

[86] S. Munekuni, T. Yamanaka, Y. Shimogaichi, R. Tohmon, Y. Ohki, K. Nagasawa, and Y. Hama. Various types of nonbridging oxygen hole center in high-purity silica glass. *Journal of Applied Physics*, 68(3):1212–1217, 1990.

[87] R. Salh. Defect related luminescence in silicon dioxide network: a review. In *Crystalline Silicon - Properties and Uses*, chapter 8 - Defect, pages 135–172. 2011. ISBN 978-953-307-587-7.

[88] K. Nagasawa, Y. Ohki, and Y. Hama. Gamma-Ray Induced 2 eV Optical Absorption Band in Pure-Silica Core Fibers. *Japanese Journal of Applied Physics*, 26(6):1009–1011, 1987.

[89] W. Füssel, M. Schmidt, H. Angermann, G. Mende, and H. Flietner. Defects at the Si/SiO_2 interface: Their nature and behaviour in technological processes and stress. *Nuclear Instruments and Methods in Physics Research, Section A: Accelerators, Spectrometers, Detectors and Associated Equipment*, 377(2-3):177–183, 1996.

[90] E. Cartier, J. H. Stathis, and D. A. Buchanan. Passivation and depassivation of silicon dangling bonds at the Si/SiO_2 interface by atomic hydrogen. *Applied Physics Letters*, 63(11):1510–1512, 1993.

[91] J. I. Pankove, M. A. Lampert, and M. L. Tarng. Hydrogenation and dehydrogenation of amorphous and crystalline silicon. *Applied Physics Letters*, 32(7):439–441, 1978.

[92] P. J. Caplan, E. H. Poindexter, B. E. Deal, and R. R. Razouk. ESR centers, interface states, and oxide fixed charge in thermally oxidized silicon wafers. *Journal of Applied Physics*, 50(1979):5847–5854, 1979.

[93] W. Paul, A. Lewis, G. Connell, and T. Moustakas. Doping, Schottky barrier and p-n junction formation in amorphous germanium and silicon by RF sputtering. *Solid State Community*, 20(10):969–972, 1976.

[94] A. G. Revesz. The Role of Hydrogen in SiO_2 Films on Silicon. *Journal of The Electrochemical Society*, 126(1):122, 1979.

[95] K. L. Brower. Kinetics of H_2 passivation of Pb centers at the (111)Si/SiO_2 interface. *Physical Review B*, 38(14):9657–9666, 1988.

[96] K. L. Brower and S. M. Myers. Chemical kinetics of hydrogen and (111)Si-SiO_2 interface defects. *Applied Physics Letters*, 57(2):162–164, 1990.

[97] A. Stesmans and G. van Gorp. Maximum Density of Pb Centers at the (111)Si/SiO_2 Interface After Vacuum Anneal. *Applied Physics Letters*, 57(25):2662–2665, 1990.

[98] A. Wójcik, T. J. Ochalski, J. Muszalski, E. Kowalczyk, K. Goszczyński, and M. Bugajski. Photoluminescence mapping and angle-resolved photoluminescence of MBE-grown InGaAs/GaAs RC LED and VCSEL structures. *Thin Solid Films*, 412(1-2): 114–121, 2002.

[99] R. Houdré, C. Weisbuch, R. P. Stanley, U. Oesterle, P. Pellandini, and M. Ilegems. Measurement of cavity-polariton dispersion curve from angle-resolved photoluminescence experiments. *Physical Review Letters*, 73(15):2043–2046, 1994.

[100] K. S. Daskalakis, S. A. Maier, R. Murray, and S. Kéna-Cohen. Nonlinear interactions in an organic polariton condensate. *Nature materials*, 13(3):271–8, 2014.

[101] Heraeus Holding GmbH. Spectrosil® 2000 datasheet, 2016.

[102] K. Chen, Z. Ma, X. Huang, J. Xu, W. Li, Y. Sui, J. Mei, and D. Zhu. Comparison between light emission from Si/SiN_x and Si/SiO_2 multilayers: role of interface states. *Journal of Non-Crystalline Solids*, 338-340:448–451, 2004.

[103] A. Fusi. *Optical analysis of c-Si quantum dots embedded in a silica matrix.* Msc thesis, Technical University Delft, 2015.

[104] Solaris 100 Rapid Thermal Processor, 2010.

[105] H. Fujiwara. *Spectroscopic Ellipsometry: Principles and Applications.* Wiley, 2007. ISBN 9780470060186.

[106] A. Gencer Imer, S. Yerci, A. S. Alagoz, M. Kulakci, U. Serincan, T. G. Finstad, and R. Turan. Evolution of vibrational modes of SiO_2 during the formation of Ge and Si nanocrystals by ion implantation and magnetron sputtering. *Journal of nanoscience and nanotechnology*, 10(1):525–531, 2010.

[107] C. T. Kirk. Quantitative analysis of the effect of disorder-induced mode coupling on infrared absorption in silica. *Physical Review B*, 38(2):1255–1273, 1988.

[108] D. Nesheva, I. Bineva, Z. Levi, Z. Aneva, T. Merdzhanova, and J. C. Pivin. Composition, structure and annealing-induced phase separation in SiO_x films produced by thermal evaporation of SiO in vacuum. *Vacuum*, 68:1–9, 2003.

[109] D. V. Tsu, G. Lucovsky, and B. N. Davidson. Effects of the nearest neighbors and the alloy matrix on SiH stretching vibrations in the amorphous SiO_r:H ($0 < r < 2$) alloy system. *Physical Review B*, 40(3):1795–1805, 1989.

[110] M. Nakamura, Y. Mochizuki, K. Usami, Y. Itoh, and T. Nozaki. Infrared absorption spectra and compositions of evaporated silicon oxides (SiO_x). *Solid State Communications*, 50(12):1079–1081, 1984.

[111] L. Schumann, A. Lehmann, H. Sobotta, V. Riede, U. Teschner, and K. Hübner. Infrared Studies of Reactively Sputtered SiO_x Films in the Composition Range $0.2 \leq x \leq 1.9$. *Physica Status Solidi (b)*, 69, 1982.

[112] A. Lehmann, L. Schumann, and K. Hübner. Optical Phonons in Amorphous Silicon Oxides. *Physica Status Solidi (b)*, 689(11):689–698, 1984.

[113] A. L. Shabalov and M. S. Feldman. Optical properties and structure of thin SiO_x films. *Thin Solid Films*, 151(3):317–323, 1987.

[114] D. W. Berreman. Infrared absorption at longitudinal optic frequency in cubic crystal films. *Physical Review*, 130(6):2193–2198, 1963.

[115] M. V. de Grunt. *Raman spectroscopy of silicon quantum dots embedded in a silicon carbide matrix*. Msc thesis, Technical University Delft, Delft, 2013.

[116] Z. Remes, R. Vasudevan, K. Jarolimek, A. H. M. Smets, and M. Zeman. The Optical Spectra of a-Si:H and a-SiC:H Thin Films Measured by the Absolute Photothermal Deflection Spectroscopy (PDS). *Solid State Phenomena*, 213:19–28, 2014.

[117] I. Sychugov, R. Juhasz, J. Valenta, and J. Linnros. Narrow luminescence linewidth of a silicon quantum dot. *Physical Review Letters*, 94(8):4–7, 2005.

[118] M. Künle, T. Kaltenbach, P. Löper, A. Hartel, S. Janz, O. Eibl, and K. G. Nickel. Si-rich a-SiC:H thin films: Structural and optical transformations during thermal annealing. *Thin Solid Films*, 519(1):151–157, 2010.

[119] I. F. Crowe, M. P. Halsall, O. Hulko, A. P. Knights, R. M. Gwilliam, M. Wojdak, and A. J. Kenyon. Probing the phonon confinement in ultrasmall silicon nanocrystals reveals a size-dependent surface energy. *Journal of Applied Physics*, 109(8):0–8, 2011.

[120] H. Rinnert and M. Vergnat. Structure and optical properties of amorphous silicon oxide thin films with different porosities. *Journal of Non-Crystalline Solids*, 320(1-3): 64–75, 2003.

[121] H. Rinnert, M. Vergnat, and G. Marchal. Structure and optical properties of amorphous SiO_x thin films prepared by co-evaporation of Si and SiO. *Material science and engineering B*, 69-70:484–488, 2000.

[122] R. Limpens and T. Gregorkiewicz. Spectroscopic investigations of dark Si nanocrystals in SiO_2 and their role in external quantum efficiency quenching. *Journal of Applied Physics*, 114(7), 2013.

[123] M. van Sebille, J. Allebrandi, J. Quik, R. A. C. M. M. van Swaaij, and M. Zeman. Optimizing silicon oxide embedded silicon nanocrystal inter-particle distances. *Submitted for review to Nanoscale Research Letters*, 2016.

[124] F. Tournus. Random nanoparticle deposition: Inter-particle distances in 2D, 3D, and multilayer samples. *Journal of Nanoparticle Research*, 13(10):5211–5223, 2011.

[125] J. C. Slater. Atomic Radii in Crystals. *The Journal of Chemical Physics*, 41(10):3199, 1964.

[126] R. A. Street. The recombination of excess carriers. In *Hydrogenated Amorphous Silicon*, chapter 8, pages 276–320. 1991. ISBN 9780511525247.

[127] J. Gan, Q. Li, Z. Hu, W. Yu, K. Gao, J. Sun, N. Xu, and J. Wu. Study on phase separation in a-SiO_x for Si nanocrystal formation through the correlation of photoluminescence with structural and optical properties. *Applied Surface Science*, 257(14): 6145–6151, 2011.

[128] E. Tuğay and R. Turan. Investigation of Photoluminescence Mechanisms from SiO_2/Si:SiO_2/SiO_2 Structures in Weak Quantum Confined Regime by Deconvolution of Photoluminescence Spectra. *Journal of Nanoscience and Nanotechnology*, 16(4): 4052–4064, 2016.

[129] G. Talukder, J. C. L. Cornish, P. Jennings, G. T. Hefter, B. W. Clare, and J. Livingstone. Effects of annealing on infrared and thermal-effusion spectra of sputtered a-Si:H alloys. *Journal of Applied Physics*, 71(1):403, 1992.

[130] L. Skuja, B. Güttler, D. Schiel, and a. R. Silin. Quantitative analysis of the concentration of interstitial O_2 molecules in SiO_2 glass using luminescence and Raman spectrometry. *Journal of Applied Physics*, 83(11):6106, 1998.

[131] Y. C. Fang, Z. J. Zhang, and M. Lu. Room temperature photoluminescence mechanism of SiO_x film after annealing at different temperatures. *Journal of Luminescence*, 126 (1):145–148, 2007.

[132] Z. qiang Xie, J. Zhu, M. Zhang, Y. yuan Zhao, and M. Lu. A combined approach to fabricating Si nanocrystals with high photoluminescence intensity. *Applied Surface Science*, 255(6):3833–3836, 2009.

[133] G. Pacchioni, G. Ieranò, and A. Márquez. Optical Absorption and Nonradiative Decay Mechanism of E' Center in Silica. *Physical Review Letters*, 81(2):377–380, 1998.

[134] K. Kajihara, Y. Ikuta, M. Hirano, and H. Hosono. Effect of F_2 laser power on defect formation in high-purity SiO_2 glass. *Journal of Non-Crystalline Solids*, 322(1-3):73–77, 2003.

[135] T. Cottrell. *The Strengths of Chemical Bonds*. Butterworths Scientific Publications, London, 2 edition, 1958.

[136] I. Bineva, D. Nesheva, Z. Aneva, and Z. Levi. Room temperature photoluminescence from amorphous silicon nanoparticles in SiO_x thin films. *Journal of Luminescence*, 126(2):497–502, 2007.

[137] E. C. Cho, M. A. Green, G. Conibeer, D. Song, Y. H. Cho, G. Scardera, S. Huang, S. Park, X. J. Hao, Y. Huang, and L. Van Dao. Silicon quantum dots in a dielectric matrix for all-silicon tandem solar cells. *Advances in OptoElectronics*, 2007:1–11, 2007.

[138] K. Zellama. Crystallization in amorphous silicon. *Journal of Applied Physics*, 50(11): 6995, 1979.

Photoluminescence Model

A

First the variation in layer thickness, due to the limited precision of the PECVD setup, is analysed. This is achieved by measuring the thickness of several layers in a transmission electron microscopy image. Next the literature study is summarized in table A.1.

A.1 Layer Thickness Variation

To determine the variation in layer thickness inside a multilayer sample, a multilayer sample with known layer thicknesses is analyzed with transmission electron microscopy. The resulting image is presented in figure A.1. The dark and light bands indicate the different layers. The imposed thickness of these layers is 4 nm. By measuring the thickness of these layers at 20 points, a mean thickness of 4 nm, and a standard deviation of 0.3 nm is obtained.

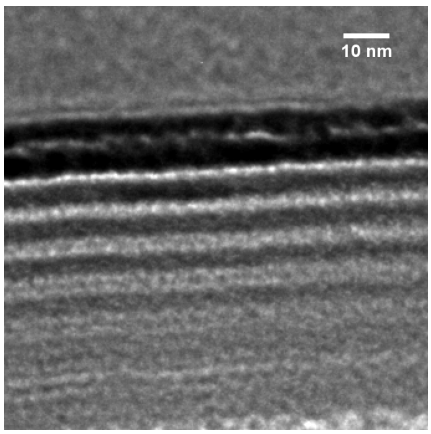

Figure A.1: A transmission electron microscopy image of a multilayer structure of Si-rich and buffer layers with a thickness of 4 nm. The different layers are indicated by the lighter and darker regions. This image was obtained by experiments caried out by Martijn van Sebille at the TU Delft.

A.2 Photoluminescence Maxima

The result of the literature study on PL mechanisms in silicon oxide embedded Si NP structures is presented in table A.1.

Table A.1: Reported photoluminescence maxima at room temperature, and their ascribed contributions in Si NPs embedded in silicon oxide. If only one value is given for the energy range there was only one maximum reported. If some entries are left blank, it was not specified. FWHM stands for full with at half maximum, and is an indication of the width of the contribution.

Contribution	Energy range [eV]		FWHM [eV]	Association	References
c-Si NPs	1.3	1.7		QC	[6]
	1.31	1.91		QC	[7]
		1.33		QC	[18]
	1.38	1.55		QC	[8]
	1.38	1.6		QC	[19]
	1.38	2.07		QC	[9]
	1.4	1.9		QC	[20]
	1.48	1.91		QC	[10]
		1.49		QC	[21]
	1.5	1.9		QC	[22]
	1.55	1.66		QC	[11]
	1.57	1.60		QC	[23]
	1.6	1.8		QC	[12]
		1.61		QC	[13]
	1.66	1.77		QC	[24]
	1.68	2.23		QC	[25]
	2.48	2.61		QC	[28]
a-Si NPs	1.52	1.67		QC	[18]
	1.7	2.3		QC	[14]
	1.7	1.94		QC	[26]
	1.91	1.99		QC	[25, 27]
Interface states	1.3	1.46		ISR	[11]
		1.55		ISR	[28, 48]
		1.65		ISR	[22]
		1.7		ISR	[20, 21, 29–32]
Defects	1.5	1.75		Oxygen thermal donor	[33]
		1.66	0.4	interfacial Si=O	[34]
	1.85	2.07	0.35	NBOHC	[35]
		1.91	0.17	NBOHC	[36]
		1.91	0.04	NBOHC	[24]
		2.0		SiO_x	[29]
		2.06	0.6	Si/SiO_2 interface	[37]
		2.07	0.6	SiO_2	[10]
		2.64		Oxygen vacancy	[32]
		2.64			[27]
		2.7		Oxygen deficiency	[38]
	3.27	3.36			[9]
		4.4		Oxygen deficiency	[39]

Measurement Error Analysis

B

A detailed measurement error analysis is performed on the Raman spectroscope, since this technique forms the core of this report. It comprises of three parts; the effect of focus, sample homogeneity, and total measurement method. Next the measurement error of a photothermal deflection spectroscopy measurement is identified.

B.1 Raman Spectroscope

To identify the measurement error in a scaled PL spectrum, three experiments are performed. First a sample is measured at the same spot six times in order to identify the error induced by focusing of the laser beam. Next the sample is measured at 10 different positions, without being cleaned in between the measurements. And finally the sample is again measured 10 times, but in between each measurement the sample is taken out of the Raman spectroscope, and cleaned and positioned on the sample stage again. These three experiments allow to identify the measurement error due to focussing, the inhomogeneity of the sample, and the total measurement error of the entire measurement procedure. The relative standard deviation σ_{rel} of each experiment is calculated by dividing the standard deviation at each photon energy STD(E), by the mean at that photon energy MEAN(E):

$$\sigma_{\text{rel}}(E) = \frac{\text{STD}(E)}{\text{MEAN}(E)}. \tag{B.1.1}$$

Next a polynomial fit is applied to obtain an estimate of the measurement error for further calculations.

First the effect of focussing is investigated. For this experiment the sample is cleaned once with semiconductor grade ethanol and wiped clean with a cleanroom tissue before placing it on the sample stage. Next the Raman spectroscope is closed, and the sample is only moved up and down by moving the sample stage with servo motors, controlled by a computer. This will reduce the contamination to a minimum, and will also reduce air currents inside the Raman spectroscope, causing dust to settle. The relative standard deviation of this experiment is presented in figure B.1**(a)**.

Next the inhomogeneity of the sample can be estimated by measuring the sample at 10 positions. The sample is again cleaned once before placing it on the sample stage, and the Raman spectroscope is closed. The sample stage is now also moved sideways in order to measure at different locations. The relative standard deviation

of this experiment is shown in figure B.1(**b**). The effect of inhomogeneity of the sample can be estimated by substracting the relative standard deviation of the focus experiment from this experiment, resulting in the red line in figure B.1(**b**), which is roughly constant at 2%.

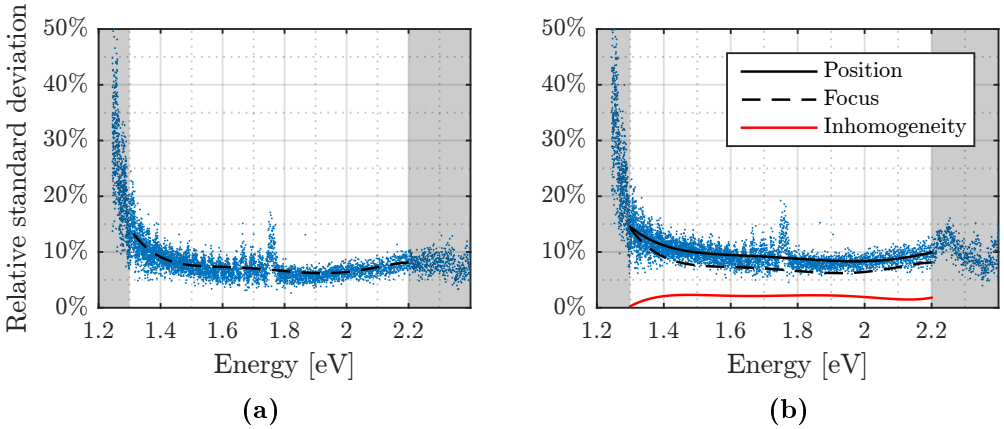

Figure B.1: The relative standard deviation of focussing **(a)** and position **(b)**. The legend in **(b)** holds for both figures. The shaded area represents data outside the boundaries used for fitting the PL spectrum.

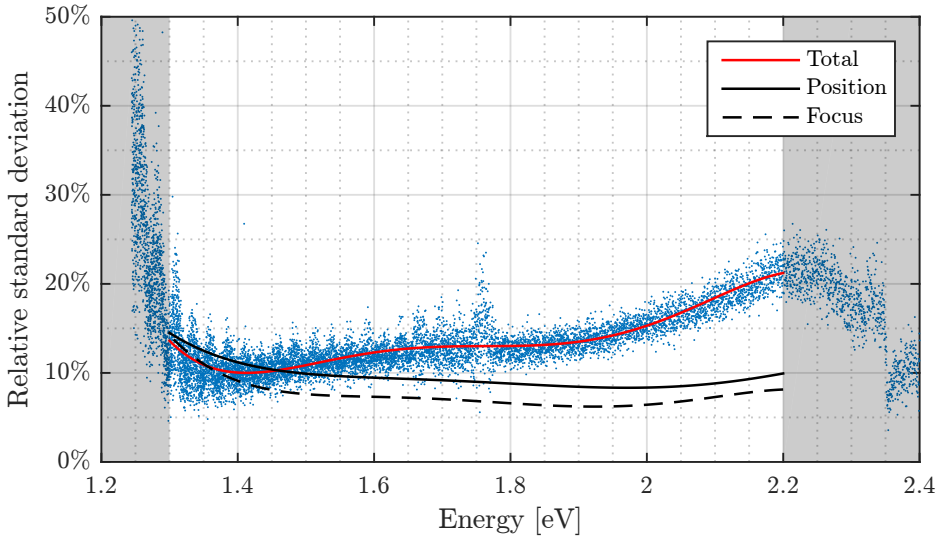

Figure B.2: The total relative standard deviation in a scaled PL spectrum. The shaded area represents data outside the boundaries used for fitting the PL spectrum.

Finally the total relative standard deviation is presented in figure B.2. In this

experiment, the sample is cleaned and positioned on the sample stage prior to each measurement, which is repeated 10 times. The relative standard deviation is expected to be the highest for this experiment, however this does not seem to be the case below 1.5 eV. This is probably due to a less than optimal fit of the polynomial in figure B.1(**b**). The noise levels in the obtained relative standard deviations also contribute to this fact.

B.1.1 Discussion

What first stands out is that the relative standard deviation increases drastically below 1.3 eV. Clearly the sensitivity of the detector deteriorates below 1.3 eV, which is the reason why this is chosen as the lower boundary for fitting the PL spectra. As a reminder; above 2.2 eV the Raman phonon modes are present, which is why that is the upper boundary for fitting.

The relative standard deviation of focussing, figure B.1a, is mostly constant. The increase below 1.4 eV is attributed to the sensitivity of the detector. Around 2.2 eV the PL intensity is low, decreasing the signal-to-noise ratio, and thus increasing standard deviation.

The inhomogeneity of the sample induces a constant deviation, indicated by the red line in figure B.1b. The decrease below 1.4 eV is again ascribed to a decrease in sensitivity of the detector.

The total relative standard deviation of this method shows a significant increase, especially above 2 eV. This is probably an agglomeration of several factors; cleaning liquid, cleaning method, handling of the sample, dust inside the Raman spectroscope and difference in sample angle. These are however inherent to this method and cannot be avoided. The red line in figure B.2 is the polynomial used for obtaining all standard deviations in scaled PL measurements presented in this report.

B.1.2 Incorporation of measurement error

To incorporate the obtained measurement error in the analysis of the PL spectra, each spectra is fitted three times. First the original spectrum is fitted. Next the standard deviation is respectively added and substracted from the PL spectra, after which the new spectra is fitted, yielding the upper and lower bounds of the standard deviation of the fit.

B.2 Photothermal Deflection Spectroscope

The PDS setup is a very sensitive setup which makes alignment very critical. The main causes for measurement errors during a PDS measurement are alignment errors and vibrations caused by the environment. Once a sample is placed into the setup, the setup needs to be aligned in order to function properly. This is a tricky procedure and has shown some unexpected behavior, further impeding alignment. Once

a measurement is running any vibration could cause unwanted errors in the measurement. This is already suppressed by the fact that the whole setup is positioned on an optical table, and the laser is even positioned on an additional optical table. However our experience is still that even the human voice can cause vibrations in this setup, showing how sensitive it really is. Fluctuations in the room temperature could also affect the measurement, since this influences the response of the detectors. The ambient light is also measured during the measurement in order to substract the background light, which also shows that it is best to keep the lighting constant during a measurement.

These factors are already kept to a minimum, however these external factors are sometimes inevitable and therefore an error analysis is necessary. A small experiment has been set up to measure this error. An annealed sample was measured five times over the course of several days. In between each measurement the sample was removed from the setup, and repositioned again. This experiment thus governs the alignment and external effects. Sample inhomogeneity will not be noticed as strong as during a Raman measurement, since the measurement spot of the PDS is roughly 5 mm in diameter, while the spot of the Raman spectroscope is focused to a spot with a diameter of 12 μm.

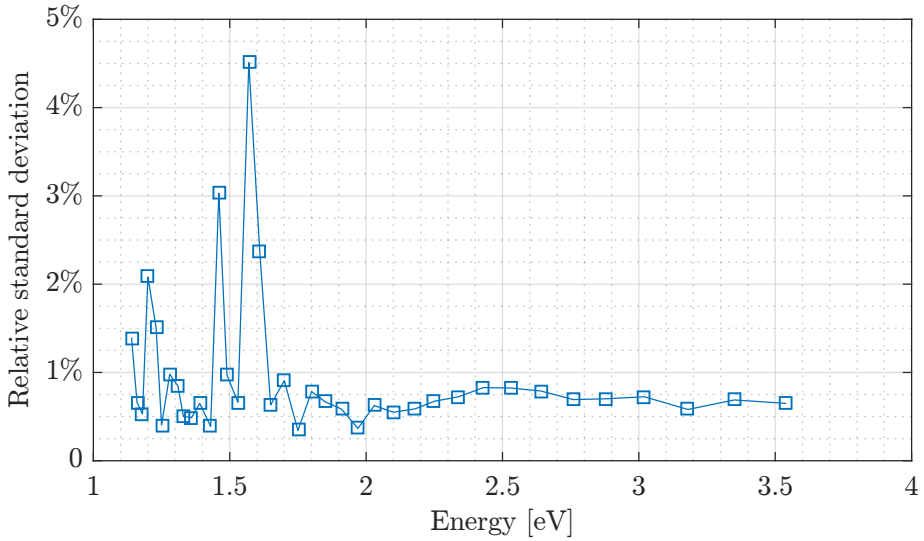

Figure B.3: The relative standard deviation in PDS measurements.

From figure B.3 it is clear that the measurement error is roughly 1%. Below 1.7 eV the signal becomes more noisy, however the relative error still remains below 5%. The increase in noise level is also expected since this region is at energies below the bandgap, which reduces the responsiveness of the setup.